UNIVERSITÀ DEGLI STUDI DI PADOVA

DIPARTIMENTO DI FISICA E ASTRONOMIA "GALILEO GALILEI"

CORSO DI DOTTORATO DI RICERCA IN ASTRONOMIA
Ciclo XXXVII

THE ASSEMBLY HISTORY OF THE MILKY WAY: INSIGHTS FROM METAL-POOR STARS AND SOLAR TWINS

Coordinator: Ch.mo Prof. Giovanni Carraro
Supervisor: Ch.mo Prof. Giovanni Carraro
Co-supervisor: Dr. Lorenzo Spina
Candidate: Anastasiia Plotnikova

Contents

Abstract

The Milky Way is a particular galaxy for the Sun. We are located in it. This fact gives us a great opportunity to study its formation and evolution in detail. And later we can generalize obtained knowledge to further galaxies in the Universe.

There are several different approaches to exploring the history of the Milky Way. One of them is studying it from its small members - stars. Stars provide us with information on their age, chemical composition and kinematics. And all of these data together can tell us the story of the Milky Way formation and evolution. With age, we can trace the timeline of the formation, its different stages, correlations and order of the events. Chemical composition shows us the composition of the environment in which the stars were formed and lived. Also, kinematics contains the dynamical history, how stars are moving in the Galaxy or even in the Universe, how and with what they interact and in tandem with chemistry it can provide the most probable location where the star was formed.

As we can see stars are great targets to use in the Milky Way formation and evolution study. By combining stars of different types we can study different parts of the Galaxy which they are populating at various periods in time.

In this work, I start with exploring the oldest objects in the Galaxy - very metal-poor stars. Due to their low metallicity, they represent the initial phases of the Milky Way formation.

In Chapter 2 I derive precise ages with the isochrone fitting technique for single stars. This method is the most popular one for the cluster's age determination. However, it can be successfully used also to derive the age for a single star in the turnoff/sub-giant branch region of the color-magnitude diagram. But to achieve high precision we have to carefully take into account all possible sources of uncertainties such as distance, reddening, metallicity, photometry, chemical composition and use different theoretical models (isochrones). An automatic algorithm was created for these purposes. As a result we get the mean age of the sample 13.9 ± 0.5 Gyr using Padova isochrones[1], and 13.7 ± 0.4 Gyr using BASTI[2] isochrones (Bag of Stellar Tracks and Isochrones). Additionally, we found a group of very metal-poor stars ($\left[\frac{Fe}{H}\right]$: -2.7 – -2.0 dex) with relatively young ages, in the range 8 – 10 Gyr.

In Chapter 3 I investigate the origin of very metal-poor stars. To do so I derive the kinematical properties of each star using McMillan (2017) potential and astrometric parameters from Gaia (Gaia Collaboration et al. (2022a), Gaia Collaboration et al. (2022b)). Combining kinematics and chemistry derived by Barklem et al. (2005) we can derive the origin of these stars. We found that some stars have clear signatures to be part of the Halo population. However, the 8 oldest could have formed in the primordial Bulge because of their orbital parameters (large eccentricity and low Z_{max} mostly) and large *alpha*-abundance. The other group of the stars can be associated with Gaia-Enceladus/Sausage (GE), and Thamnos 1, 2 according to their similarity in kinematics, chemistry and age.

Changing the target of the investigation to on average younger type of stars - solar twins, we can study more recent phases of the Milky Way formation. Particularly, stars with similar to the Sun's effective temperature, surface gravity and metallicity are mainly forming in the Thin disk of the Galaxy and tell us about its formation.

[1] http://stev.oapd.inaf.it/cmd

[2] http://basti-iac.oa-abruzzo.inaf.it/isocs.html

In Chapter 4 I perform a line-by-line differential spectroscopic analysis of our sample of solar twin stars with respect to the Sun and enlarge it with the dataset analyzed by Casali et al. (2020). Obtained high-precision effective temperature, surface gravity and metallicity allow us to derive precise ages with an average uncertainty of 0.7 Gyr.

Now, together with metallicity, we can study the age-metallicity relationship for the Thin disk. Age-metallicity relationship is one of the most important trends in the Galaxy. It shows how stars were forming and dying, how the environment was changing and what did it interact with. In this Chapter 4 we studied whether any bimodality in age-metallicity relation, such that found by Nissen et al. (2020), really exists or not. We did not detect any presence of separation into two populations for the Thin disk. Also, we demonstrate that for this kind of analysis, it is very important to take into account selection bias and statistical error together with all sources of uncertainties.

Additionally, in Chapter 4 we derive the birth radius to study the chemical evolution of the Thin disk. As a result, we propose that to reach today's chemical composition in the Thin disk the most probable scenario is that radial migration played an important role in the Thin disk formation together with the possible contribution of known accretion events such as Gaia-Enceladus/Sausage and Sagittarius.

In the end, two completely different groups of stars show us the history of the Milky Way's formation and evolution. Starting from the very beginning with very metal-poor stars we investigate that first to form was pristine Buldge. Then Halo and Disk were formed with the possible contribution from the accretion events. Then, from solar twins, we confirm that the Thin disk - one of the youngest components of the Milky Way - reached today's chemical composition due to radial migration also with the possible contribution of accretion events. More important we do not see the bimodal distribution in the age-metallicity relation that suggests that the Thin disk was formed relatively smoothly.

Symbols

α, δ	right ascension, declination	deg
l, b	galactic longitude, galactic latitude	deg
$\mathrm{M}_\odot$	solar mass	1.98892×10^{30} kg
$\mathrm{R}_\odot$	solar radius	6.957×10^{8} m
$T_{eff,\odot}$	solar effective temperature	5771 K
$logg_\odot$	solar surface gravity	4.44 dex
pc	parsec	$3.08567758149137 \times 10^{16}$ m
Gyr	gigayear	3.1536×10^{16} s
c	speed of light in vacuum	$2.99792458 \times 10^{8}\,\mathrm{m\,s^{-1}}$
G	gravitational constant	6.6743×10^{-11} $\mathrm{m^3\ kg^{-1}\ s^{-2}}$

Acronyms

ΛCDM	Λ cold dark matter
AMR	Age-metallicity relation
B/P	Boxy/peanut
CMB	Cosmic microwave background
CMD	Color-magnitude diagram
DEC	Declination
ELS	Eggen, Lynden-Bell and Sandage
EW	Equivalent width
GC	Globular cluster
GES/GE	Gaia-Enceladus/Sausage
HFS	Hyper-fine splitting
HTD	Hot thick disk
LTE	Local thermodynamical equilibrium
MS	Main sequence
MW	Milky Way
PI	Pair Instability
RA	Right ascension
RGB	Red Giant Branch
SE	Secular Evolution
SGB	Sub Giant Branch
Sgr	Sagittarius
SNe	Supernovae
S/N	Signal-to-noise
TO	Turnoff
VMP	Very metal-poor

Chapter 1

Stars and their stories

1.1 Stellar type

1.1.1 Very metal-poor stars

Stars with extremely low metal abundances ($[Fe/H] < -1.5$ dex) are of particular astrophysical and cosmological interest because they probe very early times in the evolution of the Universe and its Galactic components. Through the investigation of the age, kinematics and chemical composition we can obtain important constraints on the evolution of the Milky Way, set up a lower limit of the age of the Universe and understand the chemical and dynamical properties of the first Population III supernovae.

Very metal-poor stars are ideal probes of the beginning of the evolution of the Universe. Because of their low metallicity, they are linked to the most pristine star formation episodes in the Universe. Studies of these ancient stars have allowed stellar archaeologists to determine the chemical composition of the star-forming environments in the nascent Milky Way (Frebel &Norris (2015))

Over the years, investigations of metal-poor stars were limited by their faint apparent magnitude. As instrumentation improved, we started to have spectroscopically studied samples with a number of stars large enough for statistical study (Christlieb et al. (2004), Cayrel et al. (2004), Barklem et al. (2005), Schlaufman &Casey (2014), Limberg et al. (2021), etc.).

Metal-poor stars have not been studied as extensively as stars with close-to-solar metallicity, because in nowadays universe they are rare objects. Due to star formation, newborn stars are polluted with metals from the cloud which was enriched in heavy elements from the first supernovae. That is why stars that have low metallicity were born in regions where cosmic star formation just started at high redshift. From Madau &Dickinson (2014) we know that starting from the beginning of the Universe in the first 3-4 billion years star formation rapidly increased and then slowly but continuously decreased from then until to date. Consequently, metal-poor stars are very old and if they are still alive they are typically low mass stars hence they have faint apparent magnitudes, which causes difficulties for their detection. Also to confirm the low metallicity abundance of the star high-resolution spectroscopical analysis needed to be done which is more difficult to perform for a large sample of stars compared with photometry.

The acquisition of high signal-to-noise spectra for faint metal-poor stars requires a major telescope-time commitment, making the construction of large samples of metal-

poor star abundances prohibitively expensive. Schlaufman &Casey (2014) have developed a new, efficient selection that uses only public, all-sky APASS optical, 2MASS near-infrared, and WISE mid-infrared photometry to identify bright metal-poor star candidates through their lack of molecular absorption near 4.6 microns. The result of the selection is a sample of 11 916 metal-poor star candidates with V < 14, that increases the number of publicly available candidates by more than five times in this magnitude range. The bright apparent magnitudes of this sample have eventually allowed high-resolution follow-up observations that have detected seven previously unknown stars with $\left[\frac{Fe}{H}\right] < -3.0$. The follow-up campaign has identified that $3.8^{+1.3}_{-1.1}\%$ of Schlaufman &Casey (2014) candidates have $\left[\frac{Fe}{H}\right] < -3.0$ and $32.5^{+3.0}_{-2.9}\%$ have $-3.0 < \left[\frac{Fe}{H}\right] < -2.0$. The bulge is the most likely location of any existing Galactic Population III stars, and an infrared-only variant of this selection is effective enough for the identification of metal-poor stars in the bulge. Indeed, two of confirmed metal-poor stars with $\left[\frac{Fe}{H}\right] < -2.7$ from Schlaufman &Casey (2014) sample are within about 2 kpc of the Galactic center. They increased the number of the most metal-poor stars known in the bulge.

This spectral analysis gives as a result one of the largest sample of very metal-poor stars with homogenously-measured abundances of a significant number of individual elements. Given the large number of spectra to be processed, it is mandatory to use automated techniques for abundance analysis. This sample was used in the following work.

Also, investigations on individual metal-poor stars were done.Bond et al. (2013) studied HD 140283 is an extremely metal-deficient and high-velocity sub-giant in the solar neighborhood, having a location in the Hertzsprung-Russell diagram where absolute magnitude is most sensitive to stellar age. Because it is bright, nearby, unreddened, and has a well-determined chemical composition, this star does not present most of the critical issues in age determinations for globular clusters, for instance. Using the Fine Guidance Sensors on the Hubble Space Telescope, they have measured a trigonometric parallax of 17.15 $\pm$ 0.14 mas for HD 140283. Using modern theoretical isochrones, which include effects of helium diffusion, revised nuclear reaction rates, and enhanced oxygen abundance, together with the precise distance Bond et al. (2013) identified an age of 14.46 $\pm$ 0.31 Gyr. The presented error includes only the uncertainty in the parallax, and is for adopted surface oxygen and iron abundances of [O/H] = -1.67 and [Fe/H] = -2.40. Uncertainties in the stellar parameters and chemical composition, especially the oxygen content, now contribute more to the error budget for the age of HD 140283 than does its distance, increasing the total uncertainty to about $\pm$0.8 Gyr. Within the errors, the age of HD 140283 does not conflict with the age of the Universe, 13.77 $\pm$ 0.06 Gyr, based on the microwave background and Hubble constant, but this star must have formed soon after the Big Bang.

Subsequent work of VandenBerg et al. (2014) derived the most accurate ages for the oldest stars - nearby halo subgiants because their age determination depends almost entirely on just the measured parallaxes and absolute oxygen abundances. In this study, they have used the Fine Guidance Sensors on the Hubble Space Telescope to determine trigonometric parallaxes, with precisions of 2.1% or better, for the Population II subgiants HD84937, HD132475, and HD140283. High-quality spectra have been employed to derive their surface abundances of O, Fe, Mg, Si, and Ca, which are assumed to be 0.1–0.15 dex less than their initial abundances due to the effects of element internal diffusion. Comparisons of isochrones with the three subgiants on the ($\log T_{eff}$, M_V) diagram yielded ages of 12.08 $\pm$ 0.14, 12.56 $\pm$ 0.46, and 14.27 $\pm$ 0.38 Gyr for HD84937, HD132475, and

HD140283, in turn, where each error bar includes only the parallax uncertainty. The total uncertainty is estimated to be $\sim \pm 0.8$ Gyr (larger in the case of the near-turnoff star HD84937). Although the age of HD140283 is greater than the age of the Universe as inferred from the cosmic microwave background by ~ 0.4˜0.5 Gyr, this disagreement is at a level of $< 1\sigma$. Nevertheless, the first Population II stars apparently formed very soon after the Big Bang. (Stellar models that neglect diffusive processes seem to be ruled out as they would predict that HD140283 is ~ 1.5 Gyr older than the universe.) The field halo subgiants appear to be older than globular clusters at similar metallicities: if distances close to those implied by the RR Lyrae standard candle are assumed, HD140283 and HD132475 are older than M92 and M5 by ~ 1.5 and ~ 1.0 Gyr, respectively.

Furthermore, the precisely derived age of very metal-poor stars is an important test of the cosmological age of the Universe (Bond et al. (2013), VandenBerg et al. (2014)). The current best estimate of the age of the Universe is 13.82 ± 0.06 Gyr, based on the latest WMAP derivation of 13.77 ± 0.06 Gyr (Bennett et al. (2013)), in excellent agreement with observations of the CMB using the Planck satellite (Ade et al. (2014)). Recent simulations (e.g., Ritter et al. (2012), Safranek-Shrader et al. (2014)) suggest that the oldest Population II stars probably formed ~ 0.2˜0.3 Gyr after the big bang, depending on how quickly the gas from the first (Population III) supernovae was able to cool and condense, as well on the relevance and impact of the Population III feedback. Precise ages for the oldest and most metal-poor stars can date the onset of star formation (e.g., Bromm &Larson (2004)) following the Big Bang. Moreover, because the oldest stars must be younger than the Universe, precise ages provide a strong test of the consistency between cosmological and stellar physics.

Also, theoretical simulations of galaxy formation (Bullock &Johnston (2005)) have shown that the halo bears the signatures of the Milky Way's assembly from smaller "building block" galaxies. Recent astrometric studies have shown the existence of stellar kinematic signatures that indicate past accretion events (Belokurov et al. (2018); Myeong et al. (2019); Yuan et al. (2020)). That means that kinematics of very metal-poor stars is an important test of the Galaxy formation and evolution theories. Therefore, stars with low metal abundances are also possible members of accreted dwarf galaxies and/or clusters.

1.1.2 Solar twins

In the literature, solar twins are stars that have stellar parameters similar to the Sun (i.e., effective temperature $T_{eff} : T_{eff,\odot} \pm 200$ K; surface gravity $logg : logg_{\odot} \pm 0.20$ dex; metallicity $[Fe/H] : [Fe/H]_{\odot} \pm 0.3$ dex; where $T_{eff,\odot} = 5771$ K, $logg_{\odot} = 4.44$ dex and $[Fe/H]_{\odot} = 0.0$ dex, Ayres et al. (2006)). The similarity to the Sun makes them perfect targets for spectroscopic analysis, in particular, it allows scientists to perform line-by-line differential analysis relative to the Solar spectrum. This spectroscopic analysis cancels out the impact of log gf parameters in the error balance and also reduces the impact of systematics in models and in the spectrum normalization that allows to derive stellar parameters and chemical abundances with extremely high precision (Ramírez et al. (2014), Meléndez et al. (2014), Spina et al. (2016), Spina et al. (2018), Nissen et al. (2020), Casali et al. (2020)). With accurate spectroscopic parameters is possible also to derive precise ages (Nissen et al. (2020), Casali et al. (2020)). Recent studies on solar twins have reached very high precision on stellar parameters and chemical abundances of the order of 0.01

dex in Fe and 0.5 Gyr in age (Meléndez et al. (2009, 2014), Ramírez et al. (2009, 2014), Liu et al. (2016), Spina et al. (2016, 2018)).

With all obtained parameters together we are able to study small variations in chemical abundances with age, age-metallicity relation, assembly history and the Milky Way's chemical evolution in general in unprecedented detail. The level of precision opens the door to a more accurate understanding of the Galactic chemical evolution, unveiling more details even with respect to the large surveys.

1.2 Milky Way formation and evolution

The Milky Way formation and evolution have been an intriguing topic in astronomy for a long time. Taking into account the location of the Sun in it (in the Disk 8.2 kpc from the galactic center), we are able to resolve single stars in the Halo, Disk and even Buldge. It allows us to study Milky Way formation and evolution in detail. And we can recover even small events that have happened during our Galaxy lifetime.

1.2.1 Historical overview

Investigation of the Galaxy formation started from ELS model. It is the popular scenario of the fast monolithic collapse suggested by Eggen, Lynden-Bell and Sandage (ELS model, Eggen et al. (1962)). This result was based on the detected correlation between metallicity [Fe/H] and orbital eccentricity e for old stars in a region a few hundred parsecs around the Sun. Low metallicity stars have very small angular momentum that means that they were formed with circular orbits in rapidly collapsing material. Halo was quickly collapsing to a thin rotating disk and the disk was enriched in heavy elements by subsequent star formation events.

Later Searle &Zinn (1978) pointed out a selection bias at the core of the that ESL results. Data set of old stars were formed from high proper motion stars. They remark that globular clusters cover a big range of metallicities without correlation with distance. This shows the evidence of the formation of the Galaxy through the merging of several small protogalaxies.

Nowadays monolithic collapse scenario is not considered viable anymore for our Galaxy, or only for the restricted component: central bulge. The stellar halo is lighter and less dense than the disk and could not collapse into the disk. The only possible place to collapse into is an old bulge (Gilmore (1996)). But despite the fact that bulge stars are old, some of them have the same metallicity as disk stars and it is not easily explained by this scenario either.

The second theory is the hierarchical scenario which tells that our Galaxy was formed through the hierarchical merging of dark halos. Accretion of baryonic matter occurs later. First, the bulge was formed, then progressively the thin disk. The thick disk could be produced as a consequence of heating induced by small/medium mass accreted companions.

The presence of stellar streams in stellar halo supports the hierarchical scenario (Helmi (2002), Ibata et al. (2002)): they are tidal remains of past merging events (Grillmair (2017)). Nowadays we have a number of confirmed accreted events such as Sagittarius dwarf galaxy, Gaia-Enceladus/Sausage, Sequoia, Helmi stream, and other streams are found to be associated with accreted dwarf galaxies/ globular clusters (Koppelman et al.

(2019)). The halo of the Galaxy could be mostly built from minor mergers. Furthermore, the fact that merging frequency is increasing with increasing redshift tells us that at time of the beginning of the Galaxy formation merging events were more common. That lends further support to the hierarchical scenario.

The last and most successful scenario is Secular Evolution (SE), with slow and continuous external matter accretion. In this theory, the bulge of the Galaxy was formed due to the accretion of disk matter through the bar dynamics. This scenario is in agreement with the observed color gradient and the relation between the color of the bulge and disk studied through statistical analysis of 257 spiral galaxies (Gadotti &dos Anjos (2001)). SE is also supported by the relation between the bulge and disk masses and radii (Courteau et al. (1996)).

Another point is that a radial metallicity gradient independent of luminosity was observed in a large sample of early-type galaxies (De Propris et al. (2005)). This contradicts with monolithic collapse scenario because metallicity changes should follow matter distribution (metallicity gradient is independent of luminosity). Besides, the hierarchical model tells us that there should not be any metallicity gradient.

1.2.2 Bulge and bar

The Bulge is the heart of the galaxy and studying it is a hot topic over the last decade. Firstly, it was considered that the Galactic bulge is a classical bulge, to be more precise, a spheroidal remnant of mergers of primordial structures in a Λ cold dark matter context (ΛCDM; Ortolani et al. (1995), Baugh et al. (1996); Abadi et al. (2003a,b)). However, observations of the Milky Way Bulge (Binney et al. 1991; Bissantz &Gerhard 2002; López-Corredoira et al. 2005) and bulges at higher redshifts (Tacchella et al. 2015; Nelson et al. 2016; Shen et al. 2024) have shown a much more complex structure. So-called pseudo-bulges in comparison with classical bulges are forming from disk stars due to the vertical instability of a stellar bar (Combes et al. 1990). This scenario leads to the formation of a triaxial boxy bar structure, in other words, the Galactic bulge with a boxy/peanut (B/P) shape (Weiland et al. 1994; McWilliam &Zoccali 2010; Wegg &Gerhard 2013; Ness &Lang 2016). It was shown in N-body simulations that this type of bulge forms in barred stellar disk galaxies (Raha et al. 1991; O'Neill &Dubinski 2003; Athanassoula 2005; Shen et al. 2010; Ciambur et al. 2021; Ghosh et al. 2023). Moreover, the fact that fully formed bulges or a high central star formation are observed in galaxies at redshift $z \sim 2$ (Tadaki et al. 2017) suggests that those bulges are assembled before the formation of the bar. Therefore, the main mechanism that can explain the creation of such structures is a fast and strong primordial collapse of gas responsible for at least one rapid star formation episode.

Due to heavy extinction and crowding the Galactic Bulge is challenging to observe. Despite this, several spectroscopic (e.g., BRAVA, Rich et al. (2008), Kunder et al. (2012), Gaia-ESO, Gilmore et al. (2012), APOGEE, Majewski et al. (2017), ARGOS, Freeman et al. (2013), GIBS, Zoccali et al. (2014)) and photometric (the VVVX survey, Minniti et al. (2010)) surveys have been developed to investigate the central part of the Galaxy. The result of these observations confirms the complexity of the Bulge. Stars from the Bulge region have the bimodal metallicity distribution function (Hill et al. 2011; Bensby et al. 2011; Uttenthaler et al. 2012; Gonzalez et al. 2015; Rojas-Arriagada et al. 2017, 2019; Rojas-Arriagada et al. 2020; Zoccali et al. 2017; Queiroz et al. 2020, 2021; Johnson et al. 2020, 2022). It indicates that there can be two (or more) stellar populations: a metal-rich

Method	Bar age	Article
Distribution of infrared carbon stars	$\sim$ 2 Gyr	Cole &Weinberg (2002)
Observations of luminous face-on spiral galaxies	$\sim$ 8 Gyr	Sheth et al. (2008)
Zoom-in cosmological simulations	$\sim$ 8 Gyr	Kraljic et al. (2012)
Gaia Data Release 2 set of long-period variables	8-9 Gyr	Grady et al. (2020)

Table 1.1: Studies of the Milky Way bar formation

population with the average metallicity $[Fe/H] \sim 0.25$ dex and a metal-poor population centered at $[Fe/H] - 0.3$ dex. Talking about kinematics metal-rich population is rapidly rotating and dynamically cold and the metal-poor one is dynamically hotter and rotating more slowly. Moreover, the metal-rich population shows a vertex deviation that can be caused by the Milky Way bar (Zhao et al. 1996; Soto et al. 2007; Babusiaux et al. 2010), while the metal-poor population follows a spheroid kinematics like Thick disk stars. Also, a proposed by Portail et al. (2017) chemodynamical model shows that the dynamical properties of metal-rich stars ($[Fe/H] \geq -0.5$ dex) are strongly barred and consistent with a common disk origin, while the kinematic of metal-poor stars ($[Fe/H] < -0.5$ dex) varies more with metallicity, which can lead to the conclusion that they are coming from different stellar populations.

Since the Galactic bar produces a significant impact on the dynamic of the stars in the bulge (Baba &Kawata 2020) and in the inner disk (Minchev et al. 2016), the bar formation has become an important topic to study in terms of the Milky Way history. As already mentioned, the time of the formation of the Galactic bar is still under debate (Tab. 1.1). The distribution of infrared carbon stars shows that the estimated bar age is $\sim$ 2 Gyr (Cole &Weinberg 2002). In observations of luminous face-on spiral galaxies, the variation of the fraction of galactic bars with a redshift shows that in spiral galaxies with masses similar to the Milky Way the bar forms around $z = 1$ ($\sim$ 8 Gyr; Sheth et al. (2008)). The same result was obtained also from the zoom-in cosmological simulations (Kraljic et al. 2012). Also, a recent study of the set of long-period variables (Gaia Data Release 2) estimates that the bar formation happened 8 - 9 Gyr ago (Grady et al. 2020), though the long-period variables in the bar are generally more metal-rich and hence may be older at a given luminosity. It is worth mentioning that the age of the bar stars does not necessarily correlate with the age of the bar itself, since the bar can capture stars that were formed before its formation, moreover there could be no star formation in the bar at all (Anderson et al. 2020). By the scenario proposed by Chiba et al. (2021) and Chiba &Schönrich (2021, 2022) due to dynamical friction from the dark matter halo the bar experiences angular momentum loss, which decreases its pattern speed, Ω_p (Hernquist &Weinberg 1992; Debattista &Sellwood 2000; Martinez-Valpuesta et al. 2006). When the bar slows down, the resonance moves outward in radius throughout the disk, sequentially capturing and dragging new stars. A fraction of stars that are trapped in the corotation radius can then be captured by the bar. As a consequence, stars in the bar could be born in other parts of the Galaxy or even the Universe and then captured from the disk showing the chemical composition and age of the origin where they were initially born.

The first evolution model of the Bulge was proposed by Matteucci &Brocato (1990). In their scenario the bulge forms through the strong and fast ($\sim$ 0.5 Gyr) burst of star formation with initial mass function top-heavier than in the solar neighborhood which creates a longer plateau in the [α/Fe] ratio than in the solar vicinity. Later it was observation-

ally confirmed by McWilliam &Rich (1994) and more precise parameters for Matteucci &Brocato (1990) model were found (Ballero et al. 2007; Cescutti &Matteucci 2011). Also, Grieco et al. (2012, 2015); Tsujimoto &Bekki (2012) tried to reproduce the bimodality in the metallicity distribution function by second infall and/or accretion episode. Later Matteucci et al. (2019) were able to reproduce the metal-rich population with the pause in star formation $\sim$ 250 Myr where metal-rich stars form from the second burst or are captured from the inner disk by the bar.

1.2.3 Thin and Thick disk

The Milky Way disk is a complex structure. Its exact formation and evolution together with the related physical and dynamical processes are still under debate. Recently, several surveys have provided statistically very large datasets of stars with detailed chemical abundances: e.g. RAVE (Steinmetz et al. 2020; Steinmetz et al. 2020), Gaia-ESO (Gilmore et al. 2012), APOGEE (Majewski et al. 2017; Ahumada et al. 2020; Jönsson et al. 2020), LAMOST (Cui et al. 2012; Zhao et al. 2012) or GALAH (De Silva et al. 2015; Buder et al. 2018; Buder et al. 2021). Combined with the very precise Gaia astrometry (Gaia-Collaboration et al. 2018; Gaia-Collaboration et al. 2020; Lindegren et al. 2018; Lindegren et al. 2021a,b) they allow us to study the formation of the Galactic disc with an unprecedented level of detail. However, even taking into account this amount of data, the origin and the link between the Thin and Thick disk, the two traditionally assumed components of the Milky Way disc, are not well established.

In the Solar neighborhood, spectroscopic studies have shown that Thick disk stars are older and have a higher [α/Fe] ratio than Thin disk stars (Fuhrmann 1998, 2004, 2008, 2011; Prochaska et al. 2000; Bensby et al. 2005; Bensby et al. 2007; Haywood et al. 2013). Moreover, in the ([Fe/H], [α/Fe]) plane Thin and Thick disks separate into two sequences. A low-[α/Fe] represents the Thin disk and high-[$alpha$/Fe] - Thick disk (Fuhrmann 1998; Haywood et al. 2013). Also, the velocity dispersion is larger in the Thick disk and it rotates slower compared to the Thin disk (Soubiran et al. 2003; Kordopatis et al. 2013; Robin et al. 2017). Although two disks belong to different stellar populations some authors claim that these populations consist of multiple sub-populations that smoothly span the observed range of properties (Norris 1987; Bovy et al. 2012, 2016; Ted Mackereth et al. 2017).

If we look further than the Solar vicinity, Thin and Thick disk still appear to be two distinct populations in the ([Fe/H], [α/Fe]) plane (Nidever et al. 2014; Hayden et al. 2015; Queiroz et al. 2020) but their pattern changes with galactic radius (R) and with the modulus of the height above the Galactic plane (|Z|). The high-α population is present up to $R \sim 10 - 12$ kpc and then gradually vanishes at larger radii, meaning that the Thick disk has a shorter scale length compared to the Thin disk (Bensby et al. 2011; Bovy et al. 2012; Cheng et al. 2012). Alternatively, the low-α sequence is observed at all radii but its morphology changes with the location in the Galaxy. In the inner disk ($R < 6$ kpc) Hayden et al. (2015); Bovy et al. (2019) and Lian et al. (2020); Lian et al. (2020a) have found Thin and Thick disk stars merged and look like a single sequence, while Rojas-Arriagada et al. (2019) and Queiroz et al. (2020) observed two distinct sequences. Moreover, the observed metallicity gradient in the Thin disc is changing with the Galatic radius. It is flat in the inner disc in contrast with the gradient observed in the external regions (R$>$ 6kpc) suggesting a different chemical evolution of the two regions (Haywood

et al. 2019).

In the literature, different models proposed to explain observed α-bimodality in the disk and the formation of the Thick disk. One of the first chemical evolution models that try to explain metallicity-α-elements distribution is the two-infall model (Chiappini et al. 1997; Spina et al. 2018). The Thick disc is formed at early times through a collapse of primordial gas followed by a quiescent period where the star formation is quenched. After that, a new episode of fresh gas accretion takes place, the star formation resumes and the Thin disc is formed in an inside-out manner. A recent model by Lian et al. (2020b, 2021); Lian et al. (2020); Lian et al. (2020a) suggests that there were two episodes of gas accretion to explain the bimodality/dichotomy in the ([Fe/H], [α/Fe]) plane at different Galactic locations. Two gas accretion phases ignite the star formation and they are separated by a prolonged period of low-level star formation. Haywood et al. (2018); Haywood et al. (2019) propose that the Thick disk was formed from a turbulent gas-rich environment which is followed by a low level of star formation. The inner Thin disk was formed from the gas left from the Thick disk without any accretion. In Snaith et al. (2015a) inner and outer disks follow different chemical evolution. The α-bimodality observed in the inner disc ($R \leq 6$ kpc) is produced from the quenching phase that occurred between the formation of the inner Thin disc and the Thick disc (Haywood et al. 2016). In the external disk, the high-α population is produced during the Thick disk formation, and the low-α sequence, instead, comes from the gas left over from the Thick disk formation with a radially dependent dilution (Haywood et al. 2019). In their scenario, the sequence itself can be reproduced only by radially dependent chemical evolution, not at a single radius.

In a recently presented set of chemodynamical Milky Way-type galaxy formation simulations by Khoperskov et al. (2021) is shown that the high-α sequence is early formed from a burst of star formation in a turbulent, compact gaseous disc which forms a Thick disc. On the other side, the low-α sequence comes from a quiescent star formation supported by the slow accretion of enriched gas onto a radially extended Thin disk. The surrounding gaseous halo is enriched by stellar feedback-driven outflows during the formation of the Thick disk and then subsequently halo feeds the disc on a longer time scale. Khoperskov et al. (2021) confirm the scenario proposed by Haywood et al. (2019) by showing that the formation of the low-α sequence is a radially dependent process, which explains the *alpha*-dichotomy. However, these simulations do not include mergers.

The chemical evolution model by Schönrich &Binney (2009a,b) reproduces the α-bimodality in the ([Fe/H], [α/Fe]) plane observed in the Solar vicinity through continuous star formation. In particular, the model includes the radial flow of gas and radial migration of stars as the main mechanisms that carry kinematically hot stars from the inner disc to the Solar neighborhood and create the Thick disc. Also, Sharma et al. (2021) found the same results as Schönrich &Binney (2009a,b) and extended them to different locations across the Milky Way.

Nowadays we can simulate the Milky Way mass galaxies with high enough resolution that allows us to study the formation scenario of distinct discs self-consistently in a fully cosmological context. These simulations predict that thin stellar discs form in an inside-out, upside-down manner (Brook et al. 2012; Bird et al. 2013). However, the formation mechanism of the α-bimodality in the ([Fe/H]-[α/Fe]) plane is still under debate. Some authors (Brook et al. 2012; Grand et al. 2018; Noguchi 2018; Buck 2020; Agertz et al. 2021) have invoked gas-rich mergers as the main origin, but the formation channels of chemically

distinct discs differ. For example Grand et al. (2018) found two main paths to produce the α-dichotomy in different regions of the galaxies: an early centralised starburst mechanism that is relevant for the inner disc; and a shrinking disc mechanism that is relevant for the outer disc. For the centralised starburst pathway, an early and intense high-[α/Fe] star formation phase induced by gas-rich mergers is followed by a more quiescent low-[α/Fe] star formation. For the shrinking disc pathway, an early phase of high-[α/Fe] star formation is followed by a shrinking of the gas disc due to a temporarily lowered gas accretion rate, after which disc growth resumes. Otherwise, Clarke et al. (2019) claimed that the dichotomy arises from rapid star formation in high redshift clumps and the two [α/Fe]-sequences form simultaneously early on in the evolution of the Milky Way, resulting in overlapping ages.

1.2.4 Halo

During its lifetime the Milky Way destroys and accretes lower-mass systems - "building blocks". Smaller of them mainly contain dark matter, larger ones also contain stars. The Milky Way halo is made of these stars (Bullock &Johnston 2005; Cooper et al. 2010) and they keep the signatures of their initial progenitor orbits in their kinematics (Helmi &Tim de Zeeuw 2000; Belokurov 2013; Bland-Hawthorn &Gerhard 2016; Helmi 2020). It means that halo stars are a great source to study the Milky Way assembly history.

Let's first start with a theoretical point of view. The ΛCMD model predicts that there are many more small accretion than large (Moore et al. 1999; Jenkins et al. 2001; Gao et al. 2004; Tinker et al. 2008). For example, cosmological N-body simulations (Fakhouri et al. 2010) show that a Milky Way-mass halo (10^{12} $M_{\odot}$) typically undergoes $N \sim 30$ minor mergers (mass-ratio between 1:3 and 1:100) and $N \sim 3$ major mergers (mass-ratio >1:3) since redshift $z = 10$. And it is worth mentioning that the biggest contribution to the star mass of the halo comes from the 1-2 major mergers, minor mergers mainly contribute to the dark matter halo (Purcell et al. 2007; Deason et al. 2016; Bullock &Boylan-Kolchin 2017). The more detailed simulations, where it becomes possible to track spatially each accretion, have shown that the contribution from major mergers mainly plays a role in the formation of the inner halo $\lesssim 20-50$ kpc (Bullock &Johnston 2005; De Lucia &Helmi 2008; Cooper et al. 2010; Monachesi et al. 2019; Fattahi et al. 2020; Horta et al. 2023). It happens because massive systems undergo a dynamical friction that rapidly drags them inwards. As a consequence, most of the inner Stellar halo stars are coming from the same dwarf galaxy progenitor. The outer halo is instead dominated by the accreated low-mass systems. Their low binding energy allows them to be splayed out from the Galactic center as streams or overdensities. Also, major merger parts that were disrupted in a more circular orbit can reach the outer halo (Hendel &Johnston 2015; Pop et al. 2018). It means that in comparison with the inner halo, the outer halo is more likely to form from a larger variety of progenitors (Fattahi et al. 2020).

From the chemical point of view, we should start by studying the commonly used ([Fe/H], [α/Fe]) relation. From the star chemical evolution, we know that the most effective source of α-elements production into the interstellar medium is supernovae type II (core-collapse) which starts working on a timescale ∼Myr (also producing iron). However, the additional iron producer - supernovae type Ia starts working on a timescale ∼Gyr (Kobayashi et al. 2006; Maoz &Mannucci 2012; Kobayashi et al. 2020). This delay in additional iron production creates a "knee" in ([Fe/H], [α/Fe]) plane (Tinsley 1979). The

more massive systems are more efficient in retaining and building up the metal content, hence the metallicity of the "knee" correlates with the mass of the system (Hendricks et al. 2014; De Boer et al. 2014; Mason et al. 2024). Venn et al. (2004) have found that the "knee" for Milky Way halo stars is relatively metal-rich (but not as rich as for Milky Way disk stars) which leads to the conclusion that the halo could experience a massive merger. However, it is worth mentioning that the chemical composition of the halo stars differs from massive dwarf galaxies such as Large Magellanic Cloud and Sagittarius. It could have happened because the major mergers occurred in the early times of the Milky Way assembly and today's chemical composition of massive satellites differ because of their star formation over the lifetime.

With the new era of Gaia (Prusti et al. 2016; Gaia Collaboration et al. 2022b) we are able to study the halo in great detail from the kinematical point of view (Helmi 2020; Deason &Belokurov 2024). Now we can distinguish different structures in the halo by searching for over-densities in integral of motion space (Helmi &Tim de Zeeuw 2000).

The halo in the solar neighborhood is dominated by one major merger Gaia-Enceladus/Sausage (Helmi et al. 2018; Belokurov et al. 2018). Its stellar mass is in the range of $\sim 10^8 - 10^{10} M_\odot$ becoming smaller for the later works (Helmi et al. 2018; Vincenzo et al. 2019; Feuillet et al. 2020; Mackereth &Bovy 2020; Lane et al. 2023) and the estimated accretion time is ~ 10 Gyr ago (Helmi et al. 2018; Gallart et al. 2019; Bonaca et al. 2020; Montalbán et al. 2021). However, there were also detected other dynamical substructures (Koppelman et al. 2019; Naidu et al. 2020; Yuan et al. 2020; Horta et al. 2021; Lövdal et al. 2022; Ruiz-Lara et al. 2022; Dodd et al. 2023) and the retrograde halo is mainly populated by three main accretion events; Gaia-Enceladus/Sausage, Sequoia and Thamnos (Tab. 1.2).

The Sequoia is a loosely bound retrograde substructure (Myeong et al. 2019; Matsuno et al. 2019, 2022) which was accreted around 9 Gyr ago with the stellar mass of $\sim 5 \times 10^7 M_\odot$, high total energy ($E_n$). In chemistry the metal-poor part of Sequoia is chemically completely different from Gaia-Enceladus/Sausage (Myeong et al. 2019; Matsuno et al. 2022) but for the metallicity > -1.5 dex Sequoia is by $\sim 10-20\%$ contaminated by Gaia-Enceladus/Sausage stars (Matsuno et al. 2022; Ceccarelli et al. 2024). It happens because massive mergers like Gaia-Enceladus/Sausage can populate different regions in the dynamical space, depending on its initial orbital configuration and morphology (Koppelman et al. 2020; Naidu et al. 2021; Amarante et al. 2022).

If Sequoia represents a high-E_n retrograde halo, Thamnos represents a low-E_n retrograde halo. Initially, Thamnos was found as two accreted structures - Thamnos 1 and 2 (Koppelman et al. 2019) who share the same progenitor (Ruiz-Lara et al. 2022) with the stellar mass of $5 \times 10^6 M_\odot$ (Koppelman et al. 2019). Thamnos 2, which is the less retrograde and more bound substructure, has signatures to be contaminated by in-situ stars due to less negative angular momentum (L_z). Firstly, Thamnos 2 contains stars with the average metallicity 1.3 dex that are Al-enhanced (Koppelman et al. 2019; Horta et al. 2021) and, secondly, Thamnos 2 is more metal-rich than Thamnos 1 (Ruiz-Lara et al. 2022; Cui et al. 2012). Later with the new Gaia DR3 release Thamnos has been identified as one single substructure (Dodd et al. 2023), but its chemistry still shows a mix of stellar populations, including contamination from in-situ components and probably also from Gaia-Enceladus/Sausage.

In the end, the local halo also hosts an in-situ-originated component. In the color-magnitude diagram, the local halo separates into two populations (Babusiaux et al.

Accretion event	Stellar mass	Accretion time
Gaia-Enceladus/Sausage	$\sim 10^8 - 10^{10} M_\odot$	~ 10 Gyr ago
Sequoia	$\sim 5 \times 10^7 M_\odot$	~ 9 Gyr ago
Thamnos	$\sim 5 \times 10^6 M_\odot$	

Table 1.2: Acretion event contributed to the retrograde Milky Way halo

2018). The blue sequence represents the accreted component mainly dominated by Gaia-Enceladus/Sausage debris and the red sequence is considered to be the heated thick disk stars (Haywood et al. 2018). If the thick disk was already formed when the Gaia-Enceladus/Sausage was accreted, the thick disk stars could be heated onto halo-like orbits producing what we now call the hot thick disk (HTD, hereafter) or the Splash (Helmi et al. 2018; Gallart et al. 2019; Belokurov et al. 2020).

Also, an ancient in-situ halo structure - Aurora was found using [Al/Fe] (Belokurov &Kravtsov 2022), and hypothesized to have formed during a period of chaotic (pre-disc) evolution at the beginning of the Milky Way assembly. This population has high [Al/Fe] ratio which could be reached in rapidly star-forming and self-enriching galaxy before supernova type Ia (SN Ia) starts to contribute significantly and dilutes the [Al/Fe]. For example, these high [Al/Fe] values are not reached before the SN Ia kicks in in dwarf galaxies with slower star formation (Hawkins et al. 2015; Belokurov &Kravtsov 2022). The chemical abundances of the Aurora population also suggests that the proto-Milky Way formed with a large contribution from massive star clusters (Belokurov &Kravtsov 2022; Myeong et al. 2022). However, Horta et al. (2021, 2024) show that this proto-Milky Way/Aurora can be chemically indistinguishable from an early massive merger event.

1.3 Problematics

Summing up all the knowledge of the Milky Way formation and evolution we remain with a lot of unsolved problems and unanswered questions. In this work, I am answering some of them.

Firstly, by deriving the age of very metal-poor stars - the oldest objects in The Milky Way - we put a constraint on the age of the Milky Way and the Universe in general.

Secondly, by studying the correlation between different chemical elements in very metal-poor stars we understand some properties of chemical and physical processes in the first Population III supernovae.

Thirdly, by combining metallicity and age we can study the age-metallicity relation - one of the most important trends in the history of our Galaxy - where the metallicity traces the star formation efficiency and the age tells us about the timing of it.

Finally, by adding the kinematical parameters to the chemical abundances we can also reconstruct the chemical and dynamical evolution of the Milky Way. Moreover, by combining age, kinematics, and chemistry, we also can obtain the origin of the stars and retrace the assembly history of our Galaxy. Additionally, by using different targets like very metal-poor stars and solar twins we cover different stages in the Milky Way formation and evolution in different parts of the Galaxy.

Thesis outline

This thesis is organized as follows:

In Chapter 2, I introduce an automatic age determination technique for single stars which I apply to the dataset of very metal-poor stars from Barklem et al. (2005). For each star, I randomly select initial parameters inside the Gaussian distribution 10.000 times. For each of these random selections, I perform an isochrone fitting in a color-magnitude diagram where I derive age as the age of the closest isochrone. And then I fit the resulting age distribution with the Gaussian function. I consider its mean as the age of the star and its sigma as age uncertainty. To achieve low uncertainties in age determination I searched for the best estimate for each initial parameter: photometry, distance, metallicity, reddening and α-enhancement. Then I studied how chemical composition affects the photometry in different filters, hence the age determination. Also, I tested obtained results with the ages of globular clusters and studied before very metal-poor sturs. Finally, I studied the age metallicity relation in the metal-poor regime.

In Chapter 3, I derive the origin of the very metal-poor stars by combining age, chemistry and kinematics. I calculate the dynamical properties using most modern Galactic axisymmetric and non-axisymmetric potentials. I study the Al-Mg map to derive its origin from the chemical point of view. Also, I investigate dynamical parameters to derive origine from the kinematics. I compare the kinematical properties of the stars with the kinematical properties of known accretion events to check the possibility for these stars to be accreated, and I double-check it with the chemistry and age. Finally, based on obtained results I propose the Milky Way formation and evolution scenario.

In Chapter 4, I change the target and work with solar twins. I perform the line-by-line differential analysis with respect to the Sun to obtain high-precision stellar parameters and abundances. Together with that, I derive age using isochrone fitting technique for single stars (Chapter 2) in effective temperature (T_{eff}) - surface gravity ($logg$) space. I calibrate metallicity to take into account the effect of atomic diffusion at the solar age. Additionally, I compute kinematical parameters and birth radius. Having accurate ages and metalicity I study age-metallicity relation for solar twins in the Thin disk around the Sun. Especially the question if there are two populations or not. Also, I study chemical trends to recover

the chemical evolution of the Thin disk in the Solar vicinity.

Finally, Chapter 5 summarizes my conclusions and outlook.

Chapter 2

Very metal-poor stars in the solar vicinity: age determination

Based on:
Plotnikova A., Carraro G., Villanova S., Ortolani S.,
"Very metal-poor stars in the solar vicinity: age determination", 2022, ApJ 940, 159

Abstract

The ages of the oldest and most metal-poor stars in the Milky Way bear important information on the age of the Universe and its standard model. We analyze a sample of 28 extremely metal-poor field stars in the solar vicinity culled from the literature and carefully determine their ages. To this aim, we critically make use of Gaia data to derive their distances and associated uncertainties. Particular attention has been paid to the estimate of the reddening and its effect on the derivation of stellar ages. We employed different reddenings and super-impose isochrones from different sources in the stars color-magnitude diagram built up with different photometric systems. We highlight subtle metallicity effects when using the Johnson photometry for low metallicity stars and finally adopt Gaia photometry. An automatic fitting method is devised to assign ages to each individual star taking into account the uncertainties in the input parameters. The mean age of the sample turns out to be 13.9 ± 0.5 Gyr using Padova isochrones, and 13.7 ± 0.4 Gyr using BASTI isochrones. We found also a group of very metal-poor stars ($\left[\frac{Fe}{H}\right]$: -2.7 – -2.0 dex) with relatively young ages, in the range 8 – 10 Gyr.

2.1 Introduction

Stars with extremely low metal abundance are of particular astrophysical and cosmological interest because they probe very early times in the evolution of the Universe and its Galactic components. Through the investigation of the age and chemical composition, we can obtain important constraints on the evolution of the Milky Way, set up a lower limit to the age of the Universe (Bond et al. (2013), VandenBerg et al. (2014)), and understand the chemical properties of the first Population III supernovae in the nascent Milky Way (Frebel &Norris (2015)).

Over the years, several spectroscopic campaigns have been conducted to study the chemical composition of very metal-poor stars (Christlieb et al. (2004), Cayrel et al. (2004), Barklem et al. (2005), Schlaufman &Casey (2014), Limberg et al. (2021), etc.).

The most recent investigations of the age of metal-poor stars (Bonaca et al. (2020), Carter et al. (2021)) showed that they are on average old (12.0 ± 1.5 Gyr for turnoff stars). However, both authors discovered the presence of very metal-poor stars with relatively young ages 8 - 10 Gyr (3 stars in Bonaca et al. (2020), 1 star in Carter et al. (2021)).

The current best estimate of the age of the Universe is 13.77 ± 0.06 Gyr, based on the latest WMAP derivation (Bennett et al. (2013)), and it is in excellent agreement with observations of the cosmic microwave background (CMB) using the Planck satellite (Ade et al. (2014)). Recent simulations (e.g., Ritter et al. (2012), Safranek-Shrader et al. (2014)) suggest that the oldest Population II stars probably formed $\sim 0.2 - 0.3$ Gyr after the Big Bang, depending on how quickly the gas from the first (Population III) supernovae was able to cool down and condense, as well as on the relevance and impact of the Population III stellar feedback. Precise ages for the oldest and most metal-poor stars can date the onset of star formation (e.g., Bromm &Larson (2004)) following the Big Bang. Since the oldest stars must be younger than the Universe, precise ages provide a strong test of the consistency between cosmological and stellar physics.

Moreover, the derived age together with high precision spectroscopic measurements of metallicity can help us to reconstruct the age-metallicity relation (AMR) - one of the main observational constraints for any Milky Way formation and evolution model. The first AMR in the solar neighborhood was obtained by Twarog (1980) and it shows an average decrease of the metallicity with the age. Twarog (1980) concluded that the AMR can be used to estimate the star formation rate via comparison with theoretical models. That means that the AMR is an important tracer of the star formation history of galaxies. An extension of the AMR to the very metal-poor tail will help to understand the early stages of star formation in the Milky Way and in the Universe.

On the other hand, the wide distribution in metallicity in the solar neighborhood, at any given age, suggests that stars have been moving away from their birth locations over time (radial migration) (Grenon (1972), Grenon (1989)). The main mechanisms of radial migration are: transient spiral modes mostly at the co-rotation resonance (Sellwood &Binney (2002)), and non-axisymmetric perturbations to the potential such as bars or galaxy interactions (Bird et al. (2012), Roškar et al. (2008), Quillen et al. (2009)).

A recent intriguing finding, described in Feuillet et al. (2018), is that the youngest stars are not the most metal-rich as previously expected from pure gas enrichment processes. There are two possible reasons for such an occurrence: 1) two modes of star formation, where part of the metal-rich gas is diluted to form stars that are subsequently more metal-poor, or 2) migration of the old, metal-rich stars from the inner to the outer regions of the Galaxy. That means that non-linear patterns in AMR are correlated with the specific events in star formation and dynamical evolution of the Galaxy.

In this study, ages and chemical compositions of a sample of very metal-poor stars are investigated. Our main goal is to compare them with the age of the Universe (13.77 ± 0.06 Gyr) based on data on the CMB, baryon acoustic oscillations, and Hubble constant (Bennett et al. (2013)). We also investigate the chemical composition of these stars to retrieve information about the first Population III supernovae, the chemical composition of the nascent Milky Way, and the AMR behavior in the very metal-poor regime.

2.2 Data

As the main target of our research, we used metal-poor stars from the Hamburg vs. ESO R-process Enhanced Star (HERES) survey, spectroscopically studied by Barklem et al. (2005). Their "snapshot" spectra cover a wavelength range of 3760 – 4980 Å and have an average signal-to-noise ratio of S/N $\sim$ 54 per pixel over the entire spectral range. A 2″ slit is employed giving a minimum resolving power of $R \approx 20000$. From the "snapshot" spectra the elemental abundances of moderate precision (absolute rms errors of order 0.25 dex, relative rms errors of order 0.15 dex) have been obtained for 22 elements: C, Mg, Al, Ca, Sc, Ti, V, Cr, Mn, Fe, Co, Ni, Zn, Sr, Y, Zr, Ba, La, Ce, Nd, Sm, and Eu.

We chose this particular data set because of its careful and detailed chemical analysis. It is indeed a unique data set under this point of view. Besides, all stars in the data set under investigation are very metal-poor and this gives us the real opportunity to study the very beginning of the formation and evolution of our Galaxy. Additionally, we wanted to test the cosmological age of the Universe and very metal-poor stars are the best candidates for this purpose.

The final sample of stars analysed in Barklem et al. (2005) contains 253 stars built up with the following criteria:

- No strong molecular carbon features in spectra.
- Metallicity cut-off: [Fe/H] < -1.5
- Temperature cut-off: $T_{eff} > 4200$ K
- No spectroscopic binaries or rotators

We complemented spectroscopic data with Gaia (G, G_{BP}, G_{RP}) and Johnson (B, V, I) photometry obtained from the Gaia archive[1] and SIMBAD catalog[2]. The distribution in the galactic plane is shown in Fig.2.1. Out of these 253 stars only 28 were TO stars for which we could measure good ages (see Section 4.3.2). Coordinates, photometry, interstellar absorption, distance, temperature and chemical abundances of these 28 stars are presented in Tab.2.1. See Sections 2.4 and 4.2.2 for interstellar absorption and distance determination. The main characteristics of the data set:

- Location in the space: Galactic Halo $|b| > 20^o$.
- Most of the stars have magnitudes in the range $12 < G < 17$.
- Distance (estimated using Gaia Data Release 3 parallaxes) in the range $0 < d < 30$ kpc.
- Metallicity in the range $-3.8 < [Fe/H] < 1.5$ dex.
- All stars are α-element enhanced.
- All targets are single stars. Spectroscopic binaries were already removed by Barklem et al. (2005). We checked, however, El-Badry et al. (2021) for spatially resolved binaries. No overlap was found.

[1] https://gea.esac.esa.int/archive/
[2] http://simbad.u-strasbg.fr/simbad/sim-fbasic

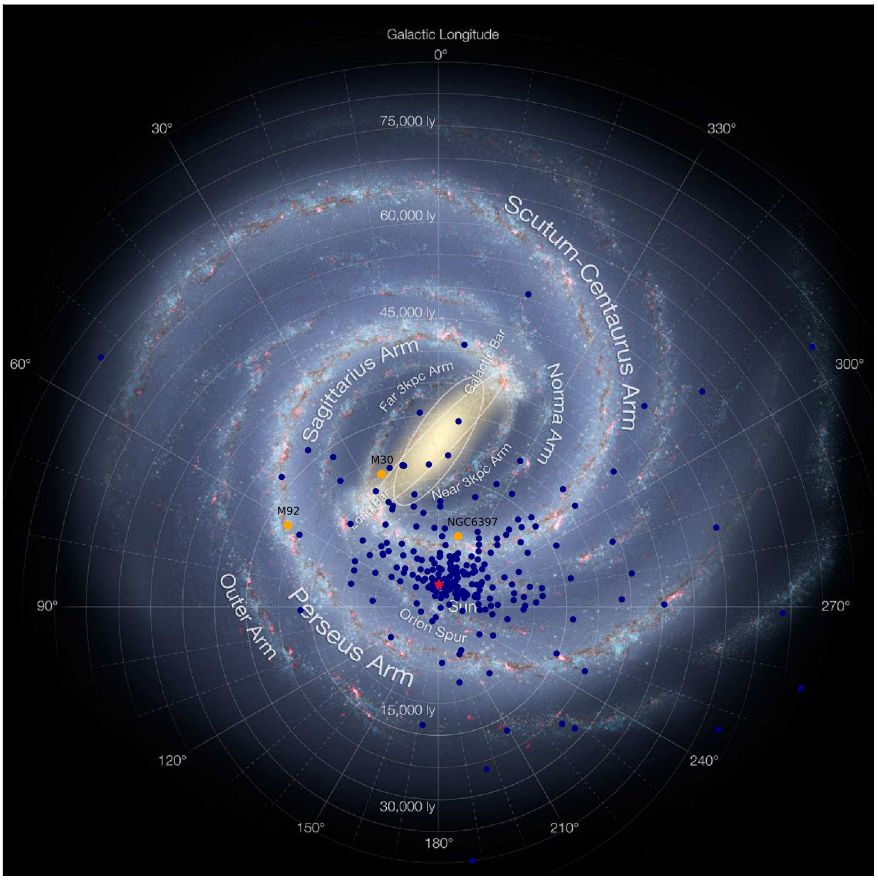

Figure 2.1: Location of 253 very metal-poor stars (blue) in Galactic plane. Yellow dotes are metal-poor globular clusters: NGC 6397, M 30, M 92. Red stars are stars: HD 84937, HD 132475, and HD 140283 (VandenBerg et al. (2014))

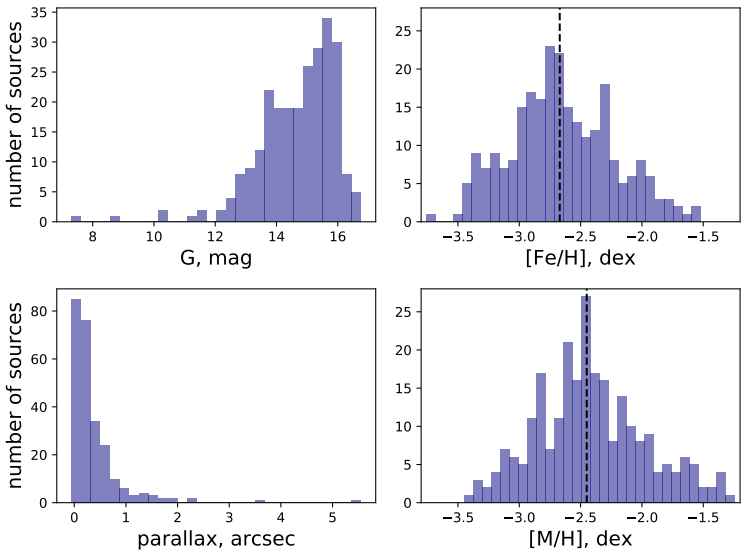

Figure 2.2: Distribution of very metal-poor stars in G-band (Gaia DR3) - *top left*, in parallax Gaia DR3 - *bottom left*, in total metallicity *top right*, in metallicity - *bottom right*, vertical dashed line is the metallicity mean.

ID	RA	DEC	B	V	I	G	G_{BP}	G_{RP}	A_V	d	T_{eff}	[Fe/H]	[C/Fe]
	J2000	J2000	mag	mag	mag	mag	mag	mag	mag	pc	K	dex	dex
HE_0023-4825	00 25 50.31	-48 08 27.01	14.298	13.830	13.161	13.667	13.945	13.218	0.032	1164	5816	-2.06	0.31
HE_0109-3711	01 11 38.40	-36 55 17.11	16.668	16.290	15.691	16.160	16.400	15.757	0.025	3662	6156	-1.91	0.31
HE_0231-4016	02 33 44.39	-40 03 42.72	16.494	16.090	15.475	15.939	16.185	15.532	0.036	2634	5972	-2.08	1.36
HE_0340-3430	03 42 04.76	-34 20 50.10	···	14.783	14.189	14.657	14.910	14.238	0.031	1780	5914	-1.95	0.06
HE_0430-4404	04 31 38.10	-43 57 48.71	···	15.724	15.166	15.629	15.868	15.236	0.035	1569	6214	-2.07	1.44
HE_0447-4858	04 49 01.00	-48 53 36.15	16.687	16.254	15.624	16.140	16.398	15.727	0.038	3261	5995	-1.69	0.04
HE_0501-5139	05 02 48.21	-51 35 36.30	16.573	16.094	15.475	15.980	16.250	15.543	0.059	4539	5861	-2.38	0.40
HE_0519-5525	05 19 59.15	-55 22 41.81	15.570	15.034	14.284	14.862	15.171	14.374	0.066	2376	5580	-2.52	0.29
HE_0534-4615	05 35 52.94	-46 13 35.97	···	15.056	14.317	14.896	15.231	14.382	0.062	2266	5506	-2.01	0.13
HE_0938+0114	09 40 43.20	+01 00 29.51	···	···	···	10.344	10.560	9.964	0.034	180	6777	-2.51	0.65
HE_1052-2548	10 55 20.53	-26 04 48.03	13.492	13.188	12.541	13.115	13.364	12.699	0.127	675	6534	-2.29	0.51
HE_1105+0027	11 07 49.50	+00 11 38.34	16.038	15.646	15.018	15.594	15.852	15.166	0.005	3162	6132	-2.42	2.00
HE_1225-0515	12 28 12.42	-05 31 40.63	···	15.584	14.947	15.524	15.767	15.118	0.005	2410	6210	-1.96	0.52
HE_1330-0354	13 33 10.67	-04 10 05.80	15.248	15.000	14.380	14.937	15.169	14.537	0.082	1716	6257	-2.29	1.05
HE_2250-2132	22 53 40.48	-21 16 23.96	14.905	14.392	13.662	14.220	14.526	13.735	0.027	1780	5705	-2.22	0.41
HE_2347-1254	23 50 10.01	-12 37 50.46	13.839	13.358	12.779	13.248	13.499	12.833	0.064	783	6132	-1.83	0.27
HE_2347-1448	23 49 58.34	-14 32 15.60	15.692	15.226	14.615	15.109	15.374	14.672	0.050	3062	6162	-2.31	0.50
HE_0244-4111	02 45 57.45	-40 59 06.81	15.531	15.025	14.302	14.839	15.141	14.356	0.075	2380	5624	-2.56	0.25
HE_0441-4343	04 43 20.43	-43 38 20.51	···	15.559	14.835	15.388	15.695	14.904	0.047	3511	5629	-2.52	0.33
HE_0513-4557	05 15 12.21	-45 54 10.46	16.279	15.743	15.045	15.609	15.913	15.133	0.038	3602	5629	-2.79	0.39
HE_0926-0508	09 28 55.35	-05 21 40.48	12.340	12.194	11.617	12.126	12.357	11.735	0.086	457	6249	-2.78	0.62
HE_1006-2218	10 09 00.69	-22 33 30.00	···	13.773	13.197	13.717	13.936	13.345	0.102	928	6638	-2.69	9.99
HE_1015-0027	10 17 35.70	-00 42 24.30	15.621	15.342	14.701	15.271	15.519	14.846	0.145	1886	6315	-2.66	9.99
HE_1120-0153	11 22 43.39	-02 09 36.69	12.210	11.789	11.036	11.646	11.884	11.242	0.110	509	6191	-2.77	0.63
HE_1126-1735	11 28 51.39	-17 51 42.82	···	15.965	15.232	15.890	16.166	15.445	0.132	4118	5689	-2.69	0.23
HE_1413-1954	14 16 04.71	-20 08 54.09	···	15.235	14.593	15.171	15.418	14.745	0.225	1966	6533	-3.22	1.45
HE_2222-4156	22 25 28.65	-41 40 57.72	···	15.332	14.583	15.252	15.538	14.783	0.042	2773	5537	-2.73	0.42
HE_2325-0755	23 27 59.61	-07 39 13.49	14.481	13.940	13.251	14.200	14.452	13.776	0.044	1600	5665	-2.85	0.21

Table 2.1: Parameters for the stars analyzed in this study.

Parameter	BaSTI	Padova
Age	1 – 15 Gyr with step 0.1 Gyr	1 – 20 Gyr with step 0.1 Gyr
[Fe/H]	-1.05, -1.2, -1.3, -1.4, -1.55 -1.7, -1.9, -2.2, -2.5, -3.2	-1.0 – -2.2 dex, step 0.1 dex
Heavy element mixture	$[\alpha/\mathrm{Fe}] = +0.4$	$= [\alpha/\mathrm{Fe}]=+0.0$
Photometric system	UBVIJHK, Gaia DR3	UBVIJHK, Gaia DR3

Table 2.2: Characteristics of the BaSTI and Padova isochrones we used in this study.

2.3 Isochrones

To derive age we used two different sets of isochrones for old metal-poor populations: Padova isochrones[3] and a Bag of Stellar Tracks and Isochrones[4] (BaSTI).

We used these two sources of isochrones to check for systematics due to differences in stellar evolution models. For example, Padova isochrones do not take into account α-enhancement while most of the studied stars are α-enhanced. BaSTI isochrones instead have main sequence bluer than references globular clusters (Hidalgo et al. (2018)) in a very-low-mass regime. We can notice that for lower metallicity ($\left[\frac{Fe}{H}\right] = -2.2$) the two sets of isochrones are in a good agreement in the turn-off point region, but BaSTI isochrones have slightly bluer in the main sequences and red giant branch is more vertical. Instead, for higher metallicity ($\left[\frac{Fe}{H}\right] = -1.2$) the shift between isochrones is more evident. BaSTI isochrones are fainter and redder. The reason for this shift could be that they take into account α-enhancement that displaces isochrones towards higher metallicity (Salaris et al. (1993)). Tab.2.2 gives a summary of the isochrones we usde in this study.

In order to use Padova isochrones properly, we need to correct them for α-enhancement. To do so we used the technique proposed by Salaris et al. (1993) where α-enhanced isochrones can be reproduced by standard isochrones if a metallicity given by the following equation is used:

$$Z = Z_0(0.638 f_\alpha + 0.362) \tag{2.1}$$

where $f_\alpha = \frac{Z}{Z_{Sun}} = 10^{\left[\frac{\text{element abundance}}{Fe}\right]}$

The result of α-correction is shown in Fig.2.2. In this plot we can see that the correction for α-enhancement increases the total metallicity on average by 0.2 dex. Moreover, Fig.2.6 indicates a good agreement between the stars' distribution and the isochrones, both color-coded with metallicity.

2.4 Reddening

In this work we used two photometric systems: Gaia (G, G_{BP}, G_{RP}) and Johnson (B, V). Both of them cover the optical part of the spectrum thus they are quite sensitive to reddening. Therefore, correction for reddening is a critical step in our analysis. Our targets are located in the Galactic Halo ($|b| > 20^o$). Galactic Halo is poor in gas and dust and, as a consequence, it does not exhibit significant extinction. But even small reddening corrections might cause big uncertainties in age determination, that is why we used the

[3] http://stev.oapd.inaf.it/cmd
[4] http://basti-iac.oa-abruzzo.inaf.it/isocs.html

Source	Year	Type	Coverage	Accuracy
Schlegel et al.	1998	2D	all sky	16%
Schlafly &Finkbeiner	2011	2D	all sky	50 mmag
Queiroz et al.	2019	3D	$\lvert Z_{Gal}\rvert < 1$ kpc, $R_{Gal} \lesssim 20$ kpc	50-200 mmag
Green et al.	2018	3D	$\delta \gtrsim -30^o$, $d^* \lesssim 60$ kpc	10-100 mmag
Lallement et al.	2018	3D	$D^{**} \leq 4000$ pc, $\lvert Z_{Gal}\rvert \leq 600$ pc	10-150 mmag
Montalto et al.	2021	method	$d \lesssim 2.5$ kpc	

Table 2.3: Extinction sources

* Distance from the Sun.

** Distance from the Sun in the Galactic disk.

5 different sources of extinction values listed in Tab.2.3 to get the best estimate for that effect.

Schlegel et al. (1998) is a full-sky 100 μm 2D map that is a reprocessed composite of the COBE/DIRBE and IRAS/ISSA maps, where the zodiacal foreground and confirmed point sources are removed. The uncertainty of the map is around 16%.

Schlafly &Finkbeiner (2011) presented a full-sky 2D dust reddening map measured as the difference between the measured and predicted colors of a star, as derived from stellar parameters from the Sloan Extension for Galactic Understanding and Exploration Stellar Parameter Pipeline. They achieve uncertainties of 56, 34, 25, and 29 mmag in the colors u - g, g - r, r - i, and i - z, per star, though the uncertainty varies depending on the stellar type and the magnitude of the star.

`StarHorse` extinction values are computed by Bayesian isochrone fitting technique with stellar parameters (T_{eff}, log g, $\left[\frac{M}{H}\right]$) from spectroscopy, photometric magnitude (m_λ), parallax from Gaia DR2, and PARSEC isochrones. The extinction uncertainties are ∼70 mmag, when all photometric information is available, and ∼170 mmag if optical photometry is missing. For our data set the most common value of uncertainty is ∼200 mmag. (See also Sec. 2.5.4) They provide an coverage of the disc close to the Galactic mid-plane ($|Z_{Gal}| < 1kpc$) from the Galactic center out to $R_{Gal} \sim 20kpc$.

Green et al. (2018) produced a new 3D map of interstellar dust reddening, covering three-quarters of the sky (declinations of $\delta \gtrsim -30$) out to a distance of several kiloparsecs. The map is based on high-quality stellar photometry of 800 million stars from Pan-STARRS 1 and 2MASS. They divide the sky into sightlines containing a few hundred stars each, and then infer stellar distances and types, along with the line-of-sight dust distribution. For our data set the mean uncertainty of this map is about 20 mmag.

Lallement et al. (2018) selected low-reddening SDSS/APOGEE-DR14 red giants to obtain an empirical effective temperature- and metallicity-dependent photometric calibration in the Gaia G and 2MASS Ks bands. This calibration has been combined with Gaia G-band empirical extinction coefficients recently published, G, J, and Ks photometry, and APOGEE atmospheric parameters to derive the extinction of a large fraction of the survey targets. Distances were estimated independently using isochrones and the magnitude-independent extinction K_{J-Ks}. This new data set has been merged with the one used for the earlier version of the dust map. A new Bayesian inversion of distance-extinction pairs has been performed to produce an updated 3D map that covers $4000 \times 4000 \times 600$ pc^3 around the Sun. Uncertainty of this map for our data set varies from 10 to 150 mmag.

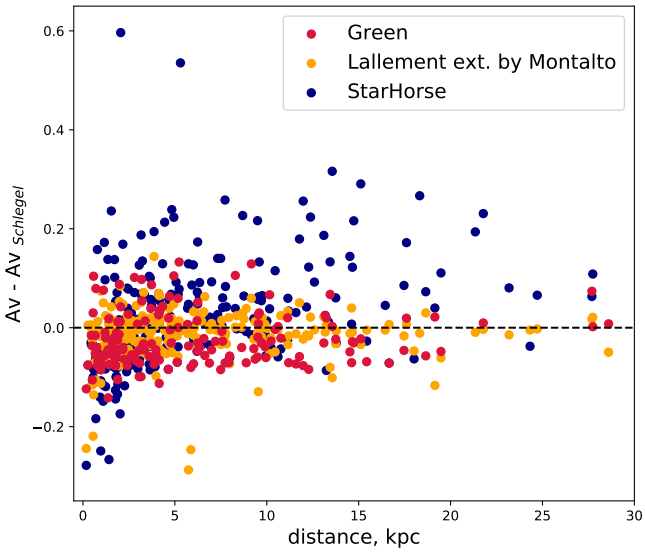

Figure 2.3: Comparison of reddening from Green et al. (2018), Lallement et al. (2018) extended by Montalto et al. (2021) and `StarHorse` with reddening from Schlegel et al. (1998) as a function of distance.

To extent Lallement et al. (2018) map to farther distances we applied the method illustrated in Montalto et al. (2021). They suggested to use the dust distribution model of the Milky Way to calculate the amount of dust between the edge of the Lallement et al. (2018) map and the real position of the object. It can be applied if there is no specific dust and gas structures which is almost true for the Halo where all stars under consideration are located. In Montalto et al. (2021) the extension method was applied for stars not farther than 2.5 kpc and tested to show good agreement with the photometric parameters.

To get the best extinction estimate for our stars we studied all sources of reddening corrections listed in Tab.2.3. Since the range in distances for our stars is from 0.2 to 30 kpc (see Sec. 4.2.2) it is more precise to use a 3D map instead of 2D, which additionally has lower accuracy. In Fig.2.3 we can see that Lallement et al. (2018) extended by Montalto et al. (2021) and Green et al. (2018) are in a good agreement with each other and with Schlegel et al. (1998) 2D map for far distances, for closer to the Sun star Schlegel et al. (1998) map reddening is greater. `StarHorse` reddening instead shows a larger dispersion in all distance range and on average larger reddening values compared to Schlegel et al. (1998) map. Therefore by comparing the three latest 3D maps we made a choice to use only Lallement et al. (2018) extended by Montalto et al. (2021) and Green et al. (2018). Both these maps have weak points. For example, Green et al. (2018) map covers only three-quarters of the sky. Lallement et al. (2018) does not have high accuracy in all directions. That is why our solution was to combine two reddening maps together by choosing for each star the best extinction estimate from Lallement et al. (2018) extended by Montalto et al. (2021) 3D map or from Green et al. (2018) 3D map. The resulting reddening correction is shown in Fig.2.4. We can see that the combined map shows the smallest stars' dispersion in the color-magnitude diagram (CMD).

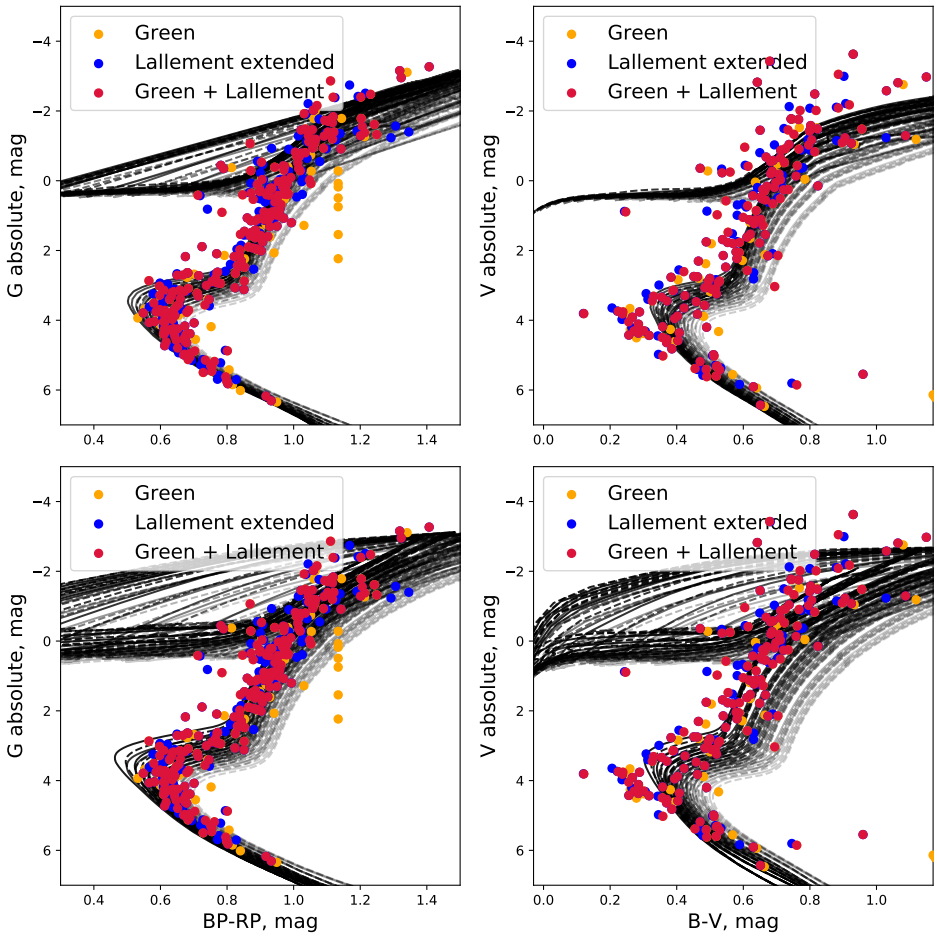

Figure 2.4: CMD in Gaia (*1st column*) and Johnson (*2nd column*) photometry corrected using Lallement et al. (2018) extended by Montalto et al. (2021), Green et al. (2018) and the best correction value from one of the two (Green+Lallement). *1st row*: Padova isochrones ([Fe/H]: -1.0 – -2.2 dex, age: 10 – 15 Gyr). *2nd row*: BaSTI isochrones ([Fe/H]: -1.0 – -3.2 dex, age: 10 – 15 Gyr).

Data product	Typical uncertainty			
	G < 15	G = 17	G = 20	G = 21
Five-parameter astrometry				
position, mas	0.01 - 0.02	0.05	0.4	1
parallax, mas	0.02 - 0.03	0.07	0.5	1.3
Six-parameter astrometry				
position, mas	0.02 - 0.03	0.08	0.4	1
parallax, mas	0.02 - 0.04	0.1	0.5	1.4

Table 2.4: Uncertainties of Gaia Data Release 3 astrometry from Gaia Collaboration (2021)

2.5 Distance determination

Stellar distances constitute a fundamental quantity in astrophysics. In fact we need distances to compute absolute magnitudes for each metal-poor star in our data set. Distance is one of the crucial parameters that affect the obtained results. For this purpose we used four different techniques: Gaia DR3 parallaxes (Gaia Collaboration et al. (2022a)), Gaia EDR3 (Gaia Collaboration (2021)) corrected by Lindegren et al. (2021), the distances derived by Bailer-Jones et al. (2021), and Queiroz et al. (2019) (`StarHorse`).

2.5.1 Gaia Data Release 3 (Gaia DR3) parallaxes

The first main technique is parallax distance. Today we have very accurate trigonometric parallaxes (see for uncertainties Tab.4.2) obtained by the Gaia satellite for about 1,47 billion stars (Gaia Collaboration et al. (2022a)). From these trigonometric parallaxes, distance can be obtained through the following equation:

$$d = \frac{1}{\pi} \tag{2.2}$$

where d is the distance to the object in pc and π is its trigonometric parallax in arcsecs. The problem with this distance determination is that, due to the structure of this equation, uncertainties on the distance are not symmetric around the mean value, especially for a large uncertainty on the parallax. That is why errors for each source must be computed separately for the higher and lower edges of the distance:

$$d_{low} = \frac{1}{\pi + \Delta\pi} \tag{2.3}$$

$$d_{high} = \frac{1}{\pi - \Delta\pi} \tag{2.4}$$

Uncertainties of Gaia Data Release 3 astrometry as given by the GAIA Collaboration are shown in Tab.4.2

2.5.2 Corrections for Gaia EDR3 parallaxes: Lindegren et al. (2021)

Parallaxes measured by Gaia Collaboration (2021) can have some biases that have been measured by Lindegren et al. (2021). Lindegren et al. (2021) found that parallaxes that

correspond to quasars (distant objects, whose parallaxes should be distributed around zero) have a systematical offset from the expected distribution around zero, by a few tens of micro-arcsec. Based on quasars bias for faint sources they extended the map of the correction to lower magnitudes using physical pairs (binaries) and Large Magellanic Cloud sources. The parallax bias is found to depend in a non-trivial way on (at least) the magnitude, color, and ecliptic latitude of the source. Different dependencies apply to the five- and six-parameter solutions in Gaia EDR3. While it is not possible to derive a definitive recipe for the parallax correction, they give tentative expressions to be used at the researcher's discretion and point out some possible paths toward future improvements. We applied the Lindegren et al. (2021) correction for downloaded Gaia EDR3 parallaxes and then computed distance and its lower and upper limit through Eq.(2.2), (2.4), (2.3). The results are shown in Fig.2.6 second row.

2.5.3 Corrections for Gaia EDR3 parallaxes: Bailer-Jones et al. (2021)

Despite Gaia EDR3's high precision, the majority of stars observed by Gaia are distant or faint so their parallax uncertainties are large and this prevents the direct inversion of parallax for obtaining distance. That is why Bailer-Jones et al. (2021) used a probabilistic approach to estimate stellar distances that use a prior construction from a three-dimensional model of our Galaxy. This model includes interstellar extinction and Gaia's variable magnitude limit. They obtain two types of distances. The first, geometric, uses the parallax together with a direction-dependent prior on distance. The second, photo-geometric, additionally uses the color and apparent magnitude of a star, by exploiting the fact that stars of a given color have a restricted range of probable absolute magnitudes (plus extinction). Tests on simulated data and external validations show that the photo-geometric estimates generally have higher accuracy and precision for stars with poor parallaxes.

2.5.4 `StarHorse` distances

An additional source of distances is the APOGEE DR16 `StarHorse` catalog where Queiroz et al. (2019) combined spectroscopic (APOGEE-2 survey Data Release 16) and photometric (IR: 2MASS, AllWISE; Optical: PanSTARRS-1) data as well as parallaxes (Gaia Data Release 2). They used Bayesian isochrone-fitting code `StarHorse` to obtain distances and extinction for 388 815 APOGEE stars. All studied in this work stars are included. The typical distance uncertainties are $\sim$ 6% for APOGEE giants and $\sim$ 2% for APOGEE dwarfs. `StarHorse` uncertainties vary with the input spectroscopic catalogue, available photometry, and parallax uncertainties. Data are available at https://data.aip.de/projects/aqueiroz2020.html.

2.5.5 Distance choice

The comparison of distances from Bailer-Jones et al. (2021) and parallaxes from Gaia DR3 and corrected by Lindegren et al. (2021) are shown in Fig.2.5 (left, middle panels). The vertical axis shows the Gaia DR3 parallax and corrected parallax multiplied by the

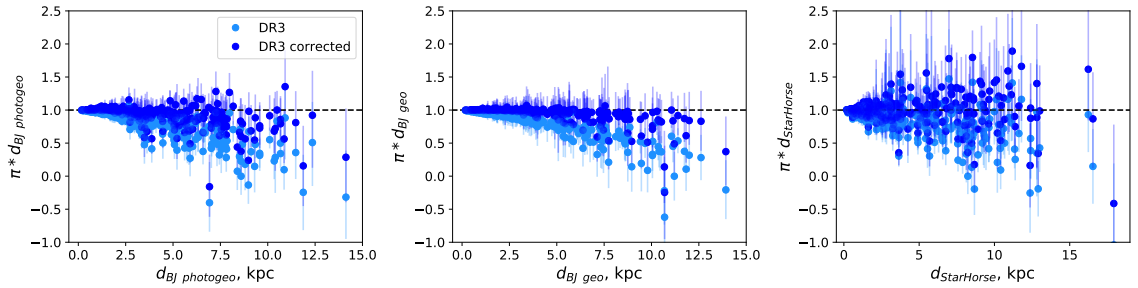

Figure 2.5: Comparison of parallax from Gaia DR3 (light blue) and corrected Gaia EDR3 by Lindegren et al. (2021) (blue) with geometric (*left*) and photogeometric (*middle*) distance from Bailer-Jones et al. (2021) and with `StarHorse` distance from Queiroz et al. (2019) (*right*). The vertical axis shows the Gaia DR3 parallax and corrected parallax multiplied by the geometric distance: values under 1 correspond to the parallax distance being larger than the value of Bailer-Jones et al. (2021)/`StarHorse` distance and vice versa. The vertical error bars take into account the statistical uncertainties both on the parallax and the distance, but the horizontal error bars for the distance are not displayed.

geometric (Fig.2.5, left panel) and photo-geometric (Fig.2.5, middle panel) distance: values under 1 correspond to the parallax distance larger than the value of Bailer-Jones et al. (2021) distance and vice versa. The vertical error bars take into account the statistical uncertainties both on the parallax and on the distance, but the horizontal error bars for the distance are not displayed. We can see that for close objects (< 3 kpc) parallaxes corrected by Lindegren et al. (2021) are in good agreement with Bailer-Jones et al. (2021) geometric and photo-geometric distances. Beyond 3 kpc the corrected parallaxes give larger distances than the geometric and the photo-geometric ones. In general Gaia DR3 parallaxes yield larger distances in all ranges of distances. Some of the stars have negative parallaxes but positive distances can be derived from Bailer-Jones et al. (2021).

From Fig.2.5 (right panel) we can notice that `StarHorse` distances and distances from parallax corrected by Lindegren et al. (2021) are in a good agreement. On the contrary, direct distances from Gaia EDR3 parallaxes show larger values. However, to consider the best estimate of distances for our data set a deeper investigations should be done using a CMD and isochrone fitting technique. In Fig.2.6 stars are corrected for reddening with combined Green et al. (2018) + Lallement et al. (2018) extended by Montalto et al. (2021) map and color-coded with corrected metallicity for Padova isochrones, observed - for BaSTI isochrones. Metallicity range for Padova isochrones: -1.3 – -2.2 dex, for BaSTI isochrones: -1.3 – -3.2 dex. For each metallicity 10 and 15 Gyr isochrone are plotted color-coded with metallicity. Comparing different methods for distance determination we can highlight the following discrepancies, depending on the distance technique we use:

- Some stars are located in low probability regions, like above the MS and below the SGB, or on the red sie of the RGB. (Gaia DR3 parallaxes, Lindegren, Bailer-Jones, `StarHorse`)
- Non negligible shift in the position of RGB and TO stars in comparison with the isochrones of the same metallicity. (Lindegren, Bailer-Jones, `StarHorse`)
- Different shape of the targets RGB if compared with the shape of isochrone RGB. (Lindegren, Bailer-Jones, `StarHorse`)

	B	V	I	G	G_{BP}	G_{RP}
A_λ/A_V	1.326	1.000	0.599	0.861	1.061	0.648

Table 2.5: Reddening coefficients for different photometric filters (http://stev.oapd.inaf.it/cgi-bin/cmd_3.4)

According to the listed above criteria, we can conclude that Gaia parallaxes show the best fit to the data. In this case we can see also that fewer targets only are lying in the low probability region. Moreover, all stars with metallicities lower than the lower limit for isochrones metallicity range lie above RGB where the estimated position of these stars should be. Lindegren correction and `StarHorse` distances move low metallicity stars in RGB to the position of isochrones with higher metallicity and break the shape of RGB. Bailer-Jones additionally shift more stars to the low probability region which reduces the quality of the data set. All these tests show that the best distance estimate estimator for our purposes is the distance obtained directly inverting Gaia parallaxes.

A possible explanation for the lower accuracy we obtained applying Lindegren et al. (2021) correction is that they are based on faint sources and, as a consequence, they are less accurate for brighter magnitudes as it is the case for our targets. Bailer-Jones also used Lindegren correction as an input. Because of this, their corrections are affected by the same bias. `StarHorse` distances are less precise instead because Queiroz et al. (2019) used Gaia Data Release 2 parallaxes as prior for the distance calculation, which have lower accuracy compared with new Gaia DR3 parallaxes.

2.6 Derivation of the absolute magnitude

To be able to compare isochrones with observational data we need to convert observed G photometry to its absolute magnitude. To do this we need to apply distance modulus and reddening correction using:

$$M_\lambda = m_\lambda + 5 - 5 \cdot log(d) - A_\lambda$$

where d is the distance to the star in parsecs and $A_G = A_V \cdot coef$ (for $coef$ see Tab.2.5). These trasformations assume the standard reddening law $A_V = R_V \cdot E(B-V)$ with $R_V = 3.1$ since all our targets are far from the galactic plane or the galactic Bulge, where R_V can assume different values.

2.7 Difference in CMDs for different photometric systems

A closer look at the data evidences additional peculiarities. Fig.2.6 shows that part of TO stars in the Johnson photometry (the two columns on the right) are blue-shifted with respect to the isochrones and also if compared with their position in the Gaia photometry (the two columns on the left). In order to investigate deeper this behaviour we performed further tests.

First of all, we color-coded our data with Galactic latitude (Fig.2.7, top row). The bottom left panel of this figure report the position of the targets on the V vs. B-V CMD.

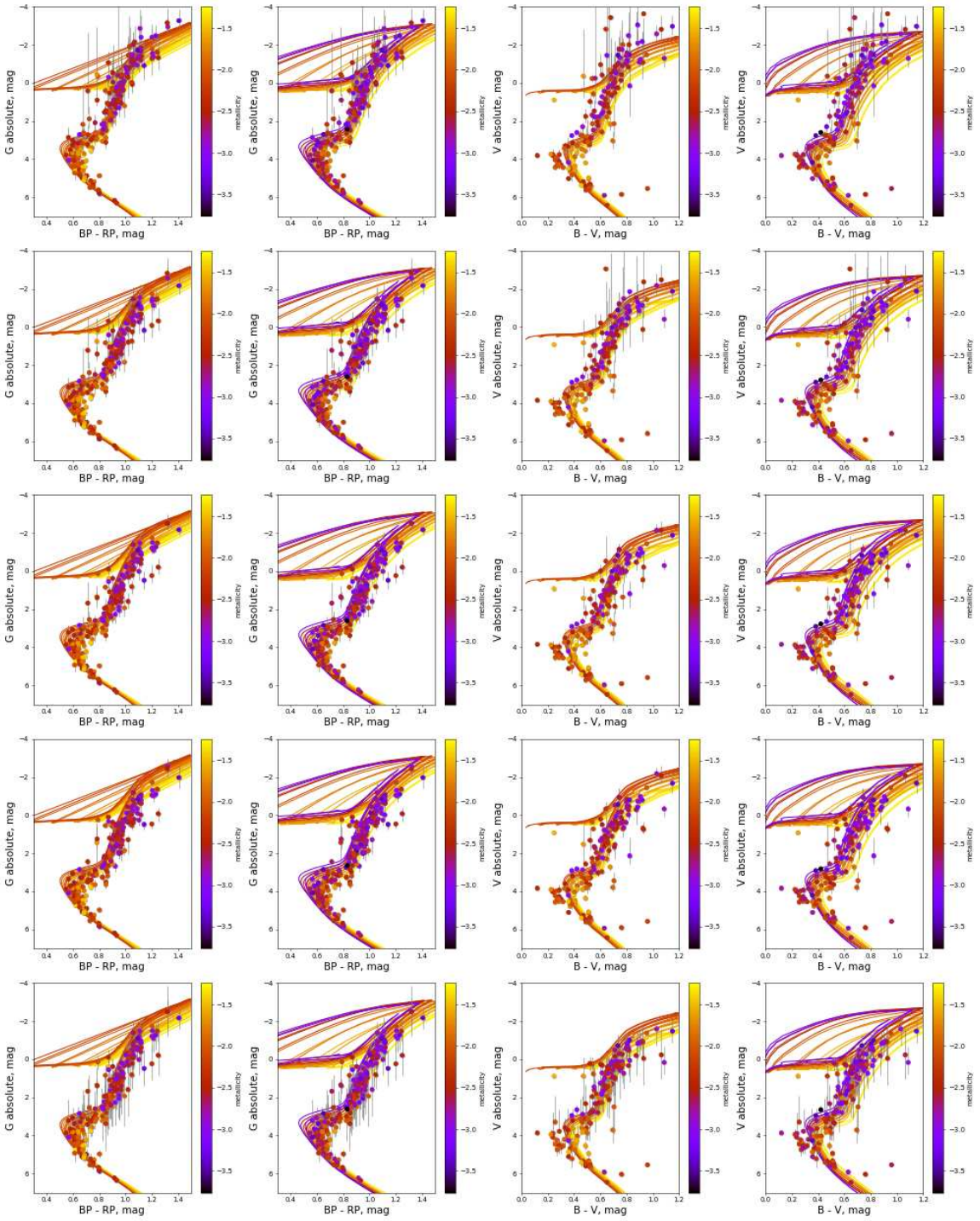

Figure 2.6: Gaia (*first two columns*) and Johnson (*last two columns*) photometry color-coded with corrected metallicity for Padova isochrones (1^{st}, 3^{rd} *columns*) and with observed metallicity for BaSTI isochrones (2^{nd}, 4^{th} *columns*). Distances are computed by Gaia DR3 parallaxes (1^{st} *row*), Gaia EDR3 parallaxes corrected by Lindegren et al. (2021) (2^{nd} *row*), Bailer-Jones et al. (2021) (geo: 3^{rd} *row*, photogeo: 4^{th} *row*), and computed by Queiroz et al. (2019) (`StarHorse`) (5^{th} *row*). Isochrones are color-coded with metallicity ([Fe/H]: -1.0 – -2.2 dex, age: 10 – 15 Gyr (Padova); [Fe/H]: -1.0 – -3.2 dex, age: 10 – 15 Gyr (BaSTI))

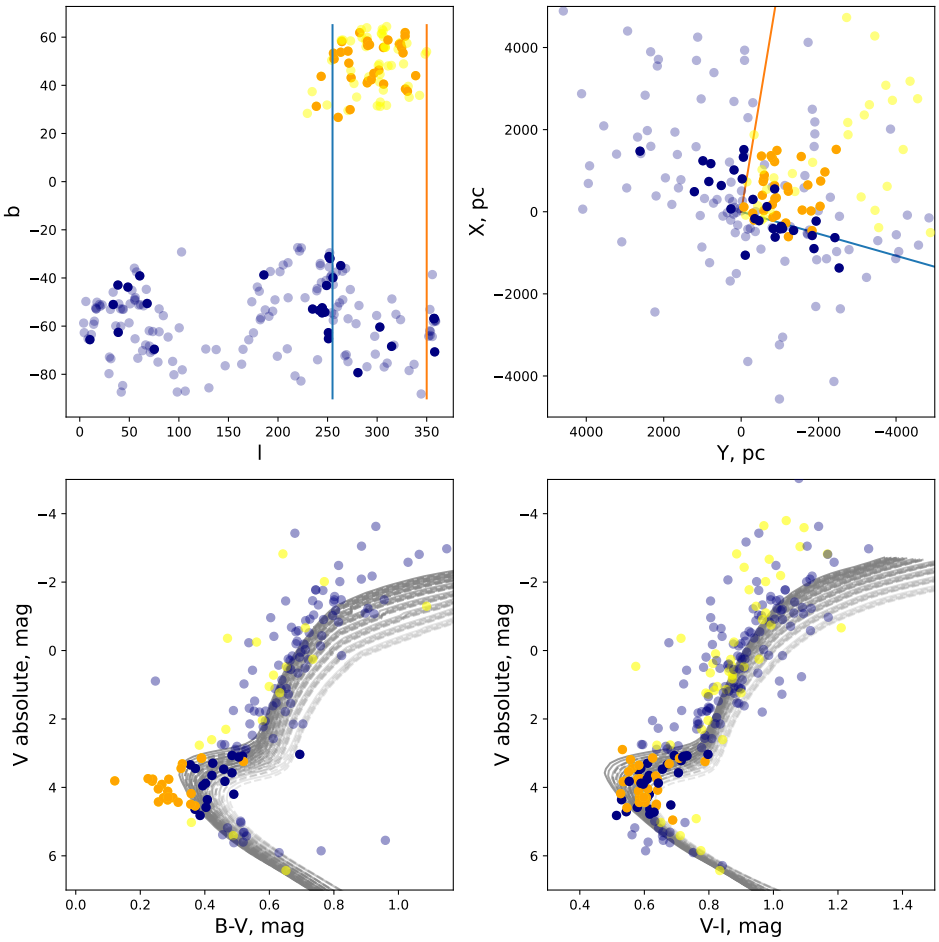

Figure 2.7: *Top*: Position of our targets on the sky (*left*, Galactic coordinates) and in the Galactic plane (*right*), color-coded with Galactic latitude ($b > 0$: yellow, $b < 0$: blue). *Bottom*: CMD in V vs. B-V (*left*) and V vs. V-I (*right*) filters, yellow points are non-TO stars with $b > 0$, orange points are TO stars with $b > 0$, light blue are non-TO stars with $b < 0$, while dark blue are TO stars with $b < 0$. Padova isochrones are added as a reference ([Fe/H]: -1.0 – -2.2 dex, age: 10 – 15 Gyr).

It is clear that all the stars with the larger TO-shift are located at positive Galactic latitude, while all the other stars have negative Galactic latitudes. The difference in position might indicate a difference in reddening, but since our data set is corrected for it, only a particularly improbable kind of extinction could explain this behaviour. On the other hand Fig.2.7 (bottom right panel) reports the V vs. V-I CMD, where we do not see such an affect. This means that the shift is entirely due to the B filter.

Chemical analysis

One of the reasons why stars with the same temperature (as inferred from the BP-GP and V-I colors) and luminosity (as inferred from G and V magnitudes) differ in just one of the filters, is that this filter contains strong molecular bands and that the elements responsible for these band (usually C,N,O) vary their abundances from one star the other. Also chemical abundances variation of C, N, O, Ne, Mg, Si, S, Ca, Fe affect opacity of the star and change the continuum emission in that part of the spectrum (Salaris et al.

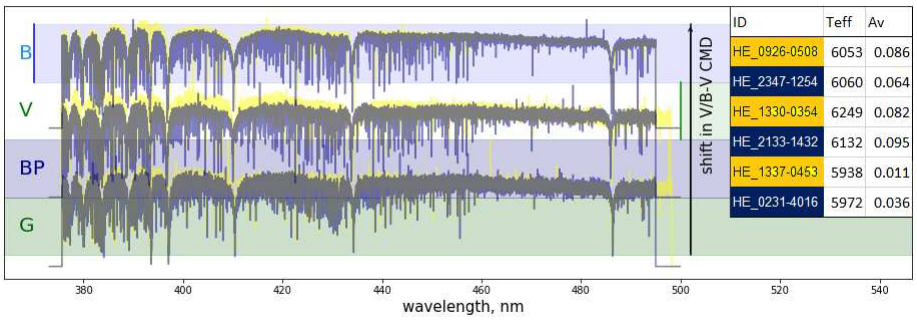

Figure 2.8: Comparison of the spectra for bluer and redder stars in V/B_V CMD. Gaia and Johnson photometric filters ranges are plotted with color.

(1993)). To check these effects we download from the ESO database[5] flux-calibrated UVES spectra for couples of stars with the same T_{eff} and similar reddening ($\Delta A_V < 0.02$ mag) but different dereddened B-V colors. In Fig.2.8 we can see that when the distance between shifted (yellow) and non-shifted (blue) stars increases, also the continuum of the shifted stars increases. It happens specifically in the range of the B filter. To check the dependence between the shift and chemical composition, we color-coded CMDs with abundances of C (the only element responsible of molecular bands we have) and Fe. From Fig.2.9 we can see that shifted stars are enhanced in C and more metal-poor on average. Since we see no presence of strong molecular bands in the spectra, we conclude it is the change in the opacity of the atmospheres of the stars due to the different C and Fe contents that is the cause of shift in the B-V color. Specifically higher [C/Fe] abundance and lower [Fe/H] content increase the flux in the B filter.

For this reason Johnson photometry can not be properly used for age determination for very metal-poor stars. Gaia filters are wider and so less affected by this phenomenon and it is the only photometry we will use for the age determination.

2.8 Age determination method

To derive age we developed an automatic technique based on isochrone fitting. First, we filtered our data with the following criteria:

1. Distance > 0
2. Distance error $< 20\%$
3. Metallicity range: -2.3 — -1 dex for Padova isochrone; -3.3 – -1 dex for BaSTI isochrone
4. Absolute magnitude is in TO-point region: $2.4 < G < 4.7$ mag

The first two criteria exclude stars with bad astrometric measurements. The third cutoff is based on the metallicity range covered by isochrone data sets. We should note that for different isochrones the cutoff is different. And the fourth cutoff leaves only stars

[5] http://archive.eso.orGvs.scienceportal/home

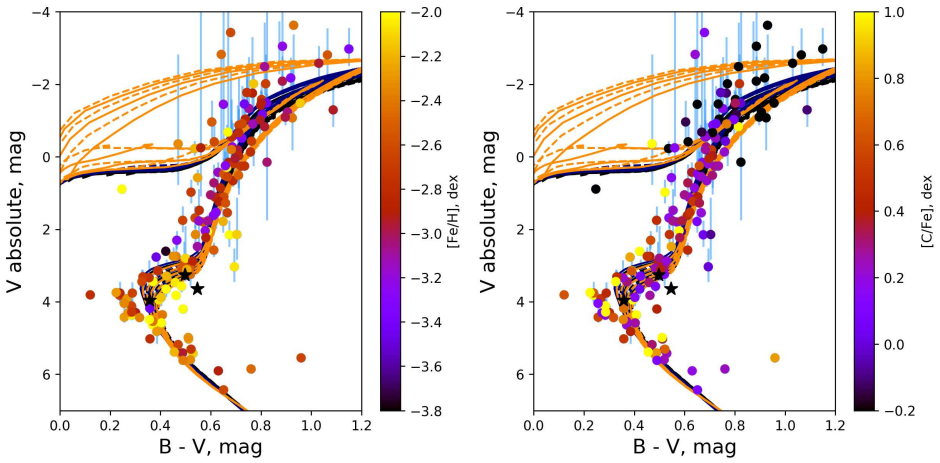

Figure 2.9: Johnson photometry color-coded with [Fe/H] (*left panel*) and [C/Fe] (*right panel*). Distance computed by means of Gaia DR3 parallaxes. Black stars are stars: HD 84937, HD 132475, and HD 140283 (VandenBerg et al. (2014)). Padova (blue) and BaSTI (orange) isochrones with [Fe/H] = -2.2 dex, age: 10 – 15 Gyr are added as a reference.

from the TO-point region - the part of the CMD most sensitive to age. The algorithm takes a set of isochrones matching the metallicity of the target and searches for the closest. Each isochrone is define by a set of X,Y points in the 2D space of the CMD. The distance used to choose the closest isochrone is the shortest between the perpendicular to one of the segments defines by two consecutive X,Y points, and the distance to the closest point of the isochrone. The age of the closest isochrone is then considered as a fisrt guess of age of the star if the distance is less than 10^{-4} mag (the maximum distance between isochrones with age step 100 Myr). Otherwise, age can not be derived, since the star is too far from all isochrones.

As a second step, we consider the mean parallax, reddening, metallicity, and photometry of each target and the related errors. Assuming a gaussian distribution we randomly distributed 10.000 points in the parameter space and applied the age determination technique to each of them. The result is an age histogram that is fitted with a Gaussian function. We consider its mean as the age of the star and σ as its uncertainty.

In Fig.2.10 we can see an illustration of the age determination for Padova and BaSTI isochrones. Isochrones have an upper limit of 20 Gyr for Padova, and from 15.4 to 19.2 Gyr (depending on metallicities) for BaSTI. Because of this, all stars redder than the oldest isochrone are considered to have the age of this isochrone. Therefore, we get some saturation in the bin corresponding to the oldest isochrone. We cut saturated bins as not representative. We derived age in three different combinations of photometric filters: G vs. G_{BP}-G_{RP}, G vs. G_{BP}-G, G vs. G-G_{RP}.

To get the best age sample we applied the following criteria:

1. Age derived in all three filter combinations: G vs. G_{BP}-G_{RP}, G vs. G_{BP}-G, G vs. G-G_{RP}.

2. Derived age is not closer to the oldest isochrone less than 1σ.

In this way we reduced the targets for which we can derive good ages to 28.

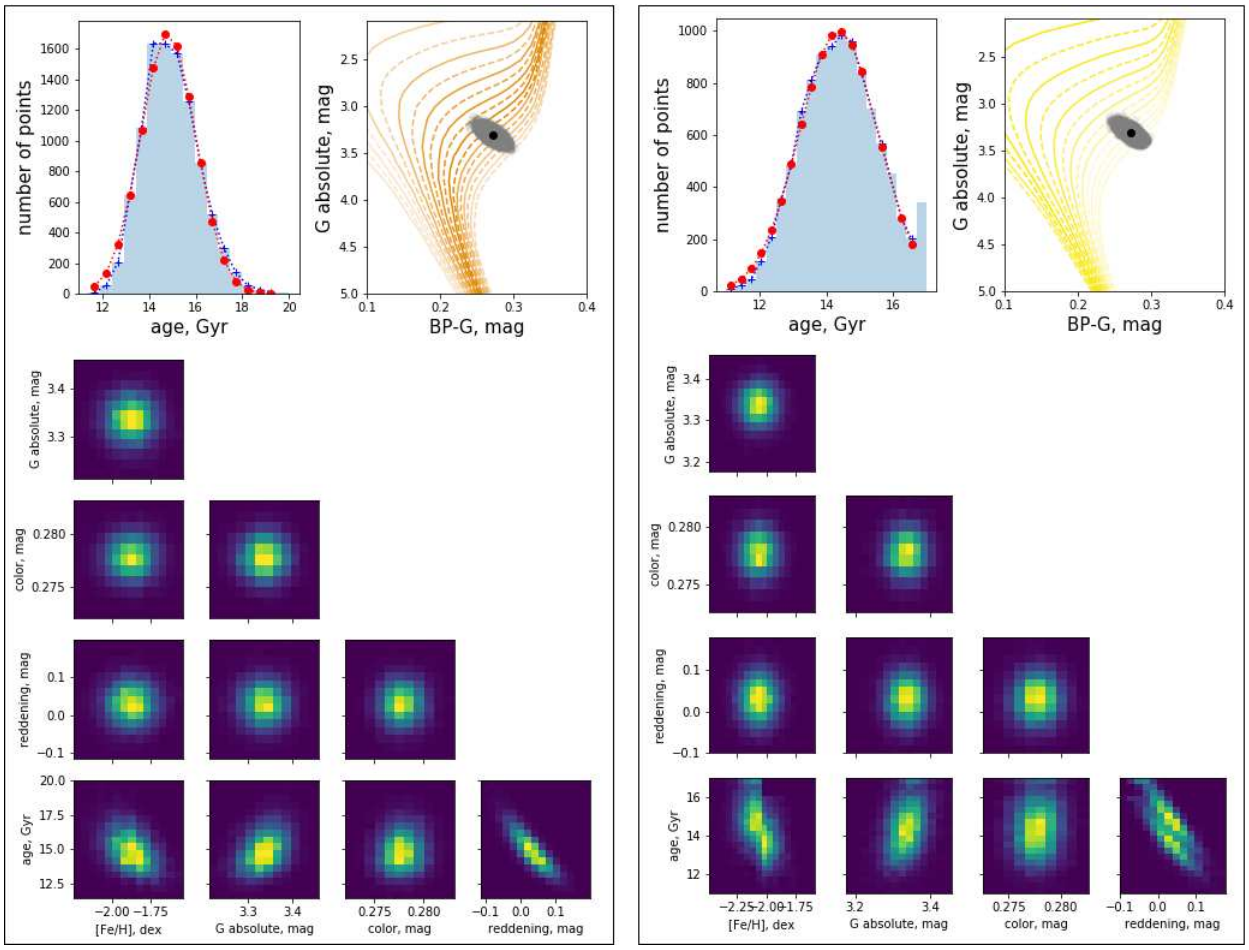

Figure 2.10: Resulting plot of age determination from Padova (*left panel*) and BaSTI (*right panel*) isochrones for star HE 0023−4825 in diagrams G vs. BP-G. Grey dotes in the CMD are randomly selected input parameters. Black dote is original stellar parameters.

ID	$\left[\frac{Fe}{H}\right]$	age from Padova isochrones, Gyr						age from BaSTI isochrones, Gyr						average, Gyr		
		G vs. BP*-G		G vs. G-RP*		G vs. BP-RP		G vs. BP-G		G vs. G-RP		G vs. BP-RP		P**	B***	P+B
	dex	age	error	age	error	age	error	age	error	age	error	age	error	age	age	age
HE 0023-4825	-2.06	14.8	±1.2	14.9	±1.1	14.9	±1.1	14.4	±1.2	14.4	±1.2	14.4	±1.2	14.9	14.4	14.6
HE 0109-3711	-1.91	11.8	±2.3	11.9	±2.4	11.8	±2.3	11.6	±2.7	11.8	±2.7	11.7	±2.7	11.8	11.7	11.8
HE 0231-4016	-2.08	13.3	±1.3	13.3	±1.2	13.3	±1.3	15.4	±1.3	15.4	±1.2	15.4	±1.2	13.3	15.4	14.4
HE 0340-3430	-1.95	13.6	±0.9	13.6	±0.9	13.6	±0.9	12.9	±0.9	13.1	±0.9	13.1	±0.9	13.6	13.0	13.3
HE 0430-4404	-2.07	7.7	±3.0	6.6	±2.7	7.0	±2.8	13.8	±2.8	12.7	±2.5	13.2	±2.6	7.1	13.2	10.1
HE 0447-4858	-1.69	14.0	±2.1	13.4	±1.7	13.6	±1.9	13.1	±2.1	12.7	±1.9	12.9	±2.0	13.7	12.9	13.3
HE 0501-5139	-2.38	9.0	±2.3	9.0	±2.3	9.0	±2.3	8.9	±2.4	8.9	±2.4	8.9	±2.4	9.0	8.9	8.9
HE 0519-5525	-2.52	13.3	±1.8	13.6	±1.8	13.5	±1.8	13.3	±1.6	13.6	±1.6	13.5	±1.6	13.5	13.4	13.5
HE 0534-4615	-2.01	16.0	±2.9	16.0	±2.9	16.0	±2.9	13.8	±2.3	13.8	±2.2	13.9	±2.2	16.0	13.8	14.9
HE 0938+0114	-2.51	12.4	±1.9	13.8	±1.8	13.2	±1.8	13.8	±1.7	14.6	±1.0	14.3	±1.2	13.1	14.2	13.7
HE 1052-2548	-2.29	15.3	±0.7	16.1	±0.6	15.8	±0.6	15.2	±0.5	16.0	±0.4	15.7	±0.4	15.7	15.7	15.7
HE 1105+0027	-2.42	11.2	±2.1	11.4	±2.2	11.3	±2.1	12.8	±2.4	12.9	±2.4	12.8	±2.4	11.3	12.8	12.1
HE 1225-0515	-1.96	14.6	±1.6	14.6	±1.6	14.6	±1.6	14.7	±1.8	14.6	±1.6	14.7	±1.8	14.6	14.7	14.6
HE 1330-0354	-2.29	12.3	±0.9	13.3	±0.8	12.9	±0.8	13.7	±0.9	14.6	±0.8	14.2	±0.8	12.8	14.2	13.5
HE 2250-2132	-2.22	13.2	±1.2	13.6	±1.3	13.4	±1.3	12.8	±1.1	13.2	±1.3	13.0	±1.2	13.4	13.0	13.2
HE 2347-1254	-1.83	14.6	±1.7	14.6	±1.5	14.6	±1.6	14.5	±1.6	14.6	±1.4	14.4	±1.4	14.6	14.5	14.6
HE 2347-1448	-2.31	8.7	±1.8	8.8	±1.8	8.8	±1.8	8.4	±1.8	8.5	±1.9	8.5	±1.9	8.8	8.5	8.6
HE 0244-4111	-2.56	···	···	···	···	···	···	12.6	±1.3	13.0	±1.3	12.7	±1.3	···	12.8	···
HE 0441-4343	-2.52	···	···	···	···	···	···	10.3	±1.9	10.5	±1.9	10.4	±1.9	···	10.4	···
HE 0513-4557	-2.79	···	···	···	···	···	···	12.5	±2.5	12.4	±2.5	12.4	±2.5	···	12.4	···
HE 0926-0508	-2.78	···	···	···	···	···	···	14.6	±0.8	14.9	±0.6	14.8	±0.7	···	14.8	···
HE 1006-2218	-2.69	···	···	···	···	···	···	12.7	±1.1	13.1	±0.8	12.9	±0.9	···	12.9	···
HE 1015-0027	-2.66	···	···	···	···	···	···	14.9	±1.3	15.6	±1.0	15.1	±1.0	···	15.2	···
HE 1120-0153	-2.77	···	···	···	···	···	···	10.7	±0.7	11.0	±0.6	10.8	±0.6	···	10.8	···
HE 1126-1735	-2.69	···	···	···	···	···	···	9.4	±2.6	9.5	±2.6	9.4	±2.6	···	9.4	···
HE 1413-1954	-3.22	···	···	···	···	···	···	13.1	±0.9	15.3	±1.5	14.2	±1.2	···	14.2	···
HE 2222-4156	-2.73	···	···	···	···	···	···	13.3	±2.4	13.7	±2.4	13.5	±2.4	···	13.5	···
HE 2325-0755	-2.85	···	···	···	···	···	···	13.3	±1.2	13.6	±1.2	13.6	±1.2	···	13.5	···

*BP - G_{BP}, RP - G_{RP}, **P - Padova, ***B - BaSTI

Table 2.6: Age of very metal-poor stars.

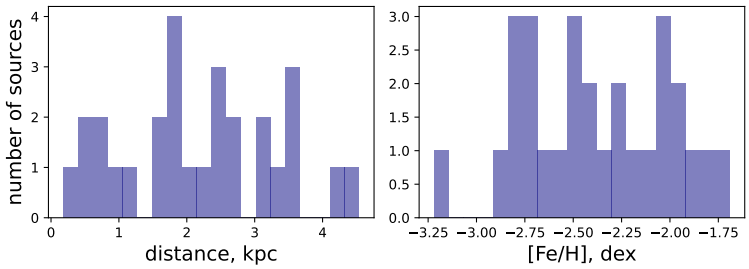

Figure 2.11: Distribution of the distance and metallicity for the 28 stars with derived age.

2.9 Results

2.9.1 Age

The derived ages for 28 selected stars are reported in Tab.2.6. The distribution of the distance nd metallicity is reported in the Fig.2.11 Out of 28 we have only 17 stars for which age is derived from both isochrone sets and for 11 stars age was derived only from BaSTI isochrone set due to its lower limit in metallicity. In Fig.2.12 on the left we can see the dispersion of the age, where the vertical dotted line show the age of the Universe 13.77 Gyr (Bennett et al. (2013)). On the right of Fig.2.12 shows that on average Padova isochrones show older age but the systematic difference is much less than 1 Gyr.

We also compared ages derived with different filter combinations: G vs. G_{BP}-G, G vs. G-G_{RP}, G vs. G_{BP}-G_{RP}. The result is reported in Fig.2.13 where we can notice that the peak of all distributions is compatible with zero within the errors. This mean that ages derived with different filter combinations are the same.

2.9.2 Comparison with old metal-poor globular clusters: M30, M92, and NGC 6397

We used metal-poor globular clusters (GCs) as a test of our age determination technique. We calculated the age for each star of GC located in the TO-point region ($2.4 < G < 4.7$ mag). All parameters for age determination of GC are listed in Tab.2.7. Parallax was derived as a mean parallax from Gaia DR3 of all members of the cluster. All three GC are located far from the Sun ($> 2.5kpc$). They lie outside the Green et al. (2018) reddening map, and far from the edge of the Lallement et al. (2018) reddening map that is why we choose extinction coefficients from 2D Schlegel et al. (1998) map. Metallicities are taken as an average of results listed in the SIMBAD catalog[6]. Reference ages were collected from Correnti et al. (2018) (NGC 6397), Kains et al. (2013) (M 30), VandenBerg et al. (2016) (M 92).

Firstly, we checked the accuracy of our automatic age determination method by comparing the age derived by different authors with our results. As we can notice in the Fig.2.14 that the age determined by our method is in a good agreement with ages derived by other authors. Only for M 30 age is slightly younger. This inconsistency is caused by uncertainties of input data, especially in parallax and reddening.

Secondly, we compare the distribution of the age of the GC with the age distribution

[6] http://simbad.u-strasbg.fr/simbad/sim-fbasic

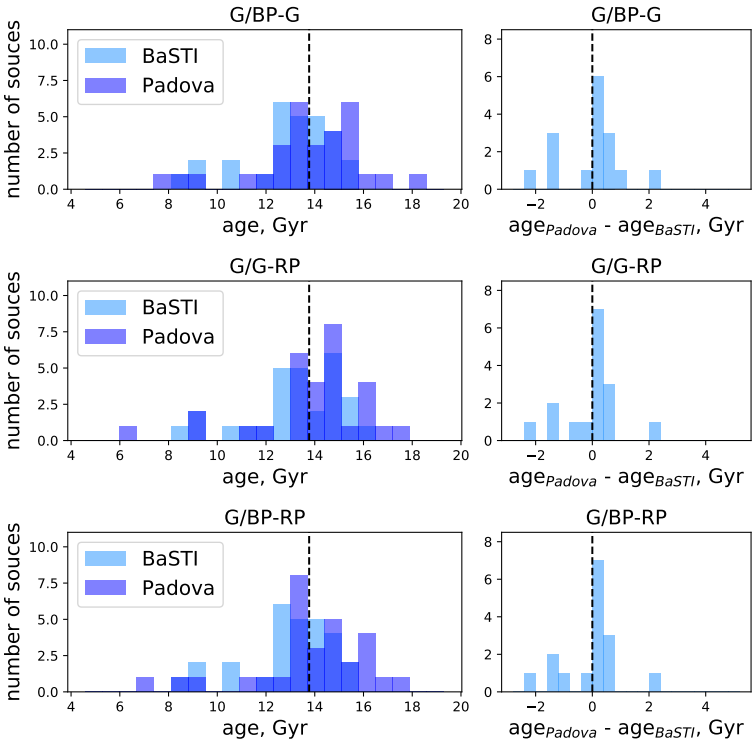

Figure 2.12: *Left*: dispersion in age determination from Padova and BaSTI isochrones in diagrams G vs. G_{BP}-G, G vs. G-G_{RP}, G vs. G_{BP}-G_{RP}. Vertical dotted line is the age of the Universe 13.77 Gyr (Bennett et al. (2013)). *Right*: dispersion in age difference between Padova and BaSTI isochrones in diagrams G vs. G_{BP}-G, G vs. G-G_{RP}, G vs. G_{BP}-G_{RP}. Vertical dotted line is a zero point.

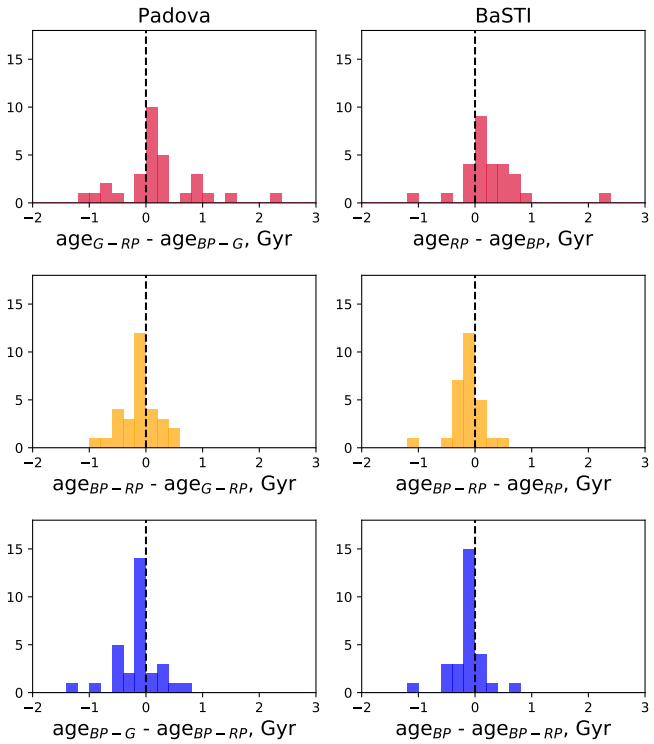

Figure 2.13: Dispersion of difference in age from different filter combinations: G vs. G_{BP}-G, G vs. G-G_{RP}, G vs. G_{BP}-G_{RP} for Padova and BaSTI isochrones. Vertical dotted line is zero-line.

Name	[Fe/H] dex	age Gyr	π mas	d pc	A_v mag	age(ref.) Gyr
NGC 6397	-1.99	12.9	0.397	2519	0.614	12.6
M 30	-2.3	12.1	0.117	8547	0.170	13.0
M 92	-2.3	12.6	0.108	9259	0.072	12.5

Table 2.7: Globular cluster parameters

of metal-poor stars. In Fig.2.14 we can see that on average our metal-poor stars are older than all three GCs by about 1 Gyr. Also, it is worth mentioning that the width of the GC's age distribution shows that stars whose age is older than the age of the universe can be explained within the natural dispersion of the parameters in the same way as in GC.

2.9.3 Comparison with the three ancient stars HD 84937, HD 132475, and HD 140283

We made an additional sanity check by comparing our results with the three very old stars HD 84937, HD 132475, and HD 140283. They were studied by VandenBerg et al. (2014). HD 140283 was studied also by Bond et al. (2013). Both studies discovered that these stars are old and close to the age of the Universe. We used our age determination technique to derive their age. We used photometry and parallaxes from Gaia DR3, metallicity from

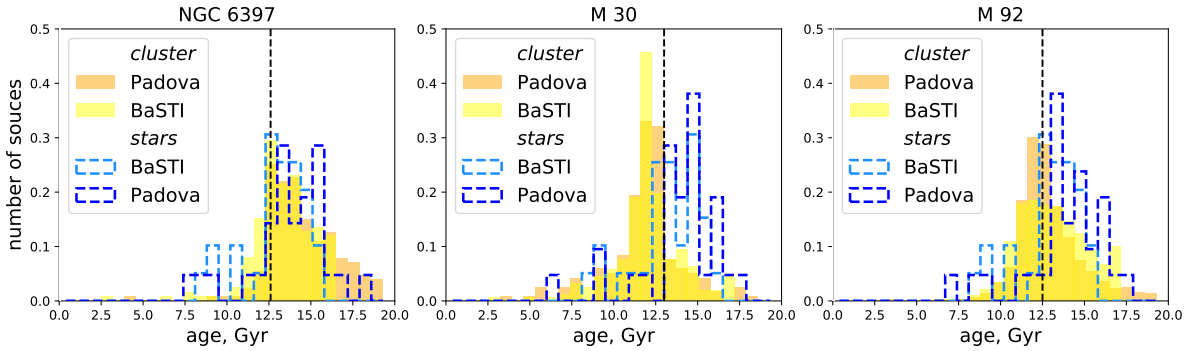

Figure 2.14: Dispersion of the age for GC NGC 6397, M 30, M92 compared with metal-poor stars under investigtion.

parameter	HD 84937	HD 132475	HD 140283
G, mag	8.207	8.391	7.036
G_{BP}, mag	8.423	8.692	7.321
G_{RP}, mag	7.817	7.898	6.562
π, mas	13.498	10.671	16.267
$\Delta\pi$, mas	0.044	0.025	0.026
$[Fe/H]$, dex	-2.0	-1.4	-2.4
$[\alpha/Fe]$, dex	0.38	0.45	0.26
A_V, mag	0.009	0.047	0.006
ΔA_V, mag	0.047	0.056	0.053

Table 2.8: VandenBerg et al. (2014) star parameters

the SIMBAD catalog[7], and reddening from Lallement et al. (2018). All parameters are listed in Tab.2.8. The resulting ages are shown in the Tab.2.9. We can see that our results are close to the previously derived ages and they coincide within the uncertainties.

2.9.4 Age averaging

Finally, we calculated the arithmetic and weighted average age for all the stars (Tab.2.10). The average age is very close to the age of the Universe that means that most of the stars under consideration were born recently after the Big Bang. The provided uncertainties take into account only the formal internal errors. But obviously we may have additional error's sources coming, for example, from isochrone's models: convection treatment, element diffusion (settlement of heavy elements and consequent wrong global metallicity derived from the actual stellar atmosphere Bonfanti et al. (2015)) and temperature-color transformations. There are also subtle effects due to overabundance of oxygen on the "shape" of the TO-point (VandenBerg et al. (2014)) and impact in opacity from C, Ca, Mg (Sec. 2.7). Another important external error could be the gas/dust ratio implied in the reddening derivation of the Lallement et al. (2018) map based on gas. We may reasonably suppose that they account for about 0.5 Gyr (this corresponds to an Av error of ± 0.05 mag at the MS turnoff). The comparison between the two different sets of isochrones

[7] http://simbad.u-strasbg.fr/simbad/sim-fbasic

star	source	BaSTI		Padova	
		age	error	age	error
HD 84937	G vs. G_{BP}-G	13.18	±1.40	12.03	±1.41
	G vs. G-G_{RP}	14.8	±1.05	13.96	±1.31
	G vs. G_{BP}-G_{RP}	14.21	±1.28	13.1	±1.22
	average	14.06	±1.51	13.03	±1.79
	VandenBerg et al. (2014)	12.08	±0.14		
HD 132475	G vs. G_{BP}-G	13.28	±1.27	13.16	±1.14
	G vs. G-G_{RP}	14.16	±1.27	14.09	±1.32
	G vs. G_{BP}-G_{RP}	13.68	±1.14	13.64	±1.18
	average	13.71	±0.81	13.63	±0.86
	VandenBerg et al. (2014)	12.56	±0.46		
HD 140283	G vs. G_{BP}-G	14.02	±1.27	14.13	±1.3
	G vs. G-G_{RP}	14.7	±1.17	15.24	±1.56
	G vs. G_{BP}-G_{RP}	14.51	±1.29	14.71	±1.44
	average	14.41	±0.65	14.69	±1.03
	VandenBerg et al. (2014)	14.27	±0.38		
	Bond et al. (2013)	14.46	±0.31		

Table 2.9: Age derived for VandenBerg et al. (2014) stars.

we use and our age determination of the three reference globular clusters suggest that 0.5 Gyr is a good estimation for our systematic error.

2.9.5 Age metallicity relation

The age metallicity relation (AMR) from G vs. G_{BP}-G, G vs. G-G_{RP}, G vs. G_{BP}-G_{RP} diagrams is presented in Fig.2.15 and for average age in Fig.2.16 together with three ancient stars from VandenBerg et al. (2014) and three metal-poor GC: NGC 6397, M30, M92. The first column show result from Padova isochrones and the second column is from BaSTI. For the comparison we took the Milky Way Globular cluster AMR from Dotter et al. (2011) (in paper Fig.10) and Cohen et al. (2021) (in paper Fig.4) (dashed lines

isochrone	filter	average age Gyr	error Gyr	weighted average age Gyr	error Gyr
Padova	G vs. BP-G	13.6	±1.3	13.7	±1.1
	G vs. G-RP	13.9	±1.4	14.1	±1.2
	G vs. BP-RP	13.8	±1.3	13.9	±1.1
	average	13.7	±0.5	13.9	±0.5
BaSTI	G vs. BP-G	13.4	±0.7	13.5	±0.7
	G vs. G-RP	13.6	±0.7	13.9	±0.7
	G vs. BP-RP	13.5	±0.8	13.7	±0.7
	average	13.5	±0.4	13.7	±0.4
Padova+BaSTI	average	13.8	±0.3	14.1	±0.3

Table 2.10: Average age of our stars

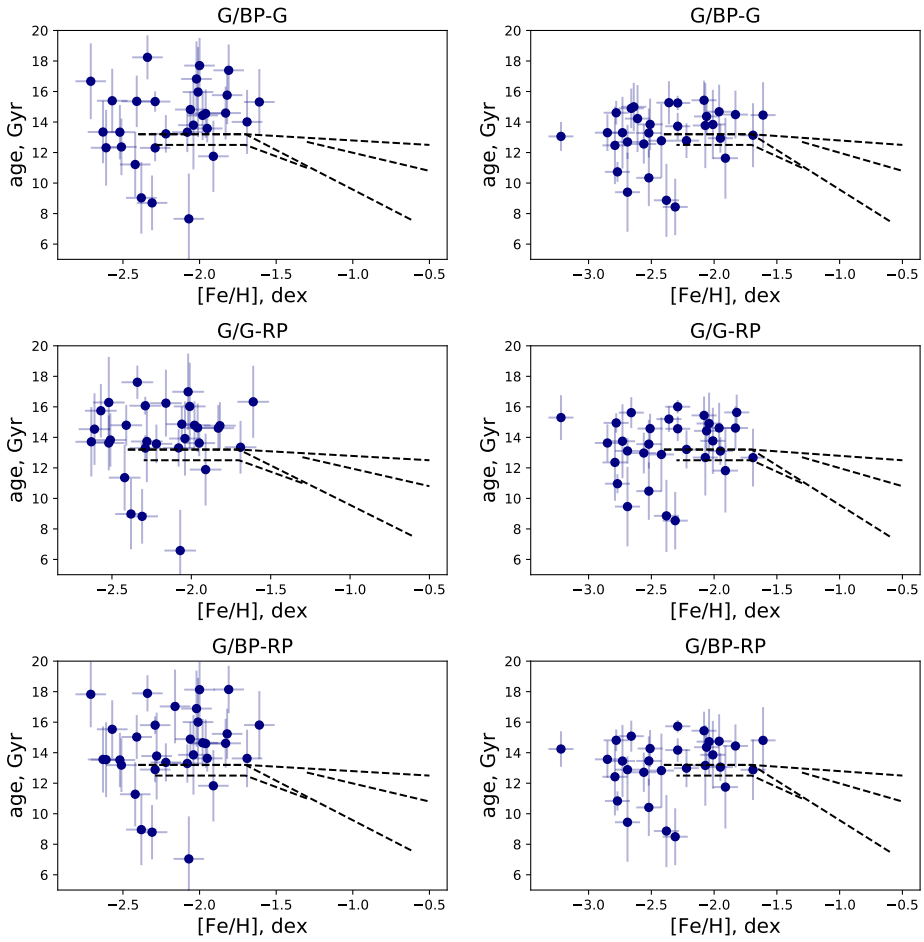

Figure 2.15: Age metallicity relation for ages from G vs. G_{BP}-G, G vs. G-G_{RP}, G vs. G_{BP}-G_{RP} diagrams. *First column*: ages are from Padova isochrones, *second column*: from BaSTI.

in Fig.2.15, 2.16). We can see that our stars extend the AMR to the lower metallicity side. On average metal-poor stars under investigation are older by about 0.8 Gyr than the main trends of the literature. And it is consistent with our results in Sec. 2.9.2, where we showed that GCs on average show younger ages compared with single metal-poor stars. The average age for data set under consideration is 13.7 ± 0.4 Gyr (BaSTI, 28 stars), 13.9 ± 0.5 Gyr (Padova, 17) and 14.1 ± 0.3 Gyr (from BaSTI and Padova, 17 stars). Moreover for metallicity between -2.7 – -2.0 dex we have a minor population with relatively younger ages around 8 – 10 Gyr. It can be an indication of two different populations or two epochs of star formation.

2.10 Conclusion

In this study, we derived the age of 28 metal-poor stars (Tab.2.6). The average age from Padova isochrones is 13.9 ± 0.5 Gyr, from BaSTI - 13.7 ± 0.4 Gyr and for star with both determination it is of 14.1 ± 0.3 Gyr (internal errors only). Our estimate for the additional systematic error is around 0.5 Gyr.

Age was derived by automatic isochrone CMD fitting using Gaia DR3 photometry

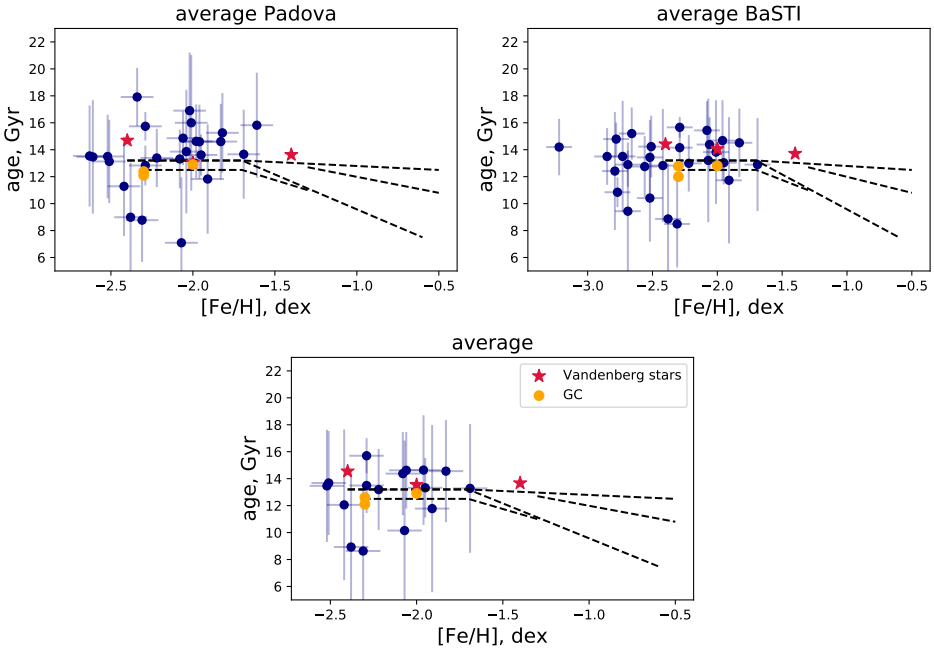

Figure 2.16: Average age metallicity relation for Padova (*left top*), BaSTI (*right top*) and Padova+BASTI averaged together (*bottom*). Red stars are VandenBerg et al. (2014) targets. Yellow dotes are three GC: NGC 6397, M 30, M92.

and the most updated parameters for distance and reddening. We considered also B,V photometry. Distance was chosen among four sources: Gaia DR3 (Gaia Collaboration (2021)), Gaia DR3 corrected by Lindegren et al. (2021), Bailer-Jones et al. (2021) and Queiroz et al. (2019) (`StarHorse`). Gaia DR3 parallaxes showed the best results in terms of CMD dispersion. We ascribe this result to the relative brightness of our stars. The best reddening estimate was obtained by combining two reddening maps Green et al. (2018) and Lallement et al. (2018) extended by Montalto et al. (2021).

We used two sets of isochrones, Padova and BaSTI. Padova isochrones produce on average 0.5 Gyr older age than BaSTI isochrones. Age determination can depend also on the detailed chemical composition of the stars. The enhancement of α-elements, C, N, O, and Ne can significantly affects the opacity of metal-poor stars and changes the continuum emission. The strongest effect is in the Johnson B filter (Fig.2.8). The effect is marginally present also in Gaia filters but, due to their width, it is much less prominent. We suggest that, in order to improve the age determination, specific isochrones should be computed for the chemical composition of each star.

In order to minimize the chemical composition effect in this work we used 3 different filter combinations of Gaia filters: G vs. G_{BP}-G, G vs. G-G_{RP}, G vs. G_{BP}-G_{RP}. We found that the age difference from one combination to the other is about 0.2 Gyr or less, smaller than the total uncertainty of the age determination method (more than 0.5 Gyr).

We checked our results against the three most metal-poor GC: NGC 6397, M 30, M 92. GC's ages derived by our automatic isochrone fitting technique are in good agreement with ages derived by other authors (Correnti et al. (2018) (NGC 6397), Kains et al. (2013) (M 30), VandenBerg et al. (2016) (M 92)). Moreover, our set of very metal-poor stars on average is older than the most metal-poor GC by about 1 Gyr.

Additionally, we compared our results with the ages of three nearby ancient halo

sub-giants (VandenBerg et al. (2014)). We found that our ages coincide within the uncertainties with the VandenBerg et al. (2014) and Bond et al. (2013) ages. Results are summarized in Tab.2.9.

Finally, we studied the age metallicity relation in its very metal-poor tail. The trend is almost horizontal, but our stars are on average older than mean locus found by other authors (Dotter et al. (2011), Cohen et al. (2021)) by about 0.8 Gyr. The interesting fact is that we found a group of very metal-poor stars with significantly young ages of 8 – 10 Gyr. The age of these stars can be a signature of two different populations or two epochs of star formation.

Acknowledgements

The comments of an anonymous referee have been much appreciated. AP acknowledges the Ulisse program of Padova University which allowed her to spend a period at Concepcion University, where part of this work has been done. SV gratefully acknowledges the support provided by Fondecyt regula n. 1220264 and by the ANID BASAL projects ACE210002 and FB210003.

Chapter 3

Very metal-poor stars in the solar vicinity: kinematics and abundance analysis

Based on:
Plotnikova A., Carraro G., Villanova S., Ortolani S.,
"Very metal-poor stars in the solar vicinity: kinematics and abundance analysis", 2023, ApJ 949, 31

Abstract

Very metal-poor stars contain crucial information on the Milky Way's infancy. In our previous study (Plotnikova et al. 2022) we derived a mean age of $\sim$ 13.7 Gyr for a sample of these stars in the Sun's vicinity. In this work, we investigate the chemical and kinematics properties of these stars with the goal of obtaining some insights on their origin and their parent population. We did not find any Al-Mg anti-correlation, which lead us to the conclusion that these stars did not form in globular clusters, while the detailed analysis of their orbital parameters reveals that these stars are most probably associated with the pristine Bulge of the Milky Way. We then sketch a scenario for the formation of the Milky Way in which the first structure to form was the Bulge through rapid collapse. The other components have grown later on, with a significant contribution of accreted structures.

3.1 Introduction

Very metal-poor stars are one of the best candidates to study the formation and evolution of the Universe and its Galactic components. The study of their chemistry and kinematics can help us to understand the chemical and dynamical properties of the first Population III supernovae. The origin of these stars contains important information about the Milky Way formation history.

Theoretical simulations of the Galaxy formation (Bullock &Johnston (2005)) have shown that the Halo bears the signatures of the Milky Way's assembly from smaller "building block" galaxies. Recent astrometric studies have shown the existence of kinematic signatures that indicate past accretion events (Belokurov et al. (2018); Myeong et al. (2019); Yuan et al. (2020)). That means that the kinematics of very metal-poor stars is an important testbed of the Galaxy formation and evolution theories. In fact,

stars with very low metal abundances are potential members of accreted dwarf galaxies and/or clusters.

Two main theories were suggested for the Milky Way formation. The first theory is the hierarchical scenario which tells us that our Galaxy was formed through the hierarchical merging of smaller dark halos. The accretion of baryonic matter occured later. The Bulge was formed first, followed by the Thin Disk. The Thick Disk could have been produced by the kinetic heating induced by small/medium mass engulfing companions.

The presence of stellar streams in the stellar Halo supports the hierarchical scenario (Helmi (2002), Ibata et al. (2002)): they are tidal remains of past merging events (Grillmair (2017)). Nowadays, we have a number of confirmed accreted events such as Sagittarius dwarf galaxy, Gaia-Enceladus/Sausage, Sequoia, Helmi stream, Thamnos, while other streams were found to be associated with accreted globular clusters (Koppelman et al. (2019)). The Halo of the Galaxy could have mostly be assembled in a sequence of minor mergers. Furthermore, the fact that the merging frequency is increasing with redshift, tells us that in the infant Galaxy merging events were quite common. That lends further support to the hierarchical scenario.

The second and most successful scenario is Secular Evolution (SE), with slow but continuous external matter accretion. According to this theory, the Bulge of the Galaxy was formed due to the accretion of disk matter through bar instabilities. This scenario is in agreement with the observed color gradient and the relation between the color of the bulge and disk studied through statistical analysis of 257 spiral galaxies (Gadotti &dos Anjos (2001)). SE is also supported by the relation between the bulge and disk masses and radii (Courteau et al. (1996)).

Metal-poor stars, being mostly ancient, are ideal probes of the early evolutionary phases of the Universe. Because of their low metallicity, they are linked to the most pristine star formation episodes in the Universe.

In this work, we build on (Plotnikova et al. 2022) and study the kinematics and abundances of a sample of very metal-poor stars in the solar vicinity. Therefore, the layout of this study is as follows. In Section 2 we discuss the data upon which our study is based. Section 3 and 4 are focused on the chemistry and kinematics of our stars, respectively. The results of our investigation are detailed in Section 5, while Section 6, finally, summarizes the outcome of this study and highlights future perspectives.

3.2 Data

As the main target for this investigation, we chose the data set of 28 very metal-poor stars for which we derived precise ages (Plotnikova et al. (2022)). These stars are of particular interest because they are very metal-poor and their average age is 13.7 ± 0.4 Gyr. As a result, the stars in this sample are valuable candidates to study the early stages of the Galaxy formation.

3.2.1 Distance determination

Distance is one of the most important parameters in dynamics studies. In Plotnikova et al. (2022) we compared the best distances, estimated out of four different techniques: Gaia DR3 parallaxes (Gaia Collaboration (2021)), Gaia EDR3 (Gaia Collaboration (2021)) corrected by Lindegren et al. (2021), the distances derived by Bailer-Jones et al. (2021),

Data product or source type	Typical uncertainty			
	G < 15	G = 17	G = 20	G = 21
Five-parameter astrometry				
position, mas	0.01 - 0.02	0.05	0.4	1
parallax, mas	0.02 - 0.03	0.07	0.5	1.3
proper motion, mas yr^{-1}	0.02 - 0.03	0.07	0.5	1.4
Six-parameter astrometry				
position, mas	0.02 - 0.03	0.08	0.4	1
parallax, mas	0.02 - 0.04	0.1	0.5	1.4
proper motion, mas yr^{-1}	0.02 - 0.04	0.1	0.6	1.5

Table 3.1: Uncertainties of Gaia Early Data Release 3 astrometry Gaia Collaboration (2021)

and Queiroz et al. (2019) (`StarHorse`). Our choice was made based on the best fit of the data with the isochrones in the color-magnitude diagram. As a result, we found that the best distances are those obtained directly from Gaia DR3 parallaxes (Plotnikova et al. (2022)).

3.2.2 Astrometric parameters

With the goal of calculating orbits and orbital parameters, we extracted coordinates, radial velocities, and proper motion components from the Gaia DR3 archive (Gaia Collaboration et al. (2022b)). Uncertainties for astrometric parameters are shown in Tab.4.2. Position and velocity of the stars in the Equatorial Coordinates were transformed to Galactocentric coordinates by `astropy`[1] python package.

3.3 Chemistry

All our stars are from Hamburg vs. ESO R-process Enhanced Star (HERES) survey. The chemical abundances were spectroscopically studied by Barklem et al. (2005). The spectrum synthesis assumes LTE and a 1D plane-parallel model of the atmosphere, where turbulence is modeled through the classical micro-turbulence and macro-turbulence parameters. Their "snapshot" spectra cover a wavelength range of 3760 – 4980 Å and have an average signal-to-noise ratio of S/N $\sim$ 54 per pixel over the entire spectral range. A 2″ slit is employed giving a minimum resolving power of $R \approx 20000$. From the "snapshot" spectra the elemental abundances of moderate precision (absolute r.m.s. errors of order 0.25 dex, relative r.m.s. errors of order 0.15 dex) have been obtained for 22 elements: C, Mg, Al, Ca, Sc, Ti, V, Cr, Mn, Fe, Co, Ni, Zn, Sr, Y, Zr, Ba, La, Ce, Nd, Sm, and Eu. The abundances used in this work are listed in Tab.3.2.

[1] https://docs.astropy.org/en/stable/_modules/astropy/coordinates/builtin_frames/galactocentric.htmlastropy

ID	[Mg/Fe] dex	[Al/Fe]$_{LTE}$ dex	[Al/Fe]$_{NLTE}$ dex	[Ca/Fe] dex	[Cr/Fe] dex	[Ti/Fe] dex	[Ni/Fe] dex	[Fe/H] dex	age Gyr	Origin*
HE_0023-4825	0.22	-1.01	-0.51	0.26	0.00	0.31	-0.01	-2.06	14.62 ± 0.11	Pr.B.
HE_0109-3711	-	-	-	0.42	-0.06	0.38	-	-1.91	11.78 ± 0.04	5G/GE
HE_0231-4016	0.22	-1.09	-0.50	0.36	-0.11	0.25	-0.14	-2.08	14.37 ± 0.47	Pr.B.
HE_0340-3430	0.19	-1.00	-0.61	0.36	-0.16	0.25	-0.26	-1.95	13.32 ± 0.13	5G/GE
HE_0430-4404	0.29	-0.97	-0.57	0.33	-0.02	0.32	0.01	-2.07	10.15 ± 1.38	Th.1
HE_0447-4858	0.24	-0.81	-0.42	0.24	0.09	0.28	0.33	-1.69	13.28 ± 0.20	5G/GE
HE_0501-5139	0.19	-	-	0.34	-0.24	0.39	-0.13	-2.38	8.93 ± 0.03	Th.1
HE_0519-5525	0.41	-0.76	-0.26	0.37	-0.19	0.37	0.13	-2.52	13.46 ± 0.06	5G/GE
HE_0534-4615	0.22	-0.87	-0.37	0.28	-0.18	0.19	-0.20	-2.01	14.91 ± 0.49	Pr.B.
HE_1052-2548	0.16	-0.48	-0.11	0.27	-0.12	0.45	0.03	-2.29	15.70 ± 0.14	Pr.B.
HE_1105+0027	0.47	-0.89	-0.33	0.47	0.05	0.32	-0.29	-2.42	12.06 ± 0.35	Th.1
HE_1225-0515	0.18	-1.00	-0.62	0.27	-0.08	0.34	-0.16	-1.96	14.64 ± 0.03	Pr.B.
HE_1330-0354	0.32	-0.93	-0.46	0.40	-0.05	0.54	-0.08	-2.29	13.49 ± 0.34	SimD
HE_2250-2132	0.31	-1.07	-0.57	0.29	-0.12	0.35	0.05	-2.22	13.19 ± 0.11	SimD
HE_2347-1254	0.29	-0.74	-0.42	0.37	-0.13	0.39	-0.16	-1.83	14.56 ± 0.03	Pr.B.
HE_2347-1448	0.13	-1.11	-0.64	0.21	-0.05	0.31	0.27	-2.31	8.63 ± 0.07	5G/GE
HE_0244-4111	0.34	-	-	0.37	-0.19	0.30	0.00	-2.56	12.75 ± 0.51	Th.1
HE_0441-4343	0.32	-1.09	-0.59	0.18	-0.36	0.27	0.07	-2.52	10.41 ± 0.50	Th.1
HE_0513-4557	0.34	-	-	0.21	-	-	-	-2.79	12.42 ± 0.50	OrNC
HE_0926-0508	0.28	-0.90	-0.49	0.37	-0.14	0.49	-0.06	-2.78	14.79 ± 0.51	Pr.B.
HE_1006-2218	-	-0.79	-0.46	0.32	-0.11	0.48	-	-2.69	12.90 ± 0.51	Th.2
HE_1015-0027	0.35	-1.00	-0.67	0.41	-0.24	0.55	-0.10	-2.66	15.20 ± 0.55	Pr.B.
HE_1126-1735	0.31	-1.06	-0.46	0.32	-0.29	0.33	-0.04	-2.69	9.44 ± 0.50	GE
HE_1413-1954	-	-	-	0.33	-	-	-	-3.22	14.20 ± 0.82	Pr.B.
HE_2222-4156	0.42	-0.93	-0.42	0.35	-0.21	0.33	-0.02	-2.73	13.50 ± 0.52	Th.1
HE_2325-0755	0.31	-1.02	-0.42	0.46	-0.29	0.35	-0.18	-2.85	13.50 ± 0.51	SimD

GE - Gaia-Enceladus/Sausage, Th.1 - Thamnos 1, Th.2 - Thamnos 2, Pr.B. - primordial bulge, 5G/GE - 5 stars group, high probability to belong to the GE, SimD - similar to the disk kinematics, OrNC - origin is not clear, stars have halo kinematics and chemistry.

Table 3.2: Chemistry

3.3.1 Non-LTE corrections

As mentioned above, spectral analysis in Barklem et al. (2005) was done assuming only the LTE model. However, aluminum abundance was obtained from the lines in the ultraviolet part of the spectrum that are significantly affected by Non-LTE effects (Nordlander &Lind (2017)). To improve the precision of the chemical parameters we applied Non-LTE correction from Nordlander &Lind (2017). The correction was implemented for each star according to its effective temperature (T_{eff}), metallicity ($[Fe/H]$) and gravity ($logg$). The resulting obtained corrections are on average around 0.5 dex (Tab.3.2).

We also checked Non-LTE corrections for all other elements by means of MPIA webtool database[2] but in all cases, corrections are less than 0.1 dex and were considered negligible.

3.4 Kinematics

We obtained orbits and orbital parameters for all stars in the data set using parallaxes, proper motion and radial velocities from Gaia DR3 by numerical calculation and adopting a model of Galactic potentials. The results are then analyzed to obtain insights on the stars' origin.

3.4.1 Galactic axisymmetric potential

We corrected the velocities of the stars by the velocity of the Sun with respect to the Galactic center which is computed independently from the velocity of the local standard of rest (Reid &Brunthaler (2004), GRAVITY Collaboration et al. (2018), Drimmel &Poggio (2018)):

$$v_{R\odot} = -12.9 \pm 3.0 \text{ km s}^{-1} \tag{3.1}$$

$$v_{\phi\odot} = 245.6 \pm 1.4 \text{ km s}^{-1} \tag{3.2}$$

$$v_{Z\odot} = 7.78 \pm 0.09 \text{ km s}^{-1} \tag{3.3}$$

where the distance between the Galactic center and the Sun is $R_0 = 8.122 \pm 0.033$ kpc (GRAVITY Collaboration et al. (2018)). We used the McMillan (2017) Galactic potential without bar implementation in `galpy`[3] (Bovy (2015)) to calculate orbits and orbital parameters such as the total energy (E_n), eccentricity (e), apo-center (R_{apo}), and peri-center (R_{peri}).

3.4.2 Galactic non-axisymmetric potential

To take into account the effect of the bar we replaced the axisymmetric bulge from McMillan (2017) with a non-axisymmetric elongated bar/bulge component. As a model for the bar/bulge structure, we used the rotating ellipsoid (Chemel et al. (2018), Yeh et al. (2020)) with density distribution given by Ferrers formula:(Bovy (2015)):

$$\rho(x,y,z) = \begin{cases} \rho_c(1-m^2)^2 & , \text{ if } m < 1, \\ 0 & , \text{ if } m > 1, \end{cases} \tag{3.4}$$

[2] https://nlte.mpia.de
[3] http://github.com/jobovy/galpy

where $m^2 = \frac{x^2}{a^2} + \frac{y^2}{b^2} + \frac{z^2}{c^2}$. For the parameters, we used $a = 5$ kpc, $b = 2$ kpc, $c = 1$ kpc which gives a good approximation for the observed bar/bulge component in the center of the Milky Way (Portail et al. (2015), Portail et al. (2017)). The central density of the bar is given by $\rho = \frac{105}{32\pi}\frac{GM_b}{abc}$, where the mass of the bar $M_b = 1.88 \times 10^{10}$ $M_\odot$ (Portail et al. (2017)).

The Milky Way bar is rotating around the Galactic center with constant angular velocity Ω_b. Also, its major axis is tilted with respect to the Sun.

Recent measurements of bar angular velocity give the following results: $\Omega_b = 41 \pm 3$ km s^{-1} kpc^{-1} (Sanders et al. (2019)), $\Omega_b = 37.5$ km s^{-1} kpc^{-1} (Clarke et al. (2019)), $\Omega_b = 40$ km s^{-1} kpc^{-1} (Sormani et al. (2015)). In this work we used bar angular velocity $\Omega_b = 40$ km s^{-1} kpc^{-1} which is in a good agreement with Portail et al. (2015), Portail et al. (2017), and Bovy et al. (2019). For the bar orientation relative to the Sun we used $\phi = 28^o$ which is in good agreement with recent estimates (Wegg &Gerhard (2013), Bland-Hawthorn &Gerhard (2016), and Portail et al. (2017)).

3.4.3 Uncertainty

To estimate uncertainties for each derived orbital parameter we perform a Monte Carlo analysis using 1000 random draws on the input parameters: parallax, radial velocity and proper motion. We considered errors in right ascension (RA) and declination (DEC) to be negligible compared to other parameters. As for proper motion, we used the multivariate normal distribution which takes into account the correlation between both components[4]. For parallax and radial velocity we used just normal distribution.

Since we use parallaxes, the resulting distribution of each orbital parameter is not Gaussian. Therefore, we derived for each orbital parameter a median value and a confidence interval of 68%.

3.5 Results

We studied the chemical composition and kinematics of our data set of 28 metal-poor stars and the correlation with their age.

3.5.1 Chemistry

In Fig.3.1 we compared the chemical composition of our data set with bulge (red open triangles, Howes et al. (2016)) and halo (grey circles, Yong et al. (2013), Roederer et al. (2014)) stars of the Milky Way. Inspecting this figure one can readily see that all our stars are in good agreement with the typical trends for Milky Way stars. This holds except for aluminum, whose position is shifted on average by 0.2 dex. For all stars we applied non-LTE correction from Nordlander &Lind (2017) that play important role in aluminum abundance.

To separate stars from the Halo, the Thin, and the Thick disk stars we used the Al versus Mg map (Fig.4.4). For comparison we used for Disk: Fulbright (2000), Reddy et al. (2003), Simmerer (2004), Reddy et al. (2006), François et al. (2007), Johnson et al. (2012),

[4] https://gea.esac.esa.int/archive/documentation/GEDR3/Gaia_archive/chap_datamodel/sec_dm_main_tables/ssec_dm_gaia_source.html

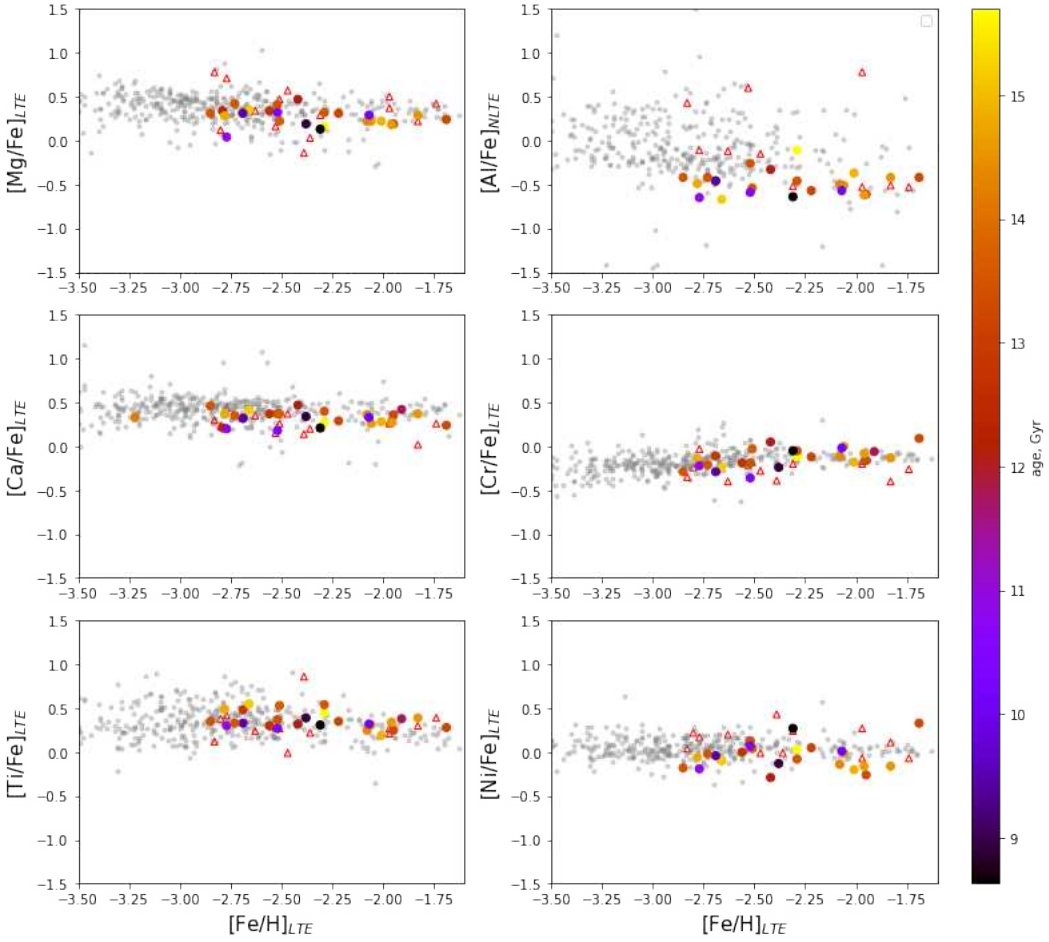

Figure 3.1: Correlation between iron and other chemical elements color-coded with the age. For comparison we show Bulge (red open triangles, Howes et al. (2016)) and Halo (grey circles, Yong et al. (2013), Roederer et al. (2014)) stars of the Milky Way. For all sources Al correction from Nordlander &Lind (2017) was applied.

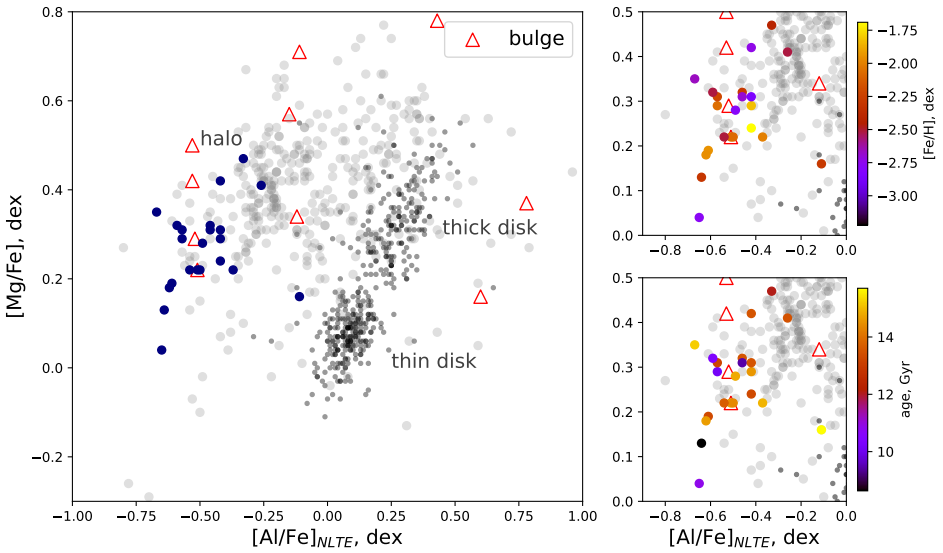

Figure 3.2: Al-Mg correlation. *Top right*: color-coded with metallicity, *bottom right*: color coded with age. The background: disk stars (*black dotes*, Fulbright (2000), Reddy et al. (2003), Simmerer (2004), Reddy et al. (2006), François et al. (2007), Johnson et al. (2012), Johnson et al. (2014)), halo stars (*grey points*, Yong et al. (2013)), Roederer et al. (2014), bulge stars (*red open triangles*, Howes et al. (2016)).

Johnson et al. (2014); for Halo: Yong et al. (2013), Roederer et al. (2014); and for Bulge: Howes et al. (2016). All our stars having measures for both elements occupy the expected region for halo stars. At odds with globular clusters' stars, our sample stars do not show any Al-Mg anti-correlation (Lucey et al. (2022), Sestito et al. (2022)). Also, it is worth mentioning that only 1-3% of halo stars have globular cluster origin (observations:Martell et al. (2011); Martocchia et al. (2023); simulations:Reina-Campos et al. (2020))

We can therefore conclude that our stars possess the typical chemical composition of the Milky Way Halo field stars. The lack of any anti-correlation seems to exclude an origin inside globular clusters.

3.5.2 Kinematics

To get additional insight on the origin of these stars we explore their kinematical properties. To this aim, in Fig.3.3 we compared our results with Koppelman et al. (2019). We used the same McMillan (2017) potential as in Koppelman et al. (2019) but, after checking that there are no differences, we adopted the most recent estimates of the Sun's velocity and distance to the Galactic center (Sec.3.4.1). Fig.3.3 shows that some of the stars share the same kinematics as well-known accretion events: the Gaia-Enceladus/Sausage system (*orange*; Belokurov et al. (2018), Helmi et al. (2018)) and Thamnos 1,2 (*darkblue*,*blue*; Koppelman et al. (2019)). This result is also supported by the velocity and L_z-eccentricity diagrams (Fig.3.4).

Besides, we can notice a group of 5 stars below the Gaia-Enceladus/Sausage locus with similar orbital parameters, age, and metallicity, and location inside the sphere with radius R$\sim$1 kpc. In some sources, Gaia-Enceladus/Sausage locus is extended to lower energies (Koppelman et al. (2019)) which gives a higher probability for this 5 stars group

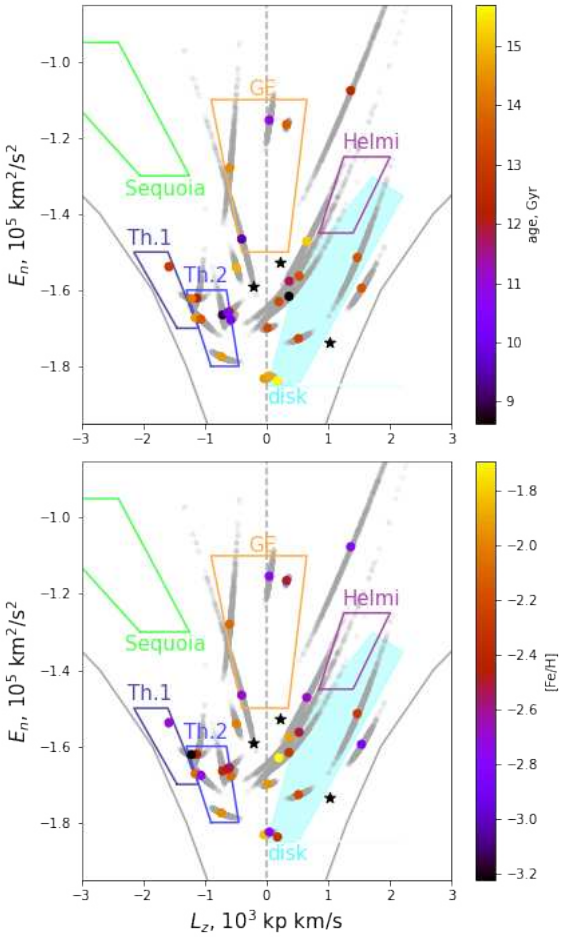

Figure 3.3: $E_n - L_z$ diagram with the loci of the biggest known accretion events: Gaia-Enceladus/Sausage (GE) (*orange*), Helmi stream (*purple*), Sequoia (*green*), Thamnos 1, 2 (*darkblue, blue*); and disk (*cyan*). Black star symbols indicate Vandenberg halo stars VandenBerg et al. (2014). The colored points are mean values of stars under investigations, while grey trials indicate their uncertainties.

to be indeed part of Gaia-Enceladus/Sausage. Also, there are three stars (Fig.3.4, *black dotes*) that have similar to the disk kinematics. Although, their chemistry is a halo like.

Our stars exhibit both prograde and retrograde motion and they cover almost the entire eccentricity range (Fig.3.4, *lower panel*). Additionally, all stars are distributed around $v_\phi = 0$ km/s which indicates a typical Halo kinematics (Fig.3.4, *upper right panel*). They might be part either of Gaia-Enceladus/Sausage (GE) (*orange*), or of Thamnos 1, 2 (*dark blue, blue*) accretion events. All diagrams in Fig.3.4 are color-coded according to their position in the $L_z - E_n$ diagram (Fig.3.4, *upper left panel*)

However, the kinematic analysis alone is not sufficient to identify the origin of these stars and decipher whether they are associated or not with a specific accreted structure. To check the possible membership of *blue* and *orange* stars to Gaia-Enceladus/Sausage (GE) (*orange*) or Thamnos 1, 2 (*dark blue, blue*) we need to combine kinematics with chemistry. In Fig.3.5 we can see that both Milky Way stars and accretion events possess similar chemistry.

Overall, our metal-poor stars have chemistry compatible with accretion event trends.

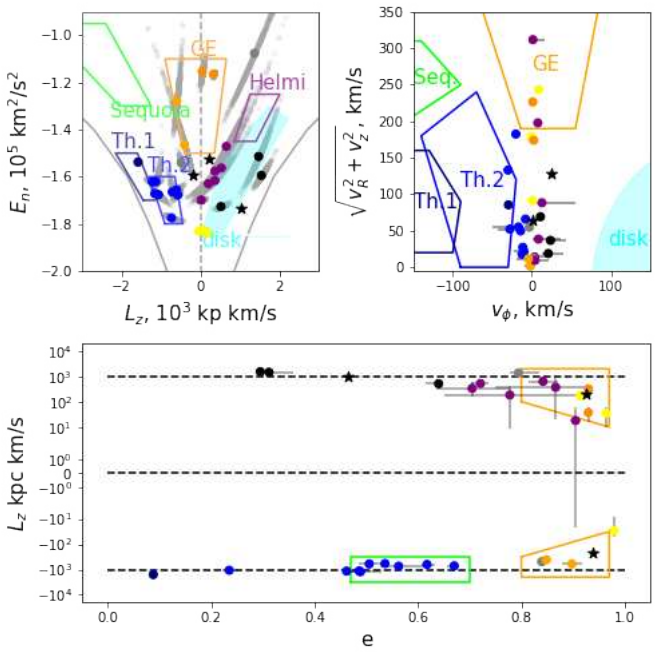

Figure 3.4: Points are color-coded with the position in $E_n - L_z$ diagram: Gaia-Enceladus/Sausage (GE) (*orange*), Sequoia (*green*), Thamnos 1, 2 (Th.) (*dark blue, blue*), Sagittarius (*red*), disk (*black*), group of 5 stars with similar parameters (*purple*), low energy stars (*yellow*), Vandenberg stars VandenBerg et al. (2014) (*black stars*).

Additionally, we compared the age of the stars with the age of each accretion event (Fig.3.6) and a part of the star's ages fall into the range of the beginning of the accreting blocks' formation. But some of the stars from this work are older and can be excluded from being accreted through known accretion events.

3.5.3 Orbital parameters

In Fig.3.7 we presented the correlation between eccentricity (e), peri-centre (R_{peri}), maximum height above the galactic plane (Z_{max}) and apo-centre (R_{apo}) color-coded with age. From the upper plot in Fig.3.7 we can notice that almost all stars in our data set cross the bulge region. That means that these stars' kinematics is perturbed by the bar/bulge potential. One can also speculate that they can be a part of the pristine bulge of the Milky Way. From the middle plot in Fig.3.7 we can see that the most distant stars exhibit on average more elongated orbits. The lower plot in Fig.3.7 shows that most of the stars have $R_{apo} > Z_{max}$, i.e. they lie close to the Galactic plane. Another intriguing evidence in this plot is that one can readily see a clear trend in age: the oldest stars (yellow) are located lower to the plane while the younger (redder) stars lie closer to the dashed line $R_{apo} = Z_{max}$.

By inspecting Fig.3.8 we can highlight also the following trends:

1. Eccentricity is increasing with increasing age.

2. The older stars orbit closer to the Galactic center and the Galactic disk.

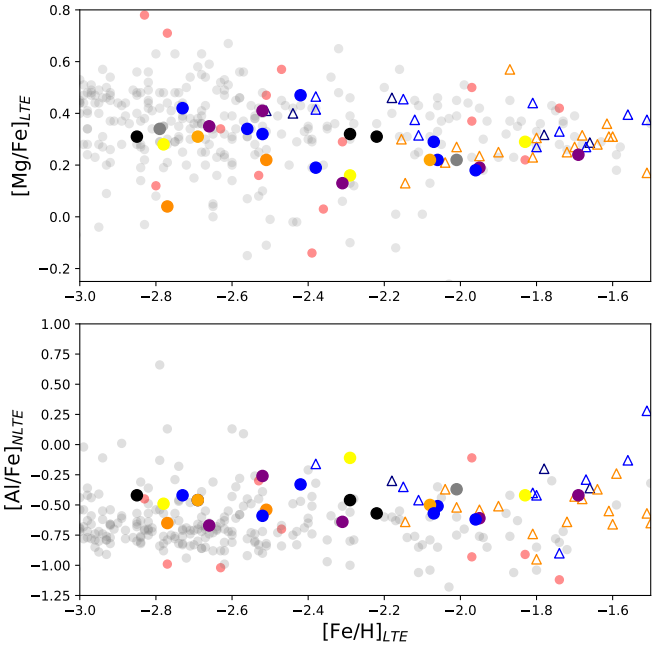

Figure 3.5: Correlation between Mg, Al and Fe. For comparison, we showed bulge (red circles, Howes et al. (2016)) and halo (grey circles, Yong et al. (2013), Roederer et al. (2014)) stars of the Milky Way. Points are color-coded with the position in $E_n - L_z$ diagram: Gaia-Enceladus/Sausage (GE) (*orange*), Sequoia (*green*), Thamnos 1, 2 (Th.) (*dark blue, blue*), Sagittarius (*red*), disk (*black*), group of 5 stars with similar parameters (*purple*), low energy stars (*yellow*). *Circles* - stars from this work, *open triangles* - stars from known accretion events (Koppelman et al. (2019)).

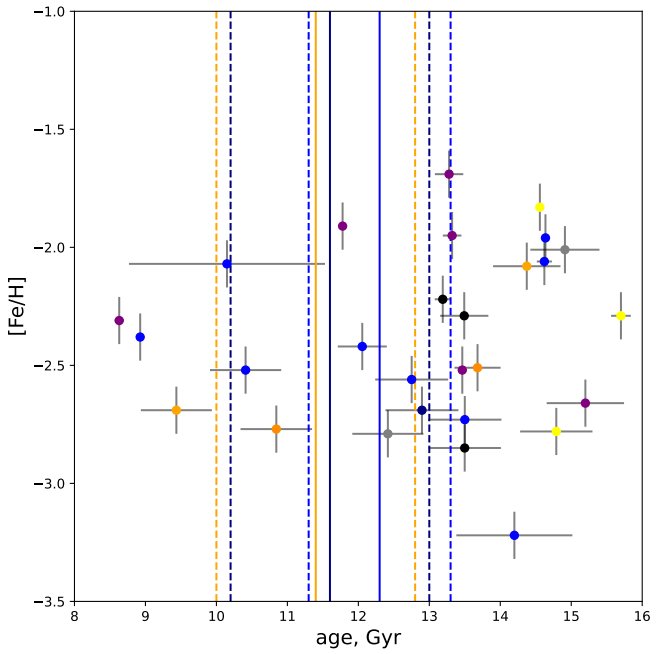

Figure 3.6: Age-metallicity relation with the time bars of the Gaia-Enceladus/Sausage (GE) (*orange*), Thamnos 1, 2 (*dark blue, blue*) formation (Ruiz-Lara et al. (2022)). Solid lines are main values and dashed lines represent uncertainties.

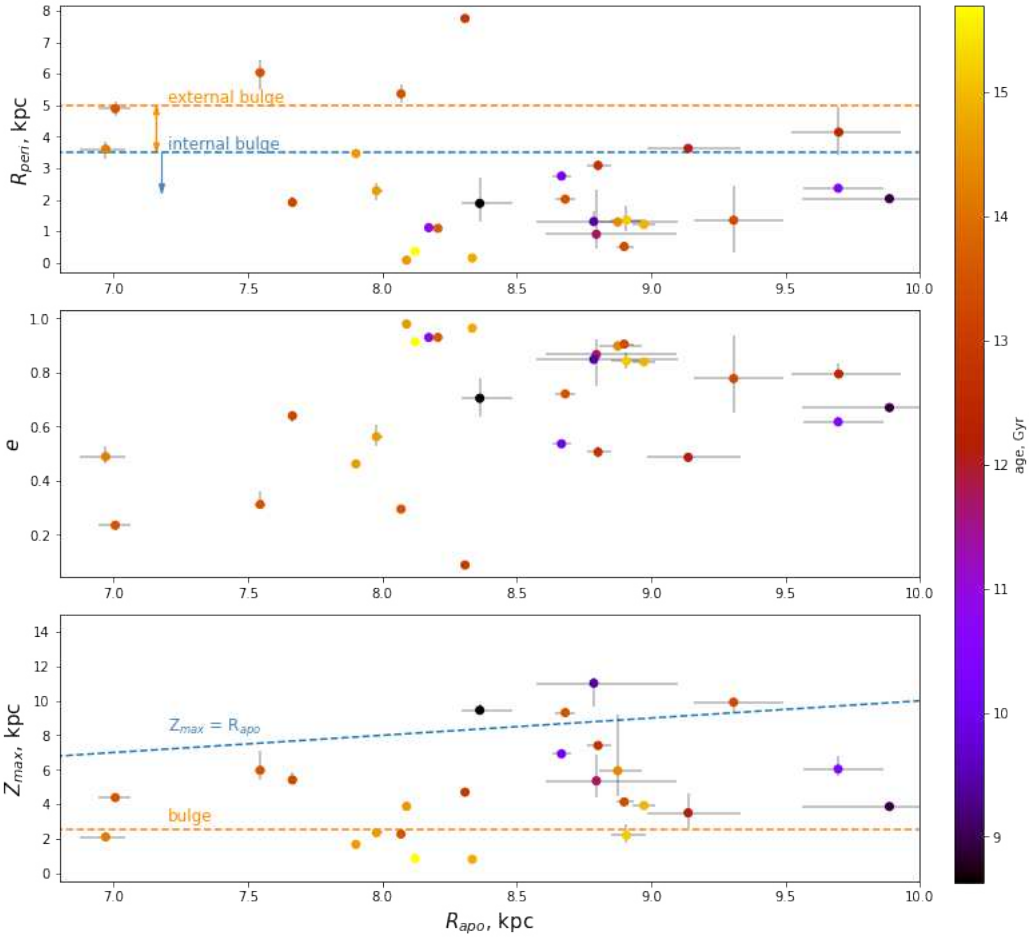

Figure 3.7: Correlation between eccentricity (e), pericentre (R_{peri}), maximum height under the galactic plane (Z_{max}) and apocentre (R_{apo}) color-coded with age.

Very old stars

Let us draw our attention to stars with ages larger than 13.5 Gyr. Their age implies they have a very low probability to be part of any well-known accretion events (Fig.3.6). Additionally, their age is very close to the age of the Universe and the very first instants of the Milky Way formation. We then speculate that they can have formed inside the very first "building blocks" of the Milky Way and therefore were part of the infant bulge at a time when the Disk had yet to form (Carraro et al. (1999)).

Moreover, all of them have orbits close to the Galactic Disk and pass close to the Galactic center while crossing the Galactic bulge. This might lend further support to a scenario in which these stars were formed in a pristine Bulge and later displaced in larger eccentricity orbits by some migration phenomenon. The same result was obtained by Grenon (1985) for metal-rich bulge stars in the solar vicinity. However, closeness to the galactic plane is rather the result of the observational limitations (all of our stars lie inside 5 kpc sphere around the Sun) than an intrinsic feature. We consider that with better observations there is a probability to find old metal-poor stars passing through the bulge in elongated orbits in all directions from the Galactic center.

Moving back to chemistry, stars under investigation are α-enhanced, and close to typical of today's Milky Way Halo stars. Speaking about bulge stars, according to Howes et al. (2016) data, chemical composition of Bulge stars is more disperse than Halo stars but distributed around the same mean that makes it impossible to distinguish between Bulge and Halo stars. Still, and interestingly, for all stars in our data set there is a clear correlation between the abundance of α-elements and age (Fig.3.9) with weighted Person correlation coefficient equal 0.24. This is due to the fact that for low metallicity stars the main source of α-elements is supernovae of type II (SNe II). An increasing α-abundance can be a signature of an environment where gas density and star formation were quite high. This seems to be another argument in favor of the idea that our oldest stars were associated with the ancient bulge.

3.5.4 Non-axisymmetric bar/bulge potential

Since most of our stars orbit close to the Galactic center ($R_{peri} < 3.5$ kpc) we additionally studied their kinematics in a non-axisymmetric bar/bulge potential (Sec.3.4.2).

In Fig.3.10 we can see that first of all changing the potential modifies the total energy (E_n) that stars possess nowadays. Besides, in their motion in the Galactic non-axisymmetric bar potential, both total energy and the angular momentum component along the z-axis evolve with time. Clearly, total energy and angular momentum along the z-axis do not conserve anymore. The Jacobi integral $E_J = E_n - \Omega_b L_z$ is constant instead. As a result of the bulge/bar time evolution E_n anti-correlates with L_z in the same fashion (same slope) for all the stars (Tkachenko et al. (2023)). For some stars, these changes are large and move them far from the location they had in the axisymmetric potential. This highlights the importance of bar/bulge structure in the dynamical evolution of these stars. However, it is worth mentioning that for the stars we identified to be probable members of accretion events the change in position due to bar perturbations is not significant. The shifted points in $E_n - L_z$ diagram are still well inside the accretion events' regions (GE, Thamnos 1,2).

For both potentials, we run simulations 1 Gyr long in time with step $\Delta t = 0.1$ Myr. For non-axisymmetric potential, though, we did not calculate uncertainties since it is a

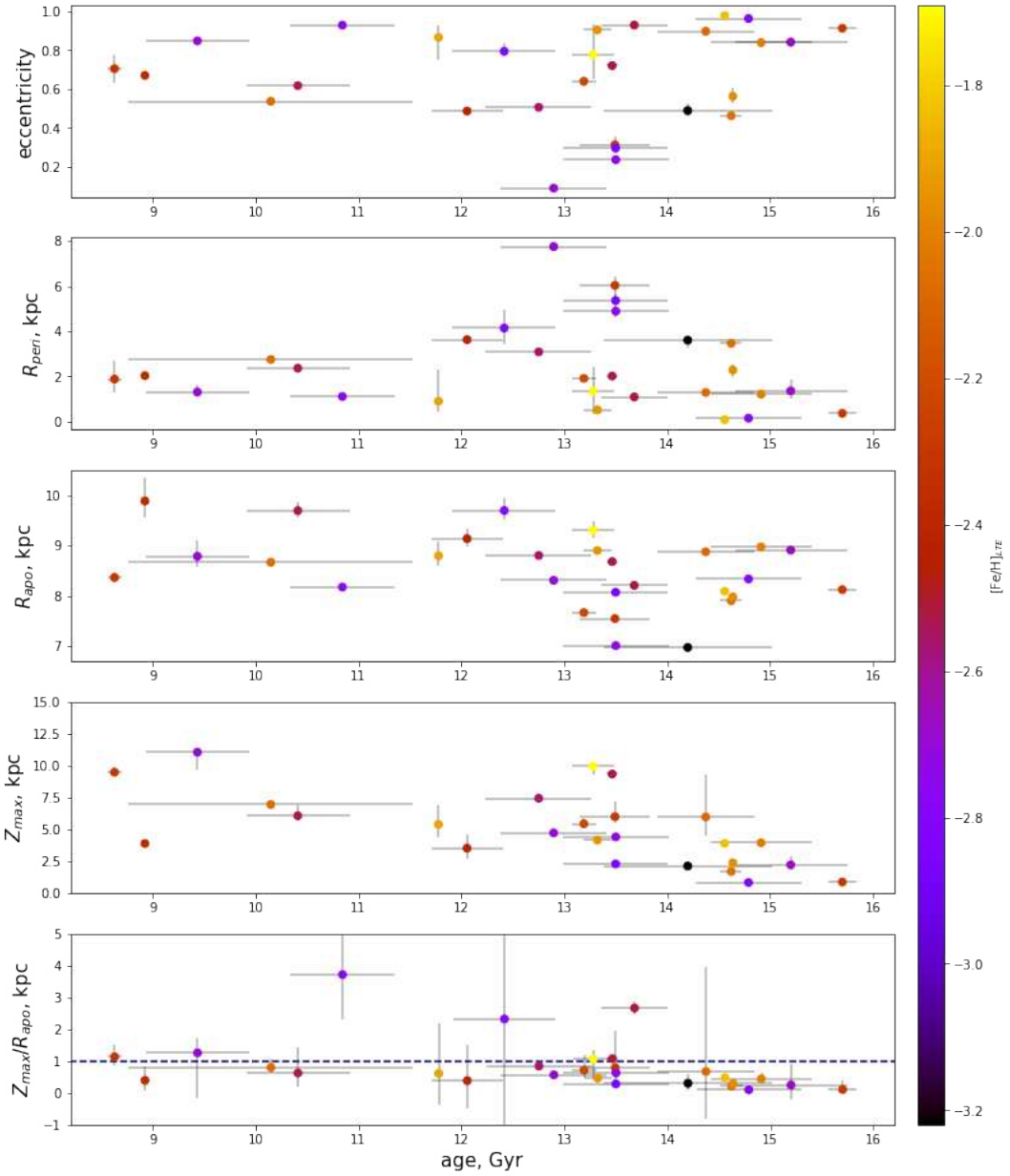

Figure 3.8: Correlation between eccentricity (e), pericentre (R_{peri}), apocentre (R_{apo}), maximum height under the galactic plane (Z_{max}), Z_{max}/R_{apo} and age color-coded with metallicity.

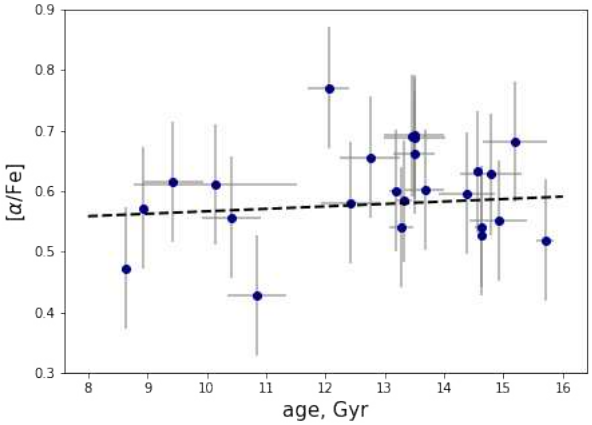

Figure 3.9: Correlation between α-elements and age. The dashed line show the main trend.

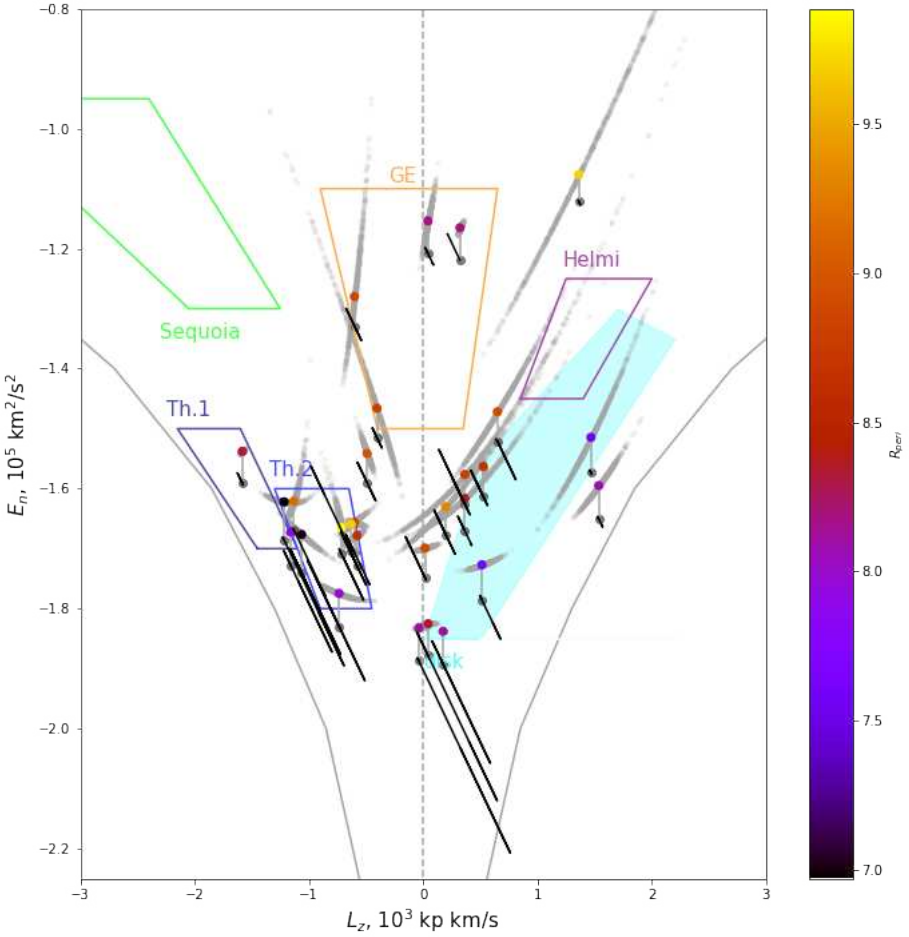

Figure 3.10: Comparison of the position in $E_n - L_z$ diagram calculated in axisymmetric (colored points with blue error bars) and non-axisymmetric (black tilted lines) potentials. $E_n - L_z$ diagram with the loci of the biggest known accretion events: Gaia-Enceladus/Sausage (GE) (*orange*), Helmi stream (*purple*), Sequoia (*green*), Thamnos 1, 2 (*darkblue, blue*); and disk (*cyan*).

highly time-consuming process.

3.6 Conclusion

Three main parameters that can be used to obtain the origin of the star are: kinematics, chemistry and age. In this study, we explored all three of them for a sample of 28 very metal-poor stars for whom we had previously derived ages ((Plotnikova et al. 2022)). Kinematics and chemistry are routinely used to assign stars to different components of the Milky Way galaxy, or to the various accreted systems that have been identified over the years in the Galactic halo. The basic conclusions of our study can be summarized as follows:

1. We have identified a group of stars with clear signatures of Halo population according to their chemistry, age, and kinematics. However, we speculate that several of them, the oldest 8 indeed, could have formed in the primordial Bulge because of their orbital parameters (large eccentricity and low Z_{max} mostly) and large α-abundance.

2. We have identified another group of stars that we tentatively associate with Gaia-Enceladus/Sausage (GE) (*orange*), and Thamnos 1, 2 (*dark blue, blue*) according to their similarity in kinematics, chemistry and age.

The identification of a group, although small, of stars probably belonging to the infant Bulge is rather intriguing. In fact, it supports a scenario in which the first component of the Milky Way to form was the Bulge via a fast collapse *a là* ELS (Eggen et al. (1962)). The other components have then assembled with a major contribution from systems that engulfed into the Milky Way later on, in agreement with the widely accepted merging scheme (Searle &Zinn (1978)).

Acknowledgements

The comments of an anonymous referee have been much appreciated. AP acknowledges the Ulisse program of Padova University which allowed her to spend a period at Concepcion University, where part of this work has been done. Also, AP acknowledges Roman Tkachenko for the useful consultations. SV gratefully acknowledges the support provided by Fondecyt regular n. 1220264 and by the ANID BASAL projects ACE210002 and FB210003. SO acknowledges DOR 2020, University of Padova.

Chapter 4

The chemical evolution of the Milky Way Thin disk using solar twins

Based on:
Plotnikova A., Spina L., Ratcliffe B., Casali G., Carraro G.,
"The chemical evolution of the Milky Way Thin disk using solar twins", submited to A&A

Abstract

In this study we address whether the age–metallicity relation (AMR) deviates from the expected trend of metallicity increasing smoothly with age. We also show the presence (or absence) of two populations, as recently claimed using a relatively small dataset. Moreover, we studied the Milky Way thin disk's chemical evolution using solar twins, including the effect of radial migration and accretion events. In particular, we exploited high-resolution spectroscopy of a large sample of solar twins in tandem with an accurate age determination to investigate the Milky Way thin disk age-metallicity relationship. Additionally, we derived the stars' birth radius and studied the chemical evolution of the thin disk. We discovered that statistical and selection biases can lead to a misinterpretation of the observational data. An accurate accounting of all the uncertainties led us to detect no separation in the AMR into different populations for solar twins around the Sun ($-0.3 < [Fe/H] < 0.3$ dex). This lead us to the conclusion that the thin disk was formed relatively smoothly. For the main scenario of the Milky Way thin disk formation, we suggest that the main mechanism for reaching today's chemical composition around the Sun is radial migration with the possible contribution of well-known accretion events such as *Gaia*-Enceladus/Sausage (GES) and Sagittarius (Sgr).

4.1 Introduction

The Milky Way formation and evolution is one of the most important topics in modern astronomical research. Using the advantage of our location from inside we can study it in great detail. Based on different observational results several models of Galaxy formation were suggested in the past. First to form was the infant metal-poor Bulge through rapid collapse (see e.g. Plotnikova et al. (2023) and references therein). Then 11 - 12 Gyr ago the Thick disk and the Halo were formed (Chiappini et al. 1997) according to the simple closed box model with instantaneous mixing of produced elements (Pagel 1997)

where metallicity increases smoothly with time (Sahlholdt et al. 2022). Later on, around 10 Gyr ago, the Thin disk started to form (Chiappini et al. 1997). Its formation created a double population in the alpha-metallicity diagram (Yoshii 1982; Gilmore &Reid 1983). According to the (Chiappini et al. 1997) model, two infall episodes originated the halo-thick disk and thin disk, respectively. About 10 Gyr is the time found for the second infall in the revised two-infall model by (Spitoni et al. 2019) which is designed to reproduce the two alpha-abundance sequences observed in the solar neighborhood. More recently, several other models were suggested assuming as second infall the accretion of the gas previously ejected into the Halo (Khoperskov et al. 2021) or accreted from some major merger event such as Gaia Enceladus sausage (Bignone et al. 2019; Buck 2020)).

Focusing on the Thin disk formation - this work's main target of investigation we would like to address the following questions. What are the key moments in the evolution of our Galaxy, and whether its most recent evolution has occurred in substantial isolation from the surrounding environment (e.g. Snaith et al. 2015b) or instead if external factors have strongly contributed to the creation of multiple stellar populations (e.g. Chiappini et al. 1997). The latest literature is rich in observational studies suggesting that the recent evolution of the Galaxy has been influenced by the interaction with dwarf galaxies (e.g Ruiz-Lara et al. 2020; Bland-Hawthorn &Tepper-García 2021; Lu et al. 2022b; Antoja et al. 2022; Gondoin 2023; Ratcliffe et al. 2023) merging with the Milky Way, such as the Gaia-Sausage-Enceladus (Belokurov et al. 2018; Helmi et al. 2018) or Sagittarius (Ibata et al. 1994). The same scenario is also supported by theoretical studies and simulations (e.g. Laporte et al. 2019; Wang et al. 2024).

Nowadays, different models have tiny differences between each other and we need a more detailed analysis of high-quality observational data to be able to distinguish them. We are lucky to have access to several high-resolution spectroscopic datasets such as HARPS, APOGEE and high-quality astrometry from Gaia DR3. Altogether, they offer us a great opportunity to study the Milky Way formation history in great detail. One of these important details is the age-metallicity relation. A recent study by Nissen et al. (2020) has found a bimodality in the age-metallicity diagram traced by nearby solar-twin stars. This result suggests the existence of two separated populations within the thin disk resulting from two episodes of accretion of gas onto the Galactic disk with a quenching of star formation in between around 5-6 Gyr ago. Although the study of Nissen et al. (2020) was based on only 72 stars and as Nissen et al. (2020) said it should be proven with a bigger dataset to be a solid statistical result. However, their results seem to agree with more recent studies based on APOGEE DR17 data[1] ((Jofré 2021; Anders et al. 2023)). Namely, Jofré (2021) has shown a clear discontinuity in the [C/N]-metallicity diagram of red clump stars in the solar neighborhood. Since for red clump stars the [C/N] abundance ratio can be considered a proxy of stellar ages, the two populations found by Jofré (2021) can be traced back to those of Nissen et al. (2020). Anders et al. (2023) have used chemical APOGEE abundances to derive ages of red-giant stars confirming the bimodality of the age-metallicity diagram hinted by Nissen et al. (2020) (see Fig. 8 in Anders et al. 2023) and Jofré (2021). The result however should not be surprising as their ages were mostly inferred by the C and N abundances, which are the same analyzed by Jofré (2021). However, the actual presence of these populations in the thin disk is still a matter of debate. In fact, several other studies show no signature of two populations (Xiang &Rix 2022; Lu et al. 2022b; Miglio et al. 2021). Interestingly, all of these studies use different

[1] https://www.sdss4.org/dr17/

age-determination methods, targets from different observations and cutoffs which are the crucial points on this issue (Sahlholdt et al. 2022; Queiroz et al. 2023).

According to the simple closed box model with instantaneous mixing of produced elements (Pagel 1997), one expects metallicity and abundances of other elements to increase smoothly with time. However, it was found that the chemical trends of stars with different ages at the same location in the Galaxy cross with each other. Important insights in this context were provided by Ratcliffe et al. (2023) based on APOGEE data and age estimations from Anders et al. (2023). The authors compute the birth radii of red giant branch stars based on the assumption of the presence of radial migration and use that information to study the chemical evolution at different locations across the Galactic disk. Chemical trends of the stars with different ages for the same birth radii are instead distributed smoothly which means that radial migration can explain the chemically mixed composition in the Galactic thin disk stars. However, they reported the presence of fluctuations in the metallicity- and [X/H]-gradient evolution, which they tentatively ascribe to the dilution in [Fe/H] from gas brought by the Gaia Sausage-Enceladus and Sagittarius mergers. Two of these features are observed at lookback times ∼4 and ∼6 Gyr. Altogether it produces a scenario of Milky Way formation with radial migration and accretion events playing an important role in the chemical composition of the thin disk.

In this work, we focus on the thin disk solar twins. Due to their similarity to the Sun, we can perform high-accuracy differential spectroscopic analysis. That makes them the perfect candidates to study chemical evolution in detail. We study the age-metallicity relation for the dataset of 485 stars with high-resolution spectroscopic observation. We study the main sources of misinterpretation of the data such as statistical and selection biases and different types of uncertainties. Also, we derive the birth radii for stars under investigation to study the ability of the radial migration model to explain observed chemical trends. Moreover, we are searching for signatures of the most massive mergers.

In Sec. 4.2 we explain how we obtained all different stellar properties. In Sec. 4.3 we talk about the method we used to study the age-metallicity relation and we present our results with a detailed analysis of all possible uncertainty sources. In Sec. 4.4 we study how the radial migration model together with the presence of major merger events can explain observational features. And we conclude with Sec. 4.5.

4.2 Data

In this work, we make use of two datasets of spectroscopic parameters and abundances of solar twins (i.e., effective temperature T_{eff} : $T_{eff,\odot} \pm 200$ K; surface gravity $logg$: $logg_\odot \pm 0.20$ dex; metallicity $[Fe/H]$: $[Fe/H]_\odot \pm 0.3$ dex; where $T_{eff,\odot} = 5771$ K, $logg_\odot = 4.44$ dex and $[Fe/H]_\odot = 0.0$ dex, Ayres et al. (2006)) with high-resolution high signal-to-noise spectroscopic observation to have a good number of stars for the statistic. The first dataset consists of HARPS-N spectra for 114 stars, which are fully reduced and analyzed in this work as described in the following paragraphs (Sec. 4.2.1). The outcomes of this spectroscopic analysis are the stellar parameters and chemical abundances. This dataset has been greatly expanded by the chemical abundances derived by Casali et al. (2020) for 371 solar-twin stars observed with the HARPS-S spectrograph. Ages and birth radii have been consistently derived in this work for all stars of the two datasets (Sec. 4.2.5, 4.2.6).

4.2.1 Spectroscopic analysis

Data sample and data reduction

To obtain high-quality spectra we used observations available in the archive of the HARPS-N spectrograph. This latter is a high-precision spectrograph onboard the Galileo National Telescope (TNG) in La Palma Island (Canary Islands, Spain). With HARPS-N we are able to obtain high-resolution (R=115,000) optical spectra with a broad wavelength coverage (378-691 nm).

In the archive IA2[2] we queried for stars with `CCF Mask` equal to G2 which should correspond to G-type stars. We obtained reduced spectra for 1118 stars and most of them had several exposures. Among those, we used only spectra with $S/N > 30px^{-1}$.

All spectra were normalized by IRAF[3] function `continuum` and Doppler-shifted by `dopcor` using spectral radial velocities derived by `crosscorrRV`[4] through cross-correlation with solar spectrum. Then, all exposures were stacked together by Python script that re-bins each spectrum to the common wavelengths without changing the resolution, computes the median of the pixels and applies 3σ clipping to the pixel values. During the analysis, all spectroscopic binaries were removed together with misclassified by solar-type stars based on cross-correlation analysis with respect to the Solar spectrum.

Additionally, we analyzed Solar spectra obtained through asteroid, planet and planet's satellites observations (i.e., Vesta, Venus, Europa, Ganymede). As it is detailed in the following paragraphs, the solar spectrum was essential to perform a line-by-line differential analysis of our stellar sample with respect to the Sun.

Stellar parameters and chemical abundances

The method of spectroscopic analysis applied in this work is the line-by-line differential analysis relative to the Solar spectrum, which is also the same method applied by Casali et al. (2020) to derive their chemical abundances. This method is perfectly suited for the analysis of solar-twin stars as it cancels out the impact of log gf parameters in the error balance and also reduces the impact of systematics in models and in the spectrum normalization. As a result, the line-by-line differential analysis lets us derive stellar parameters and chemical abundances with extremely high precision (Ramírez et al. (2014), Meléndez et al. (2014), Spina et al. (2016), Spina et al. (2018), Nissen et al. (2020), Casali et al. (2020)). In our analysis, we also adopted the same code and line-lists used by Casali et al. (2020). To derive chemical abundances of 25 chemical elements (C, Na, Mg, Al, Si, S, Ca, Sc, Ti, V, Cr, Mn, Co, Ni, Cu, Zn, Sr, Y, Zr, Ba, La, Ce, Nd, Sm, Eu) we used the master list of atomic transitions of Meléndez et al. (2014) that includes 98 lines of Fe I, 17 of Fe II, and 183 for the other elements, detectable in the HARPS spectral range ($3780 - 6910$ Å) and measured their equivalent widths (EW) with `Stellar diff`[5].

`Stellar diff` code allows the user to interactively select one or more spectral windows to create a mask around each studied line, that contains the measuring line and parts of the local continuum around it without any contamination from other lines. Choosing the continuum locally allows us to minimize uncertainties due to imperfect spectrum

[2] http://archives.ia2.inaf.it/tng/
[3] https://iraf-community.github.io/pyraf.html
[4] https://pyastronomy.readthedocs.io/en/latest/pyaslDoc/aslDoc/crosscorr.html
[5] https://github.com/andycasey/stellardiff

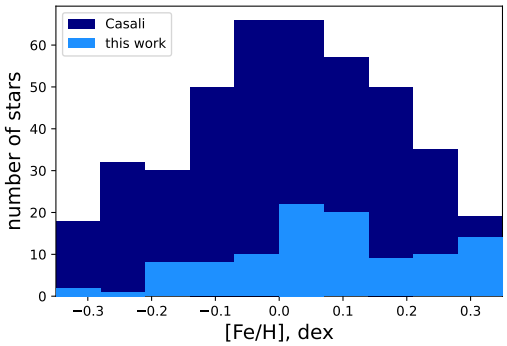

Figure 4.1: Metallicity distribution for the dataset analyzed in this work and for the dataset from Casali et al. (2020).

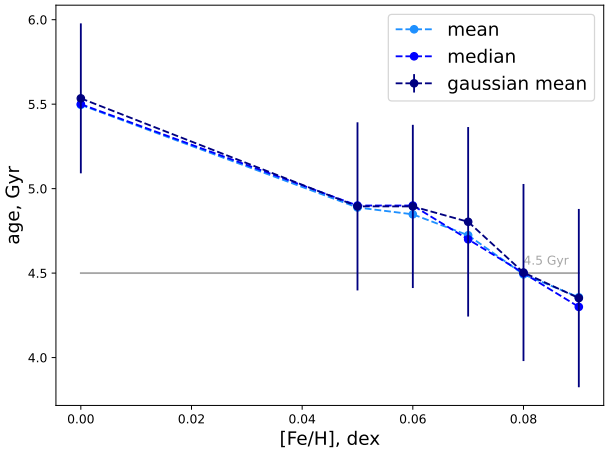

Figure 4.2: Age of the Sun calculated for different values of metallicity to calibrate isochrones for the influence of atomic diffusion at the solar age. *Light blue* represents mean values for the Sun' age, *blue* - median and *dark blue* - gaussian mean. *Grey line* is the most accurate estimate of the Sun's age Connelly et al. (2008); Amelin et al. (2010).

normalization and unresolved features in the continuum (Bedell et al. (2014)). The code fits each line of interest with a Gaussian profile and provides the EW and uncertainty. Additionally, `Stellar diff` is able to identify hot pixels and cosmic rays and remove them from the analysis.

To determine stellar parameters we used the `qoyllur-quipu (q2)`[6] code (Ramírez et al. (2014)). This code performs line-by-line differential analysis of EWs of the iron lines relative to the Sun measurements. The `q2` algorithm iteratively searches for three equilibria: extinction, ionization and the trend between the iron abundances and the reduced EW $log[EW/\lambda]$. Iterations start with the initial parameters (normal solar parameters) and produce a final set of parameters that satisfy all three equilibria. For the analysis we used Kurucz (ATLAS9) grid of model atmospheres (Castelli &Kurucz (2004)), the MOOG 2014 version (Sneden (1973)) and the following solar parameters: T_{eff} = 5771

[6] https://github.com/astroChasqui/q2

K, $logg$ = 4.44 dex, $[Fe/H]$ = 0.00 dex and ξ = 1.00 km/s (Ayres et al. (2006)). The uncertainty evaluation procedure is described in Epstein et al. (2010) and Bensby et al. (2014) where the relation between stellar parameters is taken into account. The typical internal uncertainty of the adopted methodology for each parameter, which is the average uncertainty of all stars, is $\sigma(T_{eff})$ = 9 K, $\sigma(logg)$ = 0.03 dex, $\sigma([Fe/H])$ = 0.007 dex and $\sigma(\xi)$ = 0.02 km/s. In Fig. 4.1 we present the metallicity distribution for the dataset analyzed in this work and for the dataset from Casali et al. (2020). We can see that both datasets are consistent with each other.

From stellar parameters and their uncertainties `q2` using appropriate atmospheric models derives chemical abundances for each 25 chemical elements. All abundances are scaled relatively to the Sun measurements on a line-to-line basis. Also, with `blends` driver in the MOOG code `q2` takes into account the hyper-fine splitting effects in Y, Ba and Eu. The HFS line list is adopted from Meléndez et al. (2014). However, this approach still leaves the possibility for additional uncertainty. Ideally, each line should be fully modeled and the observed shape should be compared with the modeled one (Bensby et al. 2005; Feltzing et al. 2007). Though, our analysis is robust enough for stars with close to Sun stellar parameters. Finally, `q2` derives uncertainties for every abundance [X/H] by the quadratic sum of the line-by-line scatter due to EW measurements (standard error) and errors of the atmospheric parameters. For the chemical elements with just one line measurement (Sr, Eu) as a standard error, we took the uncertainty of the EW measurement with `Stellar diff`.

Comparison of two datasets

Spectra for the dataset of solar twins analyzed in this work (HARPS-N) and dataset from Casali et al. (2020) (HARPS-S) were acquired by spectrographs with similar characteristics. Also, the same spectral analysis was applied to both these datasets. However, there may be still some small systematics in abundance determinations of the two datasets due to minor differences between the instruments.

There are 27 stars in common between Casali et al. (2020) and our dataset. That allows us to compare the precision and accuracy of abundances and stellar parameters derived by us and Casali et al. (2020). To do that we performed a linear regression ($y = kx + b$) in $[X/H]_{this\ work}$ vs. $[X/H]_{this\ work} - [X/H]_{Casali}$ space. As a result, for most of the chemical elements we do not see the correlation between the abundance difference and the abundance value derived in this work (Tab. 4.1, the slope consistent with zero within 2 sigmas or zero (Ca, Na)). We only see a constant systematic shift between Casali et al. (2020) and our sample abundances. Only few elements show a slightly increasing difference between the two datasets with increasing abundance value (Tab. 4.1: Mg, Sc, Zn, V) but they are only 20% of the whole amount of elements. Therefore, we only applied the shift correction for Casali et al. (2020) data to bring all abundances to the same point (Tab. 4.1). This correction was computed as a median shift between these two abundances for each element.

4.2.2 Distance determination

Distance is one of the most important parameters in dynamics studies. Plotnikova et al. (2022) showed that, for the bright stars in the solar vicinity, the directly inverted Gaia EDR3 parallaxes are the best distance estimation method. Since most of the stars under

element	k	Δk	b	Δb	shift
CI	0.000	0.025	0.044	0.009	0.059
NaI	0.000	0.029	0.019	0.005	0.029
MgI	0.124	0.051	0.043	0.007	0.067
AlI	0.012	0.039	0.015	0.002	0.042
SiI	0.023	0.034	0.023	0.004	0.034
SI	0.033	0.035	0.045	0.010	0.031
CaI	0.045	0.034	0.029	0.005	0.035
ScI	0.081	0.046	0.032	0.008	0.060
TiI	0.030	0.030	0.024	0.004	0.031
VI	0.061	0.034	0.031	0.007	0.024
CrI	0.012	0.042	0.029	0.005	0.039
MnI	-0.026	0.027	0.030	0.006	0.027
CoI	0.046	0.040	0.034	0.007	0.033
NiI	0.005	0.030	0.021	0.005	0.027
CuI	-0.034	0.041	0.046	0.009	0.041
ZnI	0.064	0.040	0.020	0.005	0.038
SrI	0.007	0.001	0.009	0.002	0.001
ScII	0.022	0.044	0.034	0.007	0.042
TiII	0.041	0.042	0.030	0.005	0.041
CrII	0.011	0.033	0.021	0.004	0.029

Table 4.1: Comparison of abundances derived in this work and abundances derived by Casali et al. (2020) for the 27 stars in the overlap.

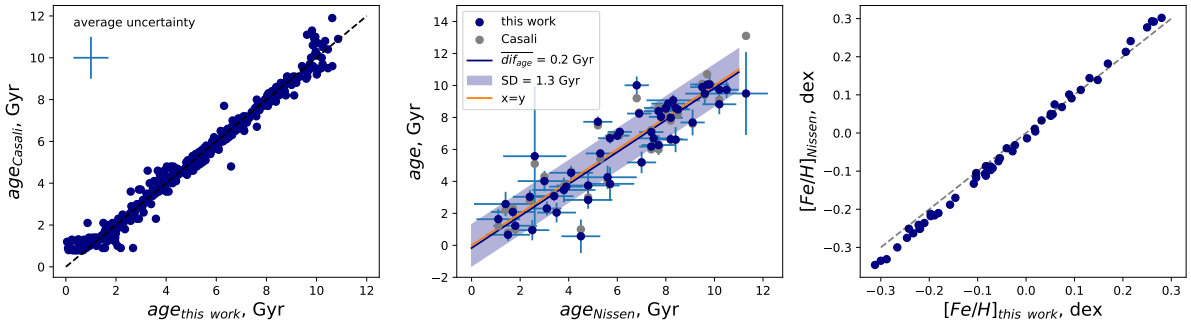

Figure 4.3: *Left*: comparison of age derived in this work and by Casali et al. (2020). *Middle*: comparison of age derived in this work and by Nissen et al. (2020) (*blue circles*) its mean difference ($\overline{dif_{age}}$) and standart deviation (SD); comparison of age derived by Casali et al. (2020) and by Nissen et al. (2020) (*grey circles*). *Right*: comparison of metallicity derived in this work and by Nissen et al. (2020).

Data product or source type	Typical uncertainty		
	G < 15	G = 17	G = 20
Five-parameter astrometry			
position, mas	0.01 - 0.02	0.05	0.4
parallax, mas	0.02 - 0.03	0.07	0.5
proper motion, mas yr^{-1}	0.02 - 0.03	0.07	0.5
Six-parameter astrometry			
position, mas	0.02 - 0.03	0.08	0.4
parallax, mas	0.02 - 0.04	0.1	0.5
proper motion, mas yr^{-1}	0.02 - 0.04	0.1	0.6

Table 4.2: Uncertainties of Gaia Early Data Release 3 astrometry Gaia Collaboration (2021)

consideration are bright and located inside 200 pc around the Sun for distance determination we used only Gaia EDR3 parallaxes (Gaia Collaboration (2021)).

4.2.3 Astrometric parameters

Intending to calculate orbits and orbital parameters, we extracted coordinates, and proper motion components from the Gaia DR3 archive (Gaia Collaboration et al. 2022b). Uncertainties for astrometric parameters are shown in Tab.4.2. Radial velocities were obtained from the spectroscopic analysis. Position and velocity of the stars in the Equatorial Coordinates were transformed to Galactocentric coordinates by `astropy`[7] python package.

4.2.4 Kinematics

We obtained orbits and orbital parameters for all stars in the dataset by numerical calculation and adopting a model of Galactic axisymmetric potential.

We corrected the velocities of the stars by the velocity of the Sun with respect to the Galactic center which is computed independently from the velocity of the local standard of rest (Reid &Brunthaler 2004; GRAVITY Collaboration et al. 2018; Drimmel &Poggio 2018):

$$v_{R\odot} = -12.9 \pm 3.0 \text{ km s}^{-1} \tag{4.1}$$

$$v_{\phi\odot} = 245.6 \pm 1.4 \text{ km s}^{-1} \tag{4.2}$$

$$v_{Z\odot} = 7.78 \pm 0.09 \text{ km s}^{-1} \tag{4.3}$$

where the distance between the Galactic center and the Sun is $R_0 = 8.122 \pm 0.033$ kpc (GRAVITY Collaboration et al. (2018)).

We used the McMillan (2017) Galactic potential without bar implementation in `galpy`[8] (Bovy 2015) to calculate orbits and orbital parameters such as the total energy (E_n), eccentricity (e), apo-center (R_{apo}), peri-center (R_{peri}), guiding radius (R_{guide}), angular

[7] https://docs.astropy.org/en/stable/_modules/astropy/coordinates/builtin_frames/galactocentric.htmlastropy

[8] http://github.com/jobovy/galpy

momentum along the z-axis (L_z) and velocity components in different directions (v_r, v_R, v_ϕ, v_z).

4.2.5 Age determination

We derived ages using the isochrone fitting technique on the Kiel diagram. To obtain ages and their uncertainties we made use of the algorithm developed by Plotnikova et al. (2022). Namely, the parameters for each star were randomly independently selected 10,000 times from a Gaussian distribution with mean as the parameter value and sigma as its uncertainty. For each selected set of parameters (out of 10,000), an age was computed. Afterward, the obtained age distribution is fitted with the Gaussian distribution, as a result, we take the mean as the age estimation and the sigma as the age uncertainty. The age fitting was carried out using the Padova isochrones PARSEC[9] with the steps: $\Delta age = 0.1$ Gyr, $\Delta[Fe/H] = 0.05$ dex; and for very young stars (initial guessed age is smaller than 1 Gyr) we repeated the algorithm with the steps: $\Delta age = 0.01$ Gyr, $\Delta[Fe/H] = 0.05$ dex. Since we have effective temperature and surface gravity from high-precision spectroscopic analysis, we derived ages with a median uncertainty of 0.7 Gyr. It is also worth mentioning that it is necessary to calibrate these ages as a function of metallicity to take into account the influence of atomic diffusion at the solar age (Meléndez et al. 2012; Dotter et al. 2017) and to obtain the last most accurate estimate for the age of the Sun (Connelly et al. 2008; Amelin et al. 2010). Therefore, we computed the age of the Sun for six different values of metallicity ([Fe/H]): 0.00, 0.05, 0.06, 0.07, 0.08, 0.09 dex. As we can see in Fig.4.2 metallicity equal 0.08 dex shows the best agreement with the Connelly et al. (2008) and Amelin et al. (2010) Solar age (4.5 Gyr). Therefore, we applied a 0.08 dex shift as a metallicity calibration.

It is also worth mentioning that it is necessary that the isochrones are calibrated by the metallicity correction (Meléndez et al. 2012) to reproduce the last most accurate estimate for the age of the Sun = 4.5 Gyr (Connelly et al. 2008; Amelin et al. 2010). One of the possible reasons can be the influence of atomic diffusion at the solar age (Dotter et al. 2017) in a different way that PARSEC isochrones are taking it into account. Therefore, we computed the age of the Sun for six different values of metallicity ([Fe/H]): 0.00, 0.05, 0.06, 0.07, 0.08, 0.09 dex. As we can see in Fig.4.2 metallicity equal 0.08 dex shows the best agreement with the Connelly et al. (2008) and Amelin et al. (2010) Solar age (4.5 Gyr). Therefore, we applied a 0.08 dex shift as a metallicity calibration.

To check the accuracy of determined ages we compared our results with ages from Casali et al. (2020) for 371 stars we have in common and ages from Nissen et al. (2020) for 52 stars.

Figure 4.3-*left* shows an excellent agreement between our age determinations and those from Casali et al. (2020). This is expected since both studies have used a similar method of analysis. Namely, both studies derived ages by isochrone fitting technique in surface gravity versus effective temperature space. Also, both studies accounted for the atomic diffusion at the solar age.

Regarding the comparison between our age determinations to those from Nissen et al. (2020) it is worth mentioning that in both cases ages were derived through isochrone fitting techniques, but in different parameters spaces. Namely, Nissen et al. (2020) used the T_{eff} vs. luminosity (L) space, while this work used the T_{eff} vs. $logg$). In Fig. 4.3, *middle* the

[9] http://stev.oapd.inaf.it/cmd

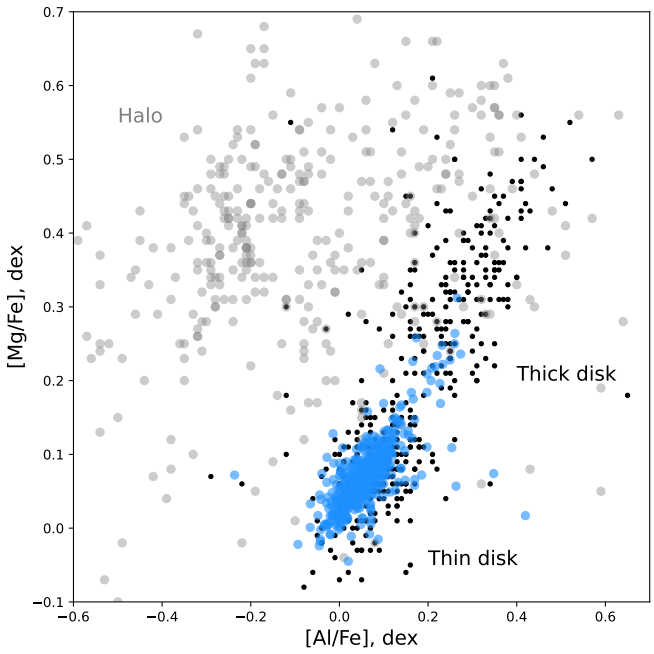

Figure 4.4: Al-Mg correlation. The background: disk stars (*black dotes*, Fulbright (2000), Reddy et al. (2003), Simmerer (2004), Reddy et al. (2006), François et al. (2007), Johnson et al. (2012), Johnson et al. (2014)), halo stars (*grey points*, Yong et al. (2013)), Roederer et al. (2014), dataset this work (*light blue circles*).

average uncertainty for both datasets is equal to 0.7 Gyr. The mean difference (dif_{age}) between the two measurements for the overlapping stars and its standard deviation (direct error) are:

$$\overline{dif_{age}} = \frac{\Sigma_{i=0}^{N}(age^{i}_{Nissen} - age^{i}_{this\ work})}{N} = 0.17 \pm 1.30 \text{ Gyr} \tag{4.4}$$

and the indirect error of the average difference is:

$$\Delta\overline{dif_{age}} = \sqrt{\Delta\overline{age_{Nissen}}^2 + \Delta\overline{age_{this\ work}}^2} =$$

$$= \sqrt{0.7^2 + 0.7^2} = 0.9 \text{ Gyr} \tag{4.5}$$

The fact that direct (1.3 Gyr) and indirect (0.9 Gyr) errors are close to each other means that ages from two different methods are in good agreement. Additionally, ages from Casali et al. (2020) for these 52 stars show the same correlation as values from this work (Fig. 4.6, *middle*).

Both tests with Casali et al. (2020) and Nissen et al. (2020) ages showed that our age determination method is accurate and gives the same precision as in Casali et al. (2020) and in Nissen et al. (2020).

4.2.6 Determination of the R_{birth}

Chemical abundances contain information regarding the birth environment of the star (Freeman &Bland-Hawthorn 2002; Ratcliffe et al. 2022), and are representative of when

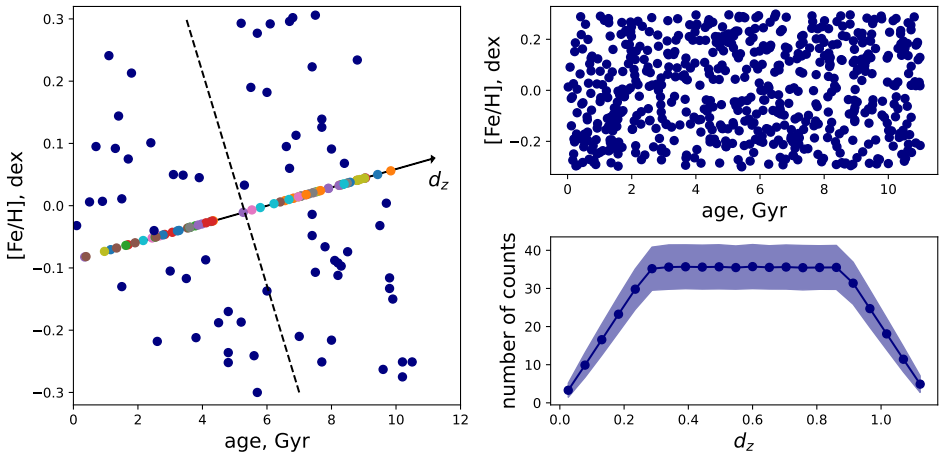

Figure 4.5: *Left*: age-metallicity map of Nissen's data (*blue dots*) with the division line for two populations (*black dashed line*) and with d_z parameter axes (*black solid line*). The solar-twins projected across the d_z axis (*color points*). *Upper right*: randomly distributed 600 stars. *Lower right*: projection of the data from the upper right age-metallicity map to the d_z axis.

(*age*) and where (R_{birth}) the star is born (e.g. Minchev et al. 2018; Frankel et al. 2018; Ness et al. 2019; Lu et al. 2022b). Since we have age, metallicity we can derive the birth radius using the method described in Lu et al. (2022b) and Ratcliffe et al. (2023), which has been shown to work in galaxies with stronger bars, like the Milky Way (Ratcliffe et al. (2024)). We assume that the star-forming gas in the Milky Way is azimuthally chemically homogeneous (observation: Deharveng et al. (2000), Esteban et al. (2017), Arellano-Córdova et al. (2021); simulations: Vincenzo &Kobayashi (2018), Lu et al. (2022a)) and that the birth metallicity gradient is always linear in radius (Arellano-Córdova et al. 2021; Esteban et al. 2022). Therefore, for any lookback time (τ), we can write metallicity ($[Fe/H](R,\tau)$) as a function of the metallicity gradient at that time ($\nabla[Fe/H](\tau)$), birth radius and the metallicity at the Galactic center ($[Fe/H](0,\tau)$):

$$[Fe/H](R_{birth},\tau) = \nabla[Fe/H](\tau) * R_{birth} + [Fe/H](0,\tau) \tag{4.6}$$

Rearranging the Equ. 4.6 we can estimate the birth radius as a function of age and metallicity:

$$R_{birth}(age,[Fe/H]) = \frac{[Fe/H] - [Fe/H](0,\tau)}{\nabla[Fe/H](\tau)} \tag{4.7}$$

The metallicity at the Galactic center and the metallicity gradient as a function of lookback time were taken from Ratcliffe et al. (2023).

4.2.7 Origin

To derive the origin of the dataset under investigation we used the Al-Mg correlation map that shows one of the best separations between Halo, Thin disk and Thick disk stars. As we can see in Fig. 4.4 almost all of our stars are lying in the location of the Thin disk stars and also taking into account that their stellar parameters are Sun-like we consider them to be a good sample of Thin disk stars.

Criteria	range
CCF mask	G2
spectroscopic binaries	removed
misclassified by solar type stars	removed
signal-to-noise, S/N	$> 30px^{-1}$
effective temperature, T_{eff}	$T_{eff,\odot} \pm 200$ K
surface gravity, logg	$logg_{\odot} \pm 0.2$ dex
metallicity, [Fe/H]	-0.3 - 0.3 dex
age	0 - 12 Gyr

Table 4.3: All cutoffs applied for the dataset under investigation. ($T_{eff,\odot} = 5771$ K, $logg_{\odot} = 4.44$ dex, Ayres et al. (2006))

4.3 Age-metallicity relation

4.3.1 Method

To study the presence of the two populations found by Nissen et al. (2020) we use the following method. First, we determine the axis d_z in the age-metallicity plot that maximizes the separation between the two populations. That axis is determined through the Linear Discriminant Analysis[10] algorithm trained over the ages and metallicities used by Nissen et al. (2020) (see their Fig. 3). Then, we rescale the data (0.6 dex in metallicity to 12 Gyr in age) to let age and metallicity affect the separation equally. Finally, we project all data points under investigation on d_z and we study the distribution of stars across that new axis. This procedure is illustrated in Fig. 4.5-*left panel*, where we show the age-metallicity diagram with the 72 solar-twins by Nissen et al. (2020), the d_z axis, the correspondent division line for the two populations, and the solar-twins projected across the d_z axis.

While studying the distribution of stars across d_z one should also consider the geometrical effects of that projection due to the edges of the dataset under consideration. As an illustrative example, the distribution of homogeneously distributed stars inside the same age and metallicity range covered by Nissen et al. (2020) sample (age: 0 - 12 Gyr, [Fe/H]: -0.3 - 0.3 dex) is shown in Fig. 4.5, *right top* (see all cutoffs in Tab. 4.3). In Fig. 4.5, *right bottom* the shape of the d_z parameter distribution is not linear because of the geometry of the dataset. Instead, the distribution has two decreasing wings on the edges. All that occurs because the dataset lies in a rectangular space (i.e., there is no apparent correlation between ages and [Fe/H] abundances) and it is projected to the axis that is non-parallel to one of the sides.

Once we have determined the distribution of stars across the d_z axis, we are interested in deriving the uncertainties in the star counting at each bin of the d_z parameter. There are two types of uncertainties:

1. Measurement uncertainty associated with age and metallicity uncertainties of each star. We randomly and independently selected 1000 times metallicity and age values from the Gaussian distribution with the mean as the measured value and with sigma as its uncertainty.

[10] sklearn.discriminant_analysis.LinearDiscriminantAnalysis

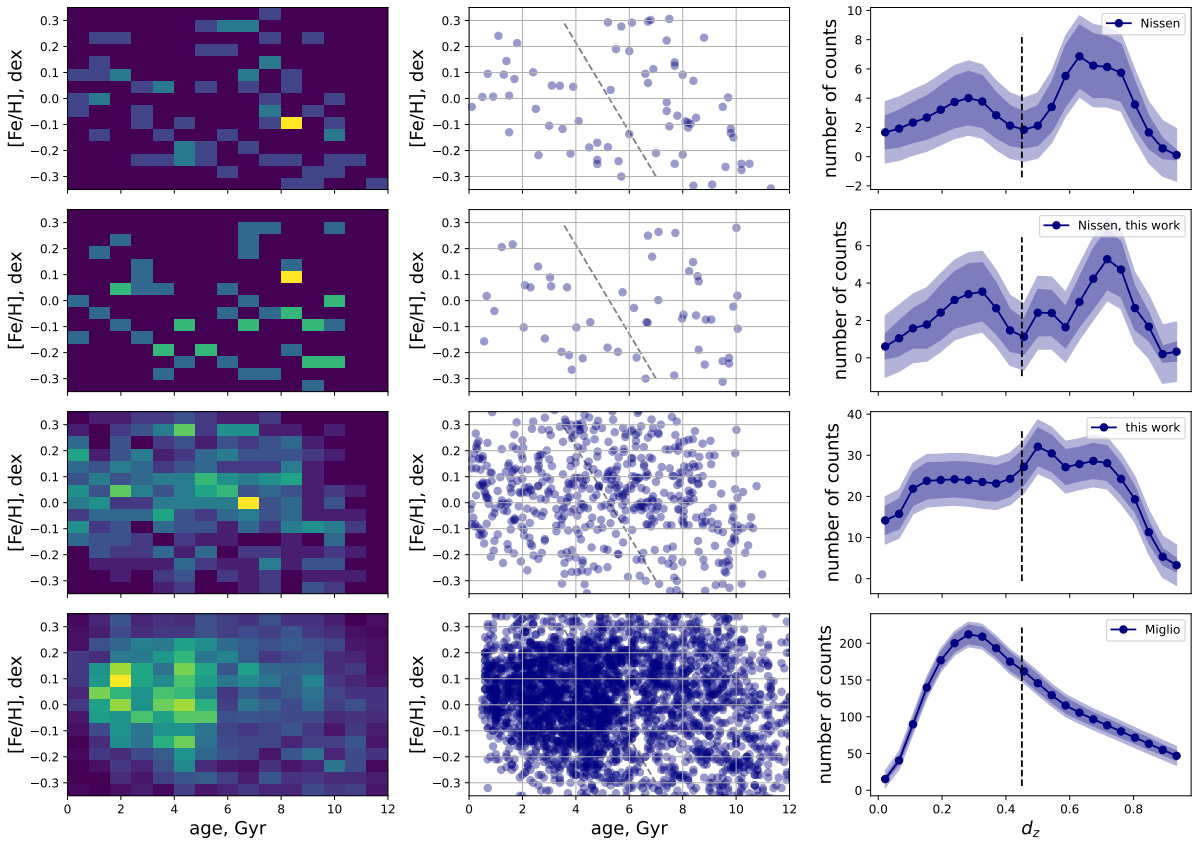

Figure 4.6: Age-metallicity relation for three different datasets: [1] Nissen's dataset (72 stars, *top row*), [2] stars that we analyzed from Nissen's dataset (52 stars, *second row*), [3] dataset under investigation in this work (485 stars, *third row*), [4] dataset from Miglio et al. (2021) (2785 stars, *bottom row*). The right column represents the d_z separation parameter (Sec. 4.3.1) where the vertical dashed line represents the location of the Nissen's data drop, the dark blue region is the measurement uncertainty, and the light blue region is the quadratic sum of measurement and statistical uncertainty.

2. Statistical uncertainty associated with bin counts:

$$\sqrt{\frac{1}{n_{bins}}(1-\frac{1}{n_{bins}}) * n_{stars}} \tag{4.8}$$

where $\frac{1}{n_{bins}}$ is the probability of the star falling into a chosen bin in d_z and n_{stars} is a number of stars in the dataset.

The method described above rigorously considers all the sources of uncertainty associated with the distribution of stars across the d_z axis. Through this approach, we can establish whether or not there is significant evidence of the two populations identified by eye by Nissen et al. (2020). In Section 4.3.2 we apply this method to different datasets, including the one analyzed by Nissen et al. (2020) and the much larger dataset provided in this study.

4.3.2 Results

Now we apply the method explained in Sec. 4.3.1 to study the presence of separation in the age-metallicity diagram pointed out by Nissen et al. (2020). It is important to mention that their dataset had only 72 stars and Nissen et al. (2020) claim their result should be checked with a bigger dataset. As our dataset includes 485 stars, it offers the possibility to further investigate this area in age-metallicity relation. In Fig. 4.6 we show the age-metallicity relations for four different datasets: [1] Nissen's dataset (72 stars, *top row*), [2] stars that are in common between Nissen's and our dataset (52 stars, *second row*), [3] dataset under investigation in this work (485 stars, *third row*), [4] dataset from Miglio et al. (2021) (2785 stars, *bottom row* typical age error - 1 Gyr).

Firstly, we analyzed Nissen's dataset with the method described in Sec. 4.3.1. We take into account the various sources of uncertainty (Sec. 4.3.1) and we can see that the analysis shows that separation between two populations is not relevant. In fact, the drop in the star's distribution across the d_z axis is less than 1-σ uncertainty (Fig. 4.6, *top row*). All that suggests that the separation found by Nissen et al. (2020) is due to a small number of statistics.

Our dataset contains 52 stars in common with Nissen et al. (2020), and as one can see in Fig. 4.3, *right* the metallicity measurements are in perfect agreement with Nissen et al. (2020). Also, as we discussed in Sec. 4.2.5, ages derived in this work and by Nissen et al. (2020) have the same precision and are in good agreement with each other. By applying the method for the overlapping 52 stars with age and metallicity derived by us we still can see the same pattern as in Nissen et al. (2020) data but taking into account all the uncertainties the separation between two populations is not as evident as in Nissen et al. (2020) data (Fig. 4.6, *second row*). Both analyses with different age and metallicity determination show the same pattern but we can conclude that taking into account uncertainties Nissen et al. (2020) dataset does not contain enough stars to support a strong claim about the presence of two populations.

Thirdly, we analyzed the whole sample from this work. In Fig. 4.6, *third row* we do not see any signature of the two populations. The resulting distribution is in good agreement within the uncertainties with the model of homogeneously distributed stars in the age-metallicity map (Fig. 4.5, *bottom right*). Moreover, we do not detect any double structure in the age-metallicity plot (Fig. 4.6, *third row middle*) and in the age-metallicity density map (Fig. 4.6, *third row left*).

In the end, we also analyzed data from Miglio et al. (2021) adopting our method. Their dataset is composed of red giant and red clump stars with APOGEE metallicity measurements and asteroseismic high-accuracy ages (average uncertainty: 1 Gyr). We cut their dataset in metallicity to match our range of study ($-0.3 < [Fe/H] < 0.3dex$). In Fig. 4.6, *bottom right* we detect a single population centered around 3 Gyr with smoothly decreasing density towards older ages. This effect can be explained by the fact that selected stars are from the red giant branch and red clump region. Stars spend less time in the red giant branch and the red clump phases than in the main sequence. Therefore, these two regions are mainly populated by stars with a specific narrow mass range hence ages. However, for the main sequence, this range of masses is bigger, and as a result, we have a more horizontal distribution in age. That is why we do not see the homogeneous distribution across the d_z axis as we have seen for our dataset solar-twin stars. However, for Miglio et al. (2021) dataset we also do not detect the presence of the two populations found by Nissen et al. (2020).

Unaccounted age uncertainties

One may still argue that we have unaccounted age uncertainties that blur over the separation. Therefore, we performed a test to estimate the value of unaccounted uncertainty we need to blur over the separation between two populations similar to those of Nissen et al. (2020). To do that, we simulated the dataset of 485 stars (same number as the dataset under investigation) with two separated populations in the exact locations as in Nissen et al. (2020) (Fig. 4.7, *first row*). We took three main points from younger ((age$_{[Gyr]}$, [Fe/H]$_{[dex]}$): (7, 0.2), (8, 0), (9, -0.2)) and from older ((age$_{[Gyr]}$, [Fe/H]$_{[dex]}$): (1.5, 0.1), (3, -0.1), (5, -0.2)) populations and randomly created blobs with Gaussian distribution with sigma equal 0.7 Gyr for age and 0.1 dex for metallicity (Fig. 4.7, *top left*). For measurement uncertainties, we used 0.06 dex for metallicity and 0.7 Gyr for age the average uncertainties for our dataset. As a result, we see in Fig. 4.7, *top right* the drop in density distribution has 2σ significance. Then for each artificial star, we randomly selected an age value inside the Gaussian distribution with the sigma equal unaccounted error. This approach simulates the effect of blurring due to unaccounted error in age. As a result, in Fig. 4.7 we can see that the drop due to the presence of two populations disappears when an unaccounted error is equal to 1.7 Gyr. This value should be understood as an eventual unknown uncertainty that we have to have in addition to 0.7 Gyr age determination uncertainty to be able to explain the absence of two populations through the blurring effect. This value is 2.5 times bigger than the age determination uncertainty and also 2 times more than the direct error of age dispersion between our ages and the ones from Nissen et al. (2020) (Sec. 4.2.5). It means that it is very unlikely that we have such a huge unaccounted error and, as a result, it is also unlikely that we have a significant blurring effect.

Selection bias

While studying the Milky Way formation and evolution it is very important to pay attention to the selection function effects. Cutoffs in color-magnitude diagrams, distance limits and other selection criteria misrepresent the real picture of our Galaxy. As we already discussed, for the Miglio et al. (2021) dataset selecting stars from the red giant branch/ red clump region (fast evolutionary phase) creates the peak in age around 3 Gyr. Feuillet et al. (2018), however, found a double-peaked structure due to selection bias. Also, as shown in Sahlholdt et al. (2022) distance larger than 600 pc creates a bias in the age-metallicity map changing the initially homogeneous distribution to the distribution with several features. As a result, the selection function plays an important role in the study of the Milky Way formation and evolution.

In our work, we selected stars from the main sequence/turn-off point as this phase is much slower compared to the red giant branch/red clump phase and therefore our data should be much less contorted. Also, most of our stars are located inside a 200 pc bubble which is far below the limit found by Sahlholdt et al. (2022). Therefore we can conclude that based on our knowledge our data is not affected by the selection bias and represents the original age-metallicity relation in the Solar neighborhood.

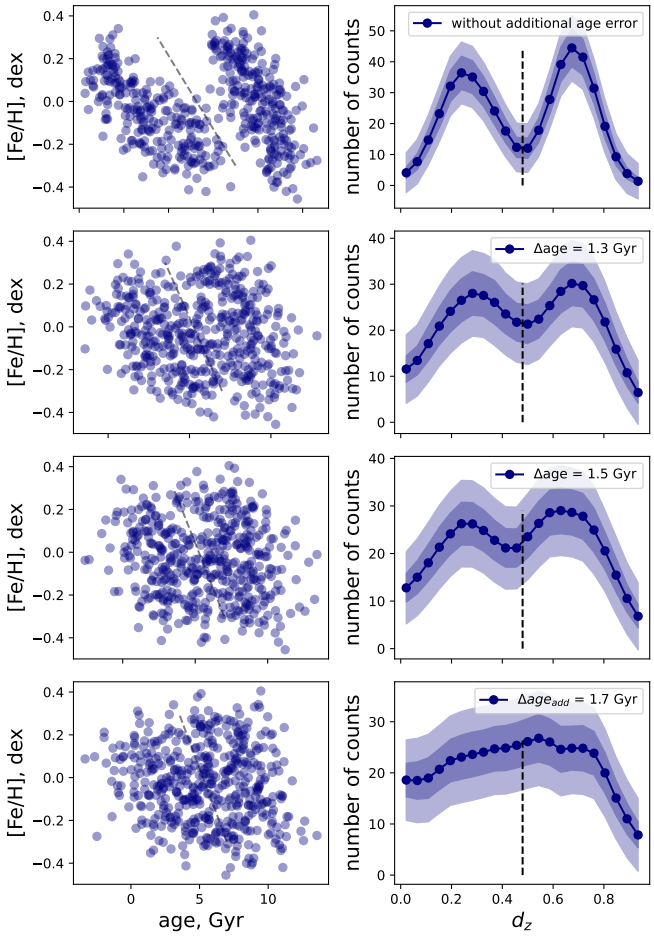

Figure 4.7: Test for the ability of unaccounted uncertainties in age determination method to vanish the presence of two populations. In each line, the results of distinguishing two populations are presented with unaccounted errors: 0.0, 1.3, 1.5, 1.7 Gyr from top to bottom. We need at least 1.7 Gyr of additional unaccounted error in age to eliminate any signature of double populations.

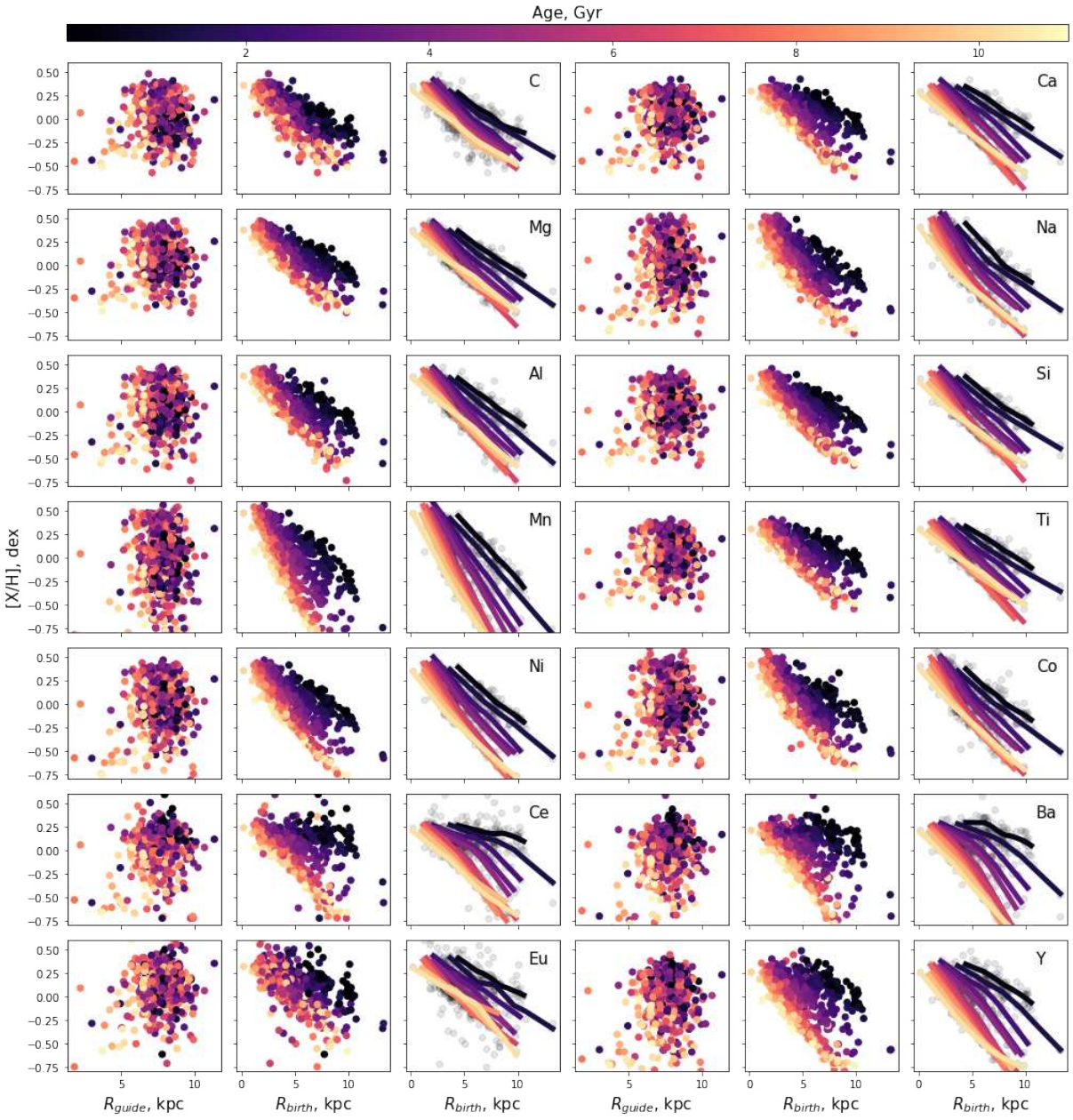

Figure 4.8: Chemical trends for 14 elements with guiding and birth radii (R_{guide}, R_{birth}) color-coded by age. In the third and sixth columns lines of trend were obtained by locally weighted scatterplot smoothing (`LOWESS`).

4.3.3 Age-metallicity relation summary

To sum up, the separation seen for stars selected in Nissen et al. (2020) dataset is not significant if we consider all sources of uncertainty. In fact, the drop in star counts due to separation is less than 1σ. An increased number of stars with the same high-quality high signal-to-noise metallicity measurements coupled with accurate age values also do not show any signature of the separation. This seems to indicate that the presence of two populations in Nissen et al. (2020) study is probably due to a sort of selection bias coupled with very low statistics. The comparison of this result with other studies, as we discussed in the Sec. 4.3.1, shows that only in the case of adopting ages from the APOGEE based on C and N dependencies (Jofré 2021) the presence of two populations emerges. All the other studies do not show it (Xiang &Rix (2022), studies based on solar twins: Spina et al. (2016), Spina et al. (2018), Bedell et al. (2018),Casali et al. (2020)). Also, the study of Miglio et al. (2021) that uses APOGEE stellar parameters and abundances but Kepler asteroseismic ages do not show any separation (Fig. 4.6, *bottom row*). This implies that the age determination method plays an important role and APOGEE ages may have a sort of bias that creates a non-linear distribution in age. For example, Anders et al. (2023) showed that the residuals between their ages and those derived with other methods are not linear, but display an oscillation pattern. That could cause a non-linear distribution of stars in the age-metallicity map. This hypothesis should be checked with a deeper study.

4.4 Chemical trends

Chemical abundances, ages, metallicity, guiding radius, and birth radius altogether allow one to trace the chemical evolution of the Milky Way disk. Fig. 4.8 illustrates chemical trends vs. birth/guiding radius color-coded with age for 14 chemical elements. As for the guiding radius, we notice that stars of different ages are well mixed and this high dispersion makes it difficult to trace the chemical evolution with age. On the other hand, exploiting the birth radius trends, we see that stars are separated from each other. This implies that radial migration (the basis of the chemical evolution model in the birth radius determination method (Minchev et al. 2018; Lu et al. 2022b; Ratcliffe et al. 2023)) explains the basic age-chemistry dependencies in the disk region around the Sun. However, we notice the presence of knees and slight overlap in the age ranges 4 - 6 Gyr and 8 - 12 Gyr (Fig. 4.8). Therefore, some other mechanism should be at work in tandem with radial migration. The most plausible mechanism is surely the cumulative effect of the accretion that the Galaxy experienced since its early assembly and that must have an impact on the disk evolution in particular. This has been pointed out in several recent observational studies which for instance illustrate the role of the Gaia-Enceladus/Sausage (GES) accretion event in altering the chemical evolution of the Milky Way disk in the period from 8 to 11 Gyr (Ruiz-Lara et al. 2020; Gondoin 2023; Lu et al. 2022b; Ratcliffe et al. 2023; Anders et al. 2023, to make a few examples). Such effects have been as well reproduced by numerical simulations (Laporte et al. 2019; Belokurov et al. 2018; Helmi et al. 2018; Buck et al. 2023; Wang et al. 2024). The period in which GES was effective is depicted in Fig. 4.9, *orange region*.

Besides, several studies demonstrated the significant impact from the Sagittarius (Sgr) pericentric passages (first: 4 - 6.5 Gyr; second: 1.5 - 2.2 Gyr; third: 0.4 - 1 Gyr, Fig.

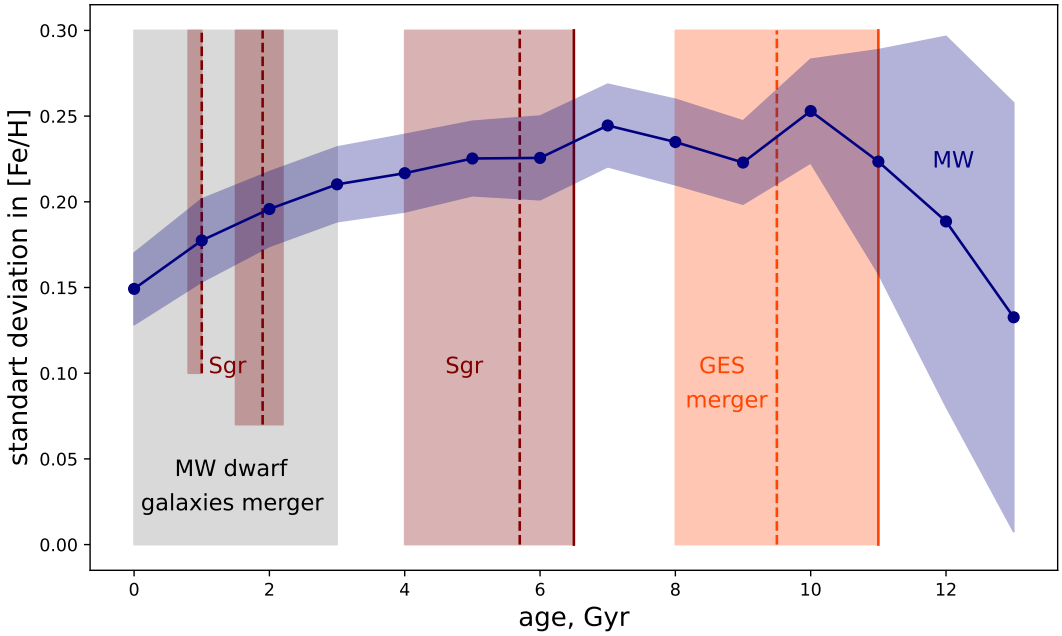

Figure 4.9: Metallicity standard deviation vs. age trend of the stars under investigation (*blue line* - main trend, *blue region* - measurement uncertainty Sec. 4.3.1). *Orange*: Gaia-Enceladus/Sausage accretion event (observations: Ruiz-Lara et al. (2020); Gondoin (2023); Lu et al. (2022b); Ratcliffe et al. (2023); Anders et al. (2023), numerical simulations: Laporte et al. (2019); Belokurov et al. (2018); Helmi et al. (2018); Buck et al. (2023); Wang et al. (2024)); *red*: Sagittarius (Ruiz-Lara et al. 2020); *grey*: mergers of the Milky Way dwarf galaxies (Wang et al. 2024). Solid vertical lines show the beginning of the merger, and dashed vertical lines show the pick of star formation corresponding to a particular accretion event.

4.9, *red region*, Ruiz-Lara et al. (2020)) in the history of the Milky Way disk formation around the Sun. And, finally, Wang et al. (2024) showed that not only the Sagittarius (Sgr) passage affected the Milky Way past 3 Gyr but also other passages of Milky Way dwarf galaxies (Fig. 4.9, *grey region*). As well, in Fig. 4.9 we present the metallicity dispersion vs. age plot for our dataset. One can see the fluctuation corresponding to GES merger in the range from 8 to 10 Gyr. Additionally, we notice a small fluctuation corresponding to the Sagittarius first pericentric passage around 5 to 6.5 Gyr, but this cannot be considered significant due to the uncertainty.

4.5 Conclusions

In this study, we analyzed 114 solar twins for which we performed a spectroscopic analysis of high-resolution spectra from HARPS-N. Also, we analyzed a dataset from Casali et al. (2020) with spectroscopic analysis from Casali et al. (2020) (371 stars). For both datasets, we derived ages with the isochrone fitting technique in the effective temperature vs logarithm of surface gravity space with a metallicity correction for the atomic diffusion at the solar age. As a result, we obtained high precision ages and chemical abundances that allowed us to study the age-metallicity relation (AMR) for solar twins around the Sun ([Fe/H]: -0.3 - 0.3 dex). We used a new parameter (d_z, Sec. 4.3.1) to test the AMR separation into two groups for solar twins in the solar vicinity. In the process, we took into account all possible sources of errors and did not detect a separation (Fig. 4.6). This result is in agreement with Miglio et al. (2021), Xiang &Rix (2022), Lu et al. (2022b). As for Nissen et al. (2020) the separation was caused by the statistical bias. In the literature, there are studies that reached the opposite result (Jofré 2021; Ratcliffe et al. 2023). There are two possible reasons why these two studies show the separation. First of all, they employed ages obtained from the use of C and N abundances. This indicates that age determination is one of the crucial aspects of studying these chemical trends. Another extremely important parameter that always should be tested while studying data that has cutoffs is the selection bias. Cutoffs in distance, magnitude, metallicity, etc produce features that lead to misinterpretation of the data. And this topic should be widely explored.

Also, we studied the dependence of chemical abundance with guiding and birth radii and age (Fig. 4.8). We see that mixed star populations for the guiding radius transform in well-separated trends for the birth radius. It means, that radial migration that lies in the basis of the birth radii determination explains well the star's chemical distribution around the Sun. But some effects like the presence of knees for some age trends of some elements or overlap for some age trends lead us to the conclusion that radial migration alone does not explain all the features in the Milky Way formation history.

Several authors already showed that GES merger and Sagittarius pericentric passages as well as other passages and accretions of dwarf galaxies affected the Milky Way evolution. In Fig. 4.9 we also detect fluctuations in the standard deviation of metallicity vs. age for the GES merger (8 - 10 Gyr) and for the first pericentric passage of Sagittarius (5 - 6.5 Gyr). However, it is worth mentioning that taking into account uncertainties is a very important aspect of the statistical study. And the fluctuations we detected for GES and Sagittarius are not significant taking into account the uncertainty.

Acknowledgements

AP acknowledges Roman Tkachenko for useful consultations. BR acknowledges support by the Deutsche Forschungsgemeinschaft under the grant MI 2009/2-1.

Chapter 5

Conclusions and outlook

In this work, I have studied the assembly history of the Milky Way with insights from metal-poor stars and solar twins. To be able to reconstruct the formation and evolution of the Milky Way we need to have three main parameters: age, kinematics and chemistry. All of these data together can shed light on the Milky Way's history.

Starting with metal-poor stars, we analyzed a dataset of 28 stars. For which we derived age by automatic isochrone CMD fitting using Gaia DR3 photometry and the most updated parameters for distance (from Gaia parallax without corrections Sec. 2.5.5) and reddening. The average age from Padova isochrones is 13.9 ± 0.5 Gyr, from BaSTI - 13.7 ± 0.4 Gyr and for stars with both determinations it is of 14.1 ± 0.3 Gyr (internal errors only). Our estimate for the additional systematic error is around 0.5 Gyr. We checked our results against the three most metal-poor GC: NGC 6397, M 30, M 92. Our set of very metal-poor stars on average is older than the most metal-poor GC by about 1 Gyr.

Age determination can depend also on the detailed chemical composition of the stars. The enhancement of α-elements, C, N, O, and Ne can significantly affects the opacity of metal-poor stars and changes the continuum emission. The strongest effect is in the Johnson B filter (Fig.2.8). The effect is marginally present also in Gaia filters but, due to their width, it is much less prominent. The difference in age for different filter combimations G vs. G_{BP}-G, G vs. G-G_{RP}, G vs. G_{BP}-G_{RP} is around 0.2 Gyr. We suggest that, in order to improve the age determination, specific isochrones should be computed for the chemical composition of each star.

Additionally, we studied the age metallicity relation in its very metal-poor tail. The trend is almost horizontal, but our stars are on average older than the mean locus found by other authors (Dotter et al. (2011), Cohen et al. (2021)) by about 0.8 Gyr. The interesting fact is that we found a group of very metal-poor stars with significantly young ages of 8 – 10 Gyr. The age of these stars can be a signature of two different populations (one of which could be accreted) or two epochs of star formation.

Moving forward, we also studied the origin of these metal-poor stars by using age and kinematics that we derived in this work and chemistry from Barklem et al. (2005). Kinematics and chemistry are routinely used to assign stars to different components of the Milky Way galaxy, or to the various accreted systems that have been identified over the years in the Galactic halo. And the timeline was checked with the age.

During the analysis, we identified a group of stars with clear signatures of the Halo population. However, we speculate that the oldest 8 of them could have formed in the

primordial Bulge because of their orbital parameters (large eccentricity and low Z_{max} mostly) and large α-abundance. Also, we have identified another group of stars that we tentatively associate with the metal-poor tail of Gaia-Enceladus/Sausage (GE) (*orange*), and Thamnos 1, 2 (*dark blue, blue*) according to their similarity in kinematics, chemistry and age.

The identification of a group, although small, of stars probably belonging to the infant Bulge is rather intriguing. In fact, it supports a scenario in which the first component of the Milky Way to form was the Bulge via a fast collapse *a là* ELS (Eggen et al. (1962)). The other components have then assembled with a major contribution from systems that engulfed into the Milky Way later on, in agreement with the widely accepted merging scheme (Searle &Zinn (1978)).

By changing the target we are moving to solar twins. We performed a spectroscopic analysis of high-resolution spectra from HARPS-N for 114 solar twins. Expanding our dataset with 371 stars spectroscopically analyzed in Casali et al. (2020) we derived ages with the isochrone fitting technique in the effective temperature vs logarithm of surface gravity space with a metallicity correction for the atomic diffusion at the solar age (485 stars in total).

With obtained high-precision chemical abundances and ages we are able to study the age-metallicity relation (AMR) for solar twins around the Sun ([Fe/H]: -0.3 - 0.3 dex) in high resolution. Our main goal was to test the AMR separation into two groups for solar twins in the thin disk in the solar neighborhood. In the analysis, we took into account all possible sources of errors and did not detect a separation (Fig. 4.6). This result is in agreement with Miglio et al. (2021), Xiang &Rix (2022), Lu et al. (2022b). However, in the literature, some studies reached the opposite result (Nissen et al. 2020; Jofré 2021; Ratcliffe et al. 2023). For Nissen et al. (2020) the separation was caused by the statistical bias. For the other two works, there are two possible reasons. First of all, they employed ages obtained from the use of C and N abundances. This indicates that age determination is one of the crucial aspects of studying these chemical trends. Another extremely important parameter that always should be tested while studying data that has cutoffs is the selection bias. Cutoffs in distance, magnitude, metallicity, etc produce features that lead to misinterpretation of the data. And this topic should be widely explored.

To recover the formation and evolution history from solar twins we, also, studied the dependence of chemical abundance with guiding and birth radii and age (Fig. 4.8). We see that mixed star populations for the guiding radius transform in well-separated trends for the birth radius. It means, that radial migration (more general the inside-out formation) that lies in the basis of the birth radii determination explains well the star's chemical distribution around the Sun. However, these trends are still not perfectly parallel. We can detect knees for some age trends of some elements and overlap for some age trends. It leads us to the conclusion that radial migration alone does not explain all the features in the Milky Way formation history.

Several authors already showed that GES merger and Sagittarius pericentric passages as well as other passages and accretions of dwarf galaxies affected the Milky Way evolution. In Fig. 4.9 we also detect fluctuations in the standard deviation of metallicity vs. age for the GES merger (8 - 10 Gyr) and for the first pericentric passage of Sagittarius (5 - 6.5 Gyr). However, it is worth mentioning that the fluctuations we detected for GES and Sagittarius are not significant taking into account the uncertainty that is very important

in the statistical study.

To sum up, we have studied the Milky Way assembly history by using two scientific targets: very metal-poor stars and solar twins. From their age, chemistry and kinematics we were able to reconstruct the Milky Way formation and evolution starting from the very beginning - infant bulge. It was first to form via a fast collapse *a là* ELS (Eggen et al. (1962)). Then the disk and halo were formed with the major contribution from known accretion events such as Gaia-Enceladus/Sausage, Thumnos etc. After that, the thin disk was smoothly formed inside-out where the radial migration took place also with the help of accretion events and passages of dwarf galaxies.

Acknowledgements

Finally, I would like to thank all my collaborators, especially Giovanni Carraro, Sandro Villanova, Lorenzo Spina and Sergio Ortolani for their huge impact on my research and for the knowledge and experience I gained from them. Also, I would like to acknowledge the Fondazione Cassa di Risparmio di Padova e Rovigo (Cariparo) for the opportunity to go abroad for the internships, schools and conferences, and the Ulisse program of Padova University which allowed me to spend a period at the Concepcion University, where part of this work has been done. Last but not least I would like to thank everyone who supported me in this journey: my family, friends and husband Artem. In the end, I would also like to thank the University of Padova for this beautiful experience full of pasta, pizza, beautiful architecture, culture and astronomy of course. I appreciate all of this and I will remember it forever.

List of Figures

List of Tables

Bibliography

Abadi, M. G., Navarro, J. F., Steinmetz, M., & Eke, V. R. 2003a, ApJ, 591, 499

Abadi, M. G., Navarro, J. F., Steinmetz, M., & Eke, V. R. 2003b, ApJ, 597, 21

Ade, P. A. R., Aghanim, N., Armitage-Caplan, C., et al. 2014, Astronomy & Astrophysics, 571, A16

Agertz, O., Renaud, F., Feltzing, S., et al. 2021, MNRAS, 503, 5826

Ahumada, R., Allende Prieto, C., Almeida, A., et al. 2020, ApJS, 249, 3

Amarante, J. A., Debattista, V. P., Silva, L. B. E., Laporte, C. F., & Deg, N. 2022, The Astrophysical Journal, 937, 12

Amelin, Y., Kaltenbach, A., Iizuka, T., et al. 2010, Earth and Planetary Science Letters, 300, 343

Anders, F., Gispert, P., Ratcliffe, B., et al. 2023, A&A, 678, A158

Anderson, L. D., Sormani, M. C., Ginsburg, A., et al. 2020, ApJ, 901, 51

Antoja, T., Ramos, P., López-Guitart, F., et al. 2022, A&A, 668, A61

Arellano-Córdova, K. Z., Esteban, C., García-Rojas, J., & Méndez-Delgado, J. E. 2021, MNRAS, 502, 225

Athanassoula, E. 2005, Celestial Mechanics and Dynamical Astronomy, 91, 9

Ayres, T. R., Plymate, C., & Keller, C. U. 2006, ApJS, 165, 618

Baba, J. & Kawata, D. 2020, MNRAS, 492, 4500

Babusiaux, C., Gómez, A., Hill, V., et al. 2010, Astronomy & Astrophysics, 519, A77

Babusiaux, C., van Leeuwen, F., Barstow, M., et al. 2018, Astronomy & Astrophysics, 616, A10

Bailer-Jones, C. A. L., Rybizki, J., Fouesneau, M., Demleitner, M., & Andrae, R. 2021, AJ, 161, 147

Ballero, S. K., Matteucci, F., Origlia, L., & Rich, R. M. 2007, A&A, 467, 123

Barklem, P. S., Christlieb, N., Beers, T. C., et al. 2005, A&A, 439, 129

Baugh, C. M., Cole, S., & Frenk, C. S. 1996, MNRAS, 283, 1361

Bedell, M., Bean, J. L., Meléndez, J., et al. 2018, ApJ, 865, 68

Bedell, M., Meléndez, J., Bean, J. L., et al. 2014, ApJ, 795, 23

Belokurov, V. 2013, New A Rev., 57, 100

Belokurov, V., Erkal, D., Evans, N., Koposov, S., & Deason, A. 2018, Monthly Notices of the Royal Astronomical Society, 478, 611

Belokurov, V., Erkal, D., Evans, N. W., Koposov, S. E., & Deason, A. J. 2018, MNRAS, 478, 611

Belokurov, V. & Kravtsov, A. 2022, Monthly Notices of the Royal Astronomical Society, 514, 689

Belokurov, V., Sanders, J. L., Fattahi, A., et al. 2020, Monthly Notices of the Royal Astronomical Society, 494, 3880

Bennett, C. L., Larson, D., Weiland, J. L., et al. 2013, The Astrophysical Journal Supplement Series, 208, 20

Bensby, T., Adén, D., Meléndez, J., et al. 2011, A&A, 533, A134

Bensby, T., Feltzing, S., Lundström, I., & Ilyin, I. 2005, A&A, 433, 185

Bensby, T., Feltzing, S., & Oey, M. S. 2014, A&A, 562, A71

Bensby, T., Zenn, A., Oey, M., & Feltzing, S. 2007, The Astrophysical Journal, 663, L13

Bignone, L. A., Helmi, A., & Tissera, P. B. 2019, ApJ, 883, L5

Binney, J., Gerhard, O. E., Stark, A. A., Bally, J., & Uchida, K. I. 1991, Monthly Notices of the Royal Astronomical Society, 252, 210

Bird, J. C., Kazantzidis, S., & Weinberg, D. H. 2012, MNRAS, 420, 913

Bird, J. C., Kazantzidis, S., Weinberg, D. H., et al. 2013, The Astrophysical Journal, 773, 43

Bissantz, N. & Gerhard, O. 2002, MNRAS, 330, 591

Bland-Hawthorn, J. & Gerhard, O. 2016, Annual Review of Astronomy and Astrophysics, 54, 529

Bland-Hawthorn, J. & Gerhard, O. 2016, ARA&A, 54, 529

Bland-Hawthorn, J. & Tepper-García, T. 2021, MNRAS, 504, 3168

Bonaca, A., Conroy, C., Cargile, P. A., et al. 2020, ApJ, 897, L18

Bond, H. E., Nelan, E. P., VandenBerg, D. A., Schaefer, G. H., & Harmer, D. 2013, ApJ, 765, L12

Bonfanti, A., Ortolani, S., Piotto, G., & Nascimbeni, V. 2015, A&A, 575, A18

Bovy, J. 2015, The Astrophysical Journal Supplement Series, 216, 29

Bovy, J., Leung, H. W., Hunt, J. A. S., et al. 2019, MNRAS, 490, 4740

Bovy, J., Rix, H.-W., Liu, C., et al. 2012, ApJ, 753, 148

Bovy, J., Rix, H.-W., Schlafly, E. F., et al. 2016, ApJ, 823, 30

Bromm, V. & Larson, R. B. 2004, ARA&A, 42, 79

Brook, C. B., Stinson, G., Gibson, B. K., et al. 2012, Monthly Notices of the Royal Astronomical Society, 426, 690

Buck, T. 2020, MNRAS, 491, 5435

Buck, T., Obreja, A., Ratcliffe, B., et al. 2023, MNRAS, 523, 1565

Buder, S., Asplund, M., Duong, L., et al. 2018, Monthly Notices of the Royal Astronomical Society, 478, 4513

Buder, S., Sharma, S., Kos, J., et al. 2021, MNRAS, 506, 150

Bullock, J. S. & Boylan-Kolchin, M. 2017, Annual Review of Astronomy and Astrophysics, 55, 343

Bullock, J. S. & Johnston, K. V. 2005, ApJ, 635, 931

Bullock, J. S. & Johnston, K. V. 2005, The Astrophysical Journal, 635, 931

Carraro, G., Girardi, L., & Chiosi, C. 1999, MNRAS, 309, 430

Carter, C., Conroy, C., Zaritsky, D., et al. 2021, ApJ, 908, 208

Casali, G., Spina, L., Magrini, L., et al. 2020, A&A, 639, A127

Castelli, F. & Kurucz, R. L. 2004, A&A, 419, 725

Cayrel, R., Depagne, E., Spite, M., et al. 2004, A&A, 416, 1117

Ceccarelli, E., Massari, D., Mucciarelli, A., et al. 2024, arXiv preprint arXiv:2401.04184

Cescutti, G. & Matteucci, F. 2011, A&A, 525, A126

Chemel, A. A., Glushkova, E. V., Dambis, A. K., et al. 2018, Astrophysical Bulletin, 73, 162

Cheng, J. Y., Rockosi, C. M., Morrison, H. L., et al. 2012, in Astronomical Society of the Pacific Conference Series, Vol. 458, Galactic Archaeology: Near-Field Cosmology and the Formation of the Milky Way, ed. W. Aoki, M. Ishigaki, T. Suda, T. Tsujimoto, & N. Arimoto, 105

Chiappini, C., Matteucci, F., & Gratton, R. 1997, ApJ, 477, 765

Chiba, R., Friske, J. K., & Schönrich, R. 2021, Monthly Notices of the Royal Astronomical Society, 500, 4710

Chiba, R. & Schönrich, R. 2021, MNRAS, 505, 2412

Chiba, R. & Schönrich, R. 2022, MNRAS, 513, 768

Christlieb, N., Beers, T. C., Barklem, P. S., et al. 2004, A&A, 428, 1027

Ciambur, B. C., Fragkoudi, F., Khoperskov, S., Di Matteo, P., & Combes, F. 2021, MNRAS, 503, 2203

Clarke, J. P., Wegg, C., Gerhard, O., et al. 2019, MNRAS, 489, 3519

Cohen, R. E., Bellini, A., Casagrande, L., et al. 2021, AJ, 162, 228

Cole, A. A. & Weinberg, M. D. 2002, ApJ, 574, L43

Combes, F., Debbasch, F., Friedli, D., & Pfenniger, D. 1990, A&A, 233, 82

Connelly, J. N., Amelin, Y., Krot, A. N., & Bizzarro, M. 2008, ApJ, 675, L121

Cooper, A. P., Cole, S., Frenk, C., et al. 2010, Monthly Notices of the Royal Astronomical Society, 406, 744

Correnti, M., Gennaro, M., Kalirai, J. S., Cohen, R. E., & Brown, T. M. 2018, ApJ, 864, 147

Courteau, S., de Jong, R. S., & Broeils, A. H. 1996, ApJ, 457, L73

Cui, X.-Q., Zhao, Y.-H., Chu, Y.-Q., et al. 2012, Research in Astronomy and Astrophysics, 12, 1197

De Boer, T., Belokurov, V., Beers, T., & Lee, Y. 2014, Monthly Notices of the Royal Astronomical Society, 443, 658

De Lucia, G. & Helmi, A. 2008, Monthly Notices of the Royal Astronomical Society, 391, 14

De Propris, R., Colless, M., Driver, S. P., Pracy, M. B., & Couch, W. J. 2005, MNRAS, 357, 590

De Silva, G. M., Freeman, K. C., Bland-Hawthorn, J., et al. 2015, Monthly Notices of the Royal Astronomical Society, 449, 2604

Deason, A. J. & Belokurov, V. 2024, arXiv preprint arXiv:2402.12443

Deason, A. J., Mao, Y.-Y., & Wechsler, R. H. 2016, The Astrophysical Journal, 821, 5

Debattista, V. P. & Sellwood, J. 2000, The Astrophysical Journal, 543, 704

Deharveng, L., Peña, M., Caplan, J., & Costero, R. 2000, MNRAS, 311, 329

Dodd, E., Callingham, T. M., Helmi, A., et al. 2023, A&A, 670, L2

Dotter, A., Conroy, C., Cargile, P., & Asplund, M. 2017, ApJ, 840, 99

Dotter, A., Sarajedini, A., & Anderson, J. 2011, ApJ, 738, 74

Drimmel, R. & Poggio, E. 2018, Research Notes of the American Astronomical Society, 2, 210

Eggen, O. J., Lynden-Bell, D., & Sandage, A. R. 1962, ApJ, 136, 748

El-Badry, K., Rix, H.-W., & Heintz, T. M. 2021, MNRAS[arXiv:2101.05282]

Epstein, C. R., Johnson, J. A., Dong, S., et al. 2010, ApJ, 709, 447

Esteban, C., Fang, X., García-Rojas, J., & Toribio San Cipriano, L. 2017, MNRAS, 471, 987

Esteban, C., Méndez-Delgado, J. E., García-Rojas, J., & Arellano-Córdova, K. Z. 2022, ApJ, 931, 92

Fakhouri, O., Ma, C.-P., & Boylan-Kolchin, M. 2010, Monthly Notices of the Royal Astronomical Society, 406, 2267

Fattahi, A., Deason, A. J., Frenk, C. S., et al. 2020, Monthly Notices of the Royal Astronomical Society, 497, 4459

Feltzing, S., Fohlman, M., & Bensby, T. 2007, A&A, 467, 665

Feuillet, D. K., Bovy, J., Holtzman, J., et al. 2018, MNRAS, 477, 2326

Feuillet, D. K., Feltzing, S., Sahlholdt, C. L., & Casagrande, L. 2020, Monthly Notices of the Royal Astronomical Society, 497, 109

François, P., Depagne, E., Hill, V., et al. 2007, A&A, 476, 935

Frankel, N., Rix, H.-W., Ting, Y.-S., Ness, M., & Hogg, D. W. 2018, ApJ, 865, 96

Frebel, A. & Norris, J. E. 2015, ARA&A, 53, 631

Freeman, K. & Bland-Hawthorn, J. 2002, ARA&A, 40, 487

Freeman, K., Ness, M., Wylie-de-Boer, E., et al. 2013, MNRAS, 428, 3660

Fuhrmann, K. 1998, A&A, 338, 161

Fuhrmann, K. 2004, Astronomische Nachrichten, 325, 3

Fuhrmann, K. 2008, MNRAS, 384, 173

Fuhrmann, K. 2011, Monthly Notices of the Royal Astronomical Society, 414, 2893

Fulbright, J. P. 2000, AJ, 120, 1841

Gadotti, D. A. & dos Anjos, S. 2001, AJ, 122, 1298

Gaia Collaboration. 2021, A&A, 649, A1

Gaia-Collaboration, Brown, A. G. A., Vallenari, A., et al. 2018, Astronomy and Astrophysics, 616, A1

Gaia-Collaboration, Brown, A. G. A., Vallenari, A., et al. 2020, arXiv:2012.01533 [astro-ph], tex.ids= brown21GaiaEarlyData arXiv: 2012.01533 publisher: EDP Sciences

Gaia Collaboration, Gaia Collaboration, De Ridder, J., et al. 2022a, arXiv e-prints, arXiv:2206.06075

Gaia Collaboration, Vallenari, A., Brown, A. G. A., et al. 2022b, arXiv e-prints, arXiv:2208.00211

Gallart, C., Bernard, E. J., Brook, C. B., et al. 2019, Nature Astronomy, 3, 932

Gao, L., White, S. D., Jenkins, A., Stoehr, F., & Springel, V. 2004, Monthly Notices of the Royal Astronomical Society, 355, 819

Ghosh, S., Fragkoudi, F., Di Matteo, P., & Saha, K. 2023, A&A, 674, A128

Gilmore, G. 1996, in Astronomical Society of the Pacific Conference Series, Vol. 92, Formation of the Galactic Halo...Inside and Out, ed. H. L. Morrison & A. Sarajedini, 161

Gilmore, G., Randich, S., Asplund, M., et al. 2012, The Messenger, 147, 25

Gilmore, G. & Reid, N. 1983, MNRAS, 202, 1025

Gondoin, P. 2023, A&A, 678, A39

Gonzalez, O. A., Zoccali, M., Vasquez, S., et al. 2015, A&A, 584, A46

Grady, J., Belokurov, V., & Evans, N. W. 2020, MNRAS, 492, 3128

Grand, R. J. J., Bustamante, S., Gómez, F. A., et al. 2018, MNRAS, 474, 3629

GRAVITY Collaboration, Abuter, R., Amorim, A., et al. 2018, A&A, 615, L15

Green, G. M., Schlafly, E. F., Finkbeiner, D., et al. 2018, MNRAS, 478, 651

Grenon, M. 1972, in IAU Colloq. 17: Age des Etoiles, ed. G. Cayrel de Strobel & A. M. Delplace, 55

Grenon, M. 1985, in Cool Stars with Excesses of Heavy Elements, ed. M. Jaschek & P. C. Keenan, Vol. 114, 147

Grenon, M. 1989, , 156, 29

Grieco, V., Matteucci, F., Pipino, A., & Cescutti, G. 2012, A&A, 548, A60

Grieco, V., Matteucci, F., Ryde, N., Schultheis, M., & Uttenthaler, S. 2015, MNRAS, 450, 2094

Grillmair, C. J. 2017, ApJ, 847, 119

Hawkins, K., Jofre, P., Masseron, T., & Gilmore, G. 2015, Monthly Notices of the Royal Astronomical Society, 453, 758

Hayden, M. R., Bovy, J., Holtzman, J. A., et al. 2015, The Astrophysical Journal, 808, 132

Haywood, M., Di Matteo, P., Lehnert, M., et al. 2018, The Astrophysical Journal, 863, 113

Haywood, M., Di Matteo, P., Lehnert, M. D., Katz, D., & Gómez, A. 2013, A&A, 560, A109

Haywood, M., Lehnert, M. D., Di Matteo, P., et al. 2016, A&A, 589, A66

Haywood, M., Snaith, O., Lehnert, M. D., Di Matteo, P., & Khoperskov, S. 2019, A&A, 625, A105

Helmi, A. 2002, , 281, 351

Helmi, A. 2020, Annual Review of Astronomy and Astrophysics, 58, 205

Helmi, A., Babusiaux, C., Koppelman, H. H., et al. 2018, Nature, 563, 85

Helmi, A. & Tim de Zeeuw, P. 2000, Monthly Notices of the Royal Astronomical Society, 319, 657

Hendel, D. & Johnston, K. V. 2015, Monthly Notices of the Royal Astronomical Society, 454, 2472

Hendricks, B., Koch, A., Lanfranchi, G. A., et al. 2014, The Astrophysical Journal, 785, 102

Hernquist, L. & Weinberg, M. D. 1992, Astrophysical Journal, Part 1 (ISSN 0004-637X), vol. 400, no. 1, p. 80-95., 400, 80

Hidalgo, S. L., Pietrinferni, A., Cassisi, S., et al. 2018, ApJ, 856, 125

Hill, V., Lecureur, A., Gómez, A., et al. 2011, A&A, 534, A80

Horta, D., Cunningham, E. C., Sanderson, R., et al. 2024, Monthly Notices of the Royal Astronomical Society, 527, 9810

Horta, D., Schiavon, R. P., Mackereth, J. T., et al. 2021, Monthly Notices of the Royal Astronomical Society, 500, 1385

Horta, D., Schiavon, R. P., Mackereth, J. T., et al. 2023, Monthly Notices of the Royal Astronomical Society, 520, 5671

Howes, L. M., Asplund, M., Keller, S. C., et al. 2016, MNRAS, 460, 884

Ibata, R. A., Gilmore, G., & Irwin, M. J. 1994, Nature, 370, 194

Ibata, R. A., Lewis, G. F., Irwin, M. J., & Cambrésy, L. 2002, MNRAS, 332, 921

Jenkins, A., Frenk, C., White, S. D., et al. 2001, Monthly Notices of the Royal Astronomical Society, 321, 372

Jofré, P. 2021, ApJ, 920, 23

Johnson, C. I., Rich, R. M., Kobayashi, C., & Fulbright, J. P. 2012, ApJ, 749, 175

Johnson, C. I., Rich, R. M., Kobayashi, C., Kunder, A., & Koch, A. 2014, AJ, 148, 67

Johnson, C. I., Rich, R. M., Simion, I. T., et al. 2022, MNRAS, 515, 1469

Johnson, C. I., Rich, R. M., Young, M. D., et al. 2020, MNRAS, 499, 2357

Jönsson, H., Holtzman, J. A., Prieto, C. A., et al. 2020, The Astronomical Journal, 160, 120

Kains, N., Bramich, D. M., Arellano Ferro, A., et al. 2013, A&A, 555, A36

Khoperskov, S., Haywood, M., Snaith, O., et al. 2021, MNRAS, 501, 5176

Kobayashi, C., Karakas, A. I., & Lugaro, M. 2020, The Astrophysical Journal, 900, 179

Kobayashi, C., Umeda, H., Nomoto, K., Tominaga, N., & Ohkubo, T. 2006, The Astrophysical Journal, 653, 1145

Koppelman, H. H., Bos, R. O. Y., & Helmi, A. 2020, A&A, 642, L18

Koppelman, H. H., Helmi, A., Massari, D., Price-Whelan, A. M., & Starkenburg, T. K. 2019, A&A, 631, L9

Kordopatis, G., Gilmore, G., Wyse, R. F., et al. 2013, Monthly Notices of the Royal Astronomical Society, 436, 3231

Kraljic, K., Bournaud, F., & Martig, M. 2012, The Astrophysical Journal, 757, 60

Kunder, A., Koch, A., Rich, R. M., et al. 2012, AJ, 143, 57

Lallement, R., Capitanio, L., Ruiz-Dern, L., et al. 2018, A&A, 616, A132

Lane, J. M., Bovy, J., & Mackereth, J. T. 2023, Monthly Notices of the Royal Astronomical Society, 526, 1209

Laporte, C. F. P., Minchev, I., Johnston, K. V., & Gómez, F. A. 2019, MNRAS, 485, 3134

Lian, J., Thomas, D., Maraston, C., et al. 2020, Monthly Notices of the Royal Astronomical Society, 497, 2371

Lian, J., Thomas, D., Maraston, C., et al. 2020a, MNRAS, 494, 2561

Lian, J., Zasowski, G., Hasselquist, S., et al. 2020b, MNRAS, 497, 3557

Lian, J., Zasowski, G., Hasselquist, S., et al. 2021, MNRAS, 500, 282

Limberg, G., Santucci, R. M., Rossi, S., et al. 2021, ApJ, 913, 11

Lindegren, L., Bastian, U., Biermann, M., et al. 2021, A&A, 649, A4

Lindegren, L., Hernández, J., Bombrun, A., et al. 2018, A&A, 616, A2

Lindegren, L., Klioner, S., Hernández, J., et al. 2021a, Astronomy & Astrophysics, 649, A2

Lindegren, L., Klioner, S., Hernández, J., et al. 2021b, Astronomy & Astrophysics, 649, A2

Liu, F., Asplund, M., Yong, D., et al. 2016, MNRAS, 463, 696

López-Corredoira, M., Cabrera-Lavers, A., & Gerhard, O. E. 2005, A&A, 439, 107

Lövdal, S. S., Ruiz-Lara, T., Koppelman, H. H., et al. 2022, Astronomy & Astrophysics, 665, A57

Lu, Y., Buck, T., Minchev, I., & Ness, M. K. 2022a, MNRAS, 515, L34

Lu, Y., Minchev, I., Buck, T., et al. 2022b, arXiv e-prints, arXiv:2212.04515

Lucey, M., Hawkins, K., Ness, M., et al. 2022, MNRAS, 509, 122

Mackereth, J. T. & Bovy, J. 2020, Monthly Notices of the Royal Astronomical Society, 492, 3631

Madau, P. & Dickinson, M. 2014, ARA&A, 52, 415

Majewski, S. R., Schiavon, R. P., Frinchaboy, P. M., et al. 2017, The Astronomical Journal, 154, 94

Maoz, D. & Mannucci, F. 2012, Publications of the Astronomical Society of Australia, 29, 447

Martell, S. L., Smolinski, J. P., Beers, T. C., & Grebel, E. K. 2011, A&A, 534, A136

Martinez-Valpuesta, I., Shlosman, I., & Heller, C. 2006, ApJ, 637, 214

Martocchia, S., Savino, A., Grebel, E. K., et al. 2023, in SF2A-2023: Proceedings of the Annual meeting of the French Society of Astronomy and Astrophysics, ed. M. N'Diaye, A. Siebert, N. Lagarde, O. Venot, K. Bailliée, M. Béthermin, E. Lagadec, J. Malzac, & J. Richard, 99–103

Mason, A. C., Crain, R. A., Schiavon, R. P., et al. 2024, Monthly Notices of the Royal Astronomical Society, 533, 184

Matsuno, T., Aoki, W., & Suda, T. 2019, The Astrophysical Journal Letters, 874, L35

Matsuno, T., Koppelman, H. H., Helmi, A., et al. 2022, Astronomy & Astrophysics, 661, A103

Matteucci, F. & Brocato, E. 1990, Astrophysical Journal, Part 1 (ISSN 0004-637X), vol. 365, Dec. 20, 1990, p. 539-543., 365, 539

Matteucci, F., Grisoni, V., Spitoni, E., et al. 2019, Monthly Notices of the Royal Astronomical Society, 487, 5363

McMillan, P. J. 2017, MNRAS, 465, 76

McWilliam, A. & Rich, R. M. 1994, ApJS, 91, 749

McWilliam, A. & Zoccali, M. 2010, ApJ, 724, 1491

Meléndez, J., Asplund, M., Gustafsson, B., & Yong, D. 2009, ApJ, 704, L66

Meléndez, J., Bergemann, M., Cohen, J. G., et al. 2012, A&A, 543, A29

Meléndez, J., Ramírez, I., Karakas, A. I., et al. 2014, ApJ, 791, 14

Miglio, A., Chiappini, C., Mackereth, J. T., et al. 2021, A&A, 645, A85

Minchev, I., Anders, F., Recio-Blanco, A., et al. 2018, MNRAS, 481, 1645

Minchev, I., Chiappini, C., & Martig, M. 2016, Astronomische Nachrichten, 337, 944

Minniti, D., Lucas, P., Emerson, J., et al. 2010, New Astronomy, 15, 433

Monachesi, A., Gómez, F. A., Grand, R. J., et al. 2019, Monthly Notices of the Royal Astronomical Society, 485, 2589

Montalbán, J., Mackereth, J. T., Miglio, A., et al. 2021, Nature Astronomy, 5, 640

Montalto, M., Piotto, G., Marrese, P. M., et al. 2021, A&A, 653, A98

Moore, B., Ghigna, S., Governato, F., et al. 1999, The Astrophysical Journal, 524, L19

Myeong, G., Belokurov, V., Aguado, D. S., et al. 2022, The Astrophysical Journal, 938, 21

Myeong, G., Vasiliev, E., Iorio, G., Evans, N., & Belokurov, V. 2019, Monthly Notices of the Royal Astronomical Society, 488, 1235

Myeong, G. C., Vasiliev, E., Iorio, G., Evans, N. W., & Belokurov, V. 2019, MNRAS, 488, 1235

Naidu, R. P., Conroy, C., Bonaca, A., et al. 2020, The Astrophysical Journal, 901, 48

Naidu, R. P., Conroy, C., Bonaca, A., et al. 2021, The Astrophysical Journal, 923, 92

Nelson, E. J., Van Dokkum, P. G., Schreiber, N. M. F., et al. 2016, The Astrophysical Journal, 828, 27

Ness, M. & Lang, D. 2016, AJ, 152, 14

Ness, M. K., Johnston, K. V., Blancato, K., et al. 2019, ApJ, 883, 177

Nidever, D. L., Bovy, J., Bird, J. C., et al. 2014, The Astrophysical Journal, 796, 38

Nissen, P. E., Christensen-Dalsgaard, J., Mosumgaard, J. R., et al. 2020, A&A, 640, A81

Noguchi, M. 2018, Nature, 559, 585

Nordlander, T. & Lind, K. 2017, A&A, 607, A75

Norris, J. 1987, ApJ, 314, L39

O'Neill, J. K. & Dubinski, J. 2003, Monthly Notices of the Royal Astronomical Society, 346, 251

Ortolani, S., Renzini, A., Gilmozzi, R., et al. 1995, Nature, 377, 701

Pagel, B. E. J. 1997, Nucleosynthesis and Chemical Evolution of Galaxies

Plotnikova, A., Carraro, G., Villanova, S., & Ortolani, S. 2022, ApJ, 940, 159

Plotnikova, A., Carraro, G., Villanova, S., & Ortolani, S. 2023, ApJ, 949, 31

Pop, A.-R., Pillepich, A., Amorisco, N. C., & Hernquist, L. 2018, Monthly Notices of the Royal Astronomical Society, 480, 1715

Portail, M., Gerhard, O., Wegg, C., & Ness, M. 2017, MNRAS, 465, 1621

Portail, M., Wegg, C., Gerhard, O., & Martinez-Valpuesta, I. 2015, MNRAS, 448, 713

Prochaska, J. X., Naumov, S. O., Carney, B. W., McWilliam, A., & Wolfe, A. M. 2000, The Astronomical Journal, 120, 2513

Prusti, T., De Bruijne, J., Brown, A. G., et al. 2016, Astronomy & astrophysics, 595, A1

Purcell, C. W., Bullock, J. S., & Zentner, A. R. 2007, The Astrophysical Journal, 666, 20

Queiroz, A. B. A., Anders, F., Chiappini, C., et al. 2023, A&A, 673, A155

Queiroz, A. B. A., Anders, F., Chiappini, C., et al. 2019, arXiv e-prints, arXiv:1912.09778

Queiroz, A. B. A., Anders, F., Chiappini, C., et al. 2020, A&A, 638, A76

Queiroz, A. B. A., Chiappini, C., Perez-Villegas, A., et al. 2021, A&A, 656, A156

Quillen, A. C., Minchev, I., Bland-Hawthorn, J., & Haywood, M. 2009, MNRAS, 397, 1599

Raha, N., Sellwood, J., James, R., & Kahn, F. 1991, nature, 352, 411

Ramírez, I., Meléndez, J., & Asplund, M. 2009, A&A, 508, L17

Ramírez, I., Meléndez, J., Bean, J., et al. 2014, A&A, 572, A48

Ratcliffe, B., Khoperskov, S., Minchev, I., et al. 2024, arXiv e-prints, arXiv:2401.09260

Ratcliffe, B., Minchev, I., Anders, F., et al. 2023, MNRAS, 525, 2208

Ratcliffe, B. L., Ness, M. K., Buck, T., et al. 2022, ApJ, 924, 60

Reddy, B. E., Lambert, D. L., & Allende Prieto, C. 2006, MNRAS, 367, 1329

Reddy, B. E., Tomkin, J., Lambert, D. L., & Allende Prieto, C. 2003, MNRAS, 340, 304

Reid, M. J. & Brunthaler, A. 2004, ApJ, 616, 872

Reina-Campos, M., Hughes, M. E., Kruijssen, J. M. D., et al. 2020, MNRAS, 493, 3422

Rich, R. M., Howard, C., Reitzel, D. B., Zhao, H., & de Propris, R. 2008, in IAU Symposium, Vol. 245, Formation and Evolution of Galaxy Bulges, ed. M. Bureau, E. Athanassoula, & B. Barbuy, 333–338

Ritter, J. S., Safranek-Shrader, C., Gnat, O., Milosavljević, M., & Bromm, V. 2012, ApJ, 761, 56

Robin, A. C., Bienaymé, O., Fernández-Trincado, J. G., & Reylé, C. 2017, A&A, 605, A1

Roederer, I. U., Preston, G. W., Thompson, I. B., et al. 2014, AJ, 147, 136

Rojas-Arriagada, A., Recio-Blanco, A., de Laverny, P., et al. 2017, A&A, 601, A140

Rojas-Arriagada, A., Zasowski, G., Schultheis, M., et al. 2020, Monthly Notices of the Royal Astronomical Society, 499, 1037

Rojas-Arriagada, A., Zoccali, M., Schultheis, M., et al. 2019, A&A, 626, A16

Roškar, R., Debattista, V. P., Stinson, G. S., et al. 2008, ApJ, 675, L65

Ruiz-Lara, T., Gallart, C., Bernard, E. J., & Cassisi, S. 2020, Nature Astronomy, 4, 965

Ruiz-Lara, T., Helmi, A., Gallart, C., Surot, F., & Cassisi, S. 2022, Astronomy & Astrophysics, 668, L10

Ruiz-Lara, T., Matsuno, T., Lövdal, S. S., et al. 2022, A&A, 665, A58

Safranek-Shrader, C., Milosavljevic, M., & Bromm, V. 2014, MNRAS, 440, L76

Sahlholdt, C. L., Feltzing, S., & Feuillet, D. K. 2022, MNRAS, 510, 4669

Salaris, M., Chieffi, A., & Straniero, O. 1993, ApJ, 414, 580

Sanders, J. L., Smith, L., Evans, N. W., & Lucas, P. 2019, MNRAS, 487, 5188

Schlafly, E. F. & Finkbeiner, D. P. 2011, ApJ, 737, 103

Schlaufman, K. C. & Casey, A. R. 2014, ApJ, 797, 13

Schlegel, D. J., Finkbeiner, D. P., & Davis, M. 1998, ApJ, 500, 525

Schönrich, R. & Binney, J. 2009a, Monthly Notices of the Royal Astronomical Society, 396, 203

Schönrich, R. & Binney, J. 2009b, Monthly Notices of the Royal Astronomical Society, 399, 1145

Searle, L. & Zinn, R. 1978, ApJ, 225, 357

Sellwood, J. A. & Binney, J. J. 2002, MNRAS, 336, 785

Sestito, F., Venn, K. A., Arentsen, A., et al. 2022, arXiv e-prints, arXiv:2208.13791

Sharma, S., Hayden, M. R., & Bland-Hawthorn, J. 2021, MNRAS, 507, 5882

Shen, J., Rich, R. M., Kormendy, J., et al. 2010, ApJ, 720, L72

Shen, L., Papovich, C., Matharu, J., et al. 2024, ApJ, 963, L49

Sheth, K., Elmegreen, D. M., Elmegreen, B. G., et al. 2008, The Astrophysical Journal, 675, 1141

Simmerer, J. 2004, in American Astronomical Society Meeting Abstracts, Vol. 205, American Astronomical Society Meeting Abstracts, 77.05

Snaith, O., Haywood, M., Di Matteo, P., et al. 2015a, A&A, 578, A87

Snaith, O., Haywood, M., Di Matteo, P., et al. 2015b, A&A, 578, A87

Sneden, C. 1973, ApJ, 184, 839

Sormani, M. C., Binney, J., & Magorrian, J. 2015, MNRAS, 454, 1818

Soto, M., Rich, R. M., & Kuijken, K. 2007, ApJ, 665, L31

Soubiran, C., Bienaymé, O., & Siebert, A. 2003, A&A, 398, 141

Spina, L., Meléndez, J., Karakas, A. I., et al. 2018, MNRAS, 474, 2580

Spina, L., Meléndez, J., Karakas, A. I., et al. 2016, A&A, 593, A125

Spitoni, E., Silva Aguirre, V., Matteucci, F., Calura, F., & Grisoni, V. 2019, A&A, 623, A60

Steinmetz, M., Guiglion, G., McMillan, P. J., et al. 2020, AJ, 160, 83

Steinmetz, M., Matijevič, G., Enke, H., et al. 2020, The Astronomical Journal, 160, 82

Tacchella, S., Carollo, C. M., Renzini, A., et al. 2015, Science, 348, 314

Tadaki, K.-i., Genzel, R., Kodama, T., et al. 2017, ApJ, 834, 135

Ted Mackereth, J., Bovy, J., Schiavon, R. P., et al. 2017, Monthly Notices of the Royal Astronomical Society, 471, 3057

Tinker, J., Kravtsov, A. V., Klypin, A., et al. 2008, The Astrophysical Journal, 688, 709

Tinsley, B. M. 1979, Astrophysical Journal, Part 1, vol. 229, May 1, 1979, p. 1046-1056. Research supported by the Alfred P. Sloan Foundation, 229, 1046

Tkachenko, R., Korchagin, V., Jmailova, A., Carraro, G., & Jmailov, B. 2023, Galaxies, 11, 26

Tsujimoto, T. & Bekki, K. 2012, ApJ, 747, 125

Twarog, B. A. 1980, ApJ, 242, 242

Uttenthaler, S., Schultheis, M., Nataf, D. M., et al. 2012, A&A, 546, A57

VandenBerg, D. A., Bond, H. E., Nelan, E. P., et al. 2014, ApJ, 792, 110

VandenBerg, D. A., Denissenkov, P. A., & Catelan, M. 2016, ApJ, 827, 2

Venn, K. A., Irwin, M., Shetrone, M. D., et al. 2004, The Astronomical Journal, 128, 1177

Vincenzo, F. & Kobayashi, C. 2018, MNRAS, 478, 155

Vincenzo, F., Spitoni, E., Calura, F., et al. 2019, Monthly Notices of the Royal Astronomical Society: Letters, 487, L47

Wang, J., Hammer, F., Yang, Y., et al. 2024, MNRAS, 527, 7144

Wegg, C. & Gerhard, O. 2013, MNRAS, 435, 1874

Weiland, J. L., Arendt, R. G., Berriman, G. B., et al. 1994, ApJ, 425, L81

Xiang, M. & Rix, H.-W. 2022, Nature, 603, 599

Yeh, F.-C., Carraro, G., Korchagin, V. I., Pianta, C., & Ortolani, S. 2020, A&A, 635, A125

Yong, D., Norris, J. E., Bessell, M. S., et al. 2013, ApJ, 762, 26

Yoshii, Y. 1982, , 34, 365

Yuan, Z., Myeong, G., Beers, T. C., et al. 2020, The Astrophysical Journal, 891, 39

Yuan, Z., Myeong, G. C., Beers, T. C., et al. 2020, ApJ, 891, 39

Zhao, G., Zhao, Y.-H., Chu, Y.-Q., Jing, Y.-P., & Deng, L.-C. 2012, Research in Astronomy and Astrophysics, 12, 723

Zhao, H., Rich, R. M., & Spergel, D. N. 1996, MNRAS, 282, 175

Zoccali, M., Gonzalez, O. A., Vasquez, S., et al. 2014, A&A, 562, A66

Zoccali, M., Vasquez, S., Gonzalez, O. A., et al. 2017, A&A, 599, A12